



UNIVERSITÉ CATHOLIQUE DE LOUVAIN

LINMA 2990 - MASTER'S THESIS IN APPLIED MATHEMATICS

Generation of a dictionary of DW-MRI signals from arbitrary brain microstructure configurations

Author:

Gaëtan RENSONNET

Supervisors:

Prof. Benoît MACQ

PhD. Maxime TAQUET

June 2015

Acknowledgements

Merci à mes parents pour leur précieux soutien au cours de ces cinq années.

Merci à mes promoteurs pour leurs conseils et pour m'avoir fait découvrir ce complexe mais fascinant sujet où se mêlent physique, biologie et mathématiques.

Contents

Acknowledgements	i
List of Figures	v
List of Tables	vii
Abbreviations	viii
Physical Constants	ix
Symbols	x
Introduction	1
1 DW-MRI : theoretical background	3
1.1 Basics of Magnetic Resonance Imaging	4
1.1.1 The spin echo experiment	5
1.1.2 Macroscopic description : the Bloch equations	6
1.1.3 Statistical model for the acquisition noise	7
1.2 Diffusion processes	8
1.3 Diffusion-Weighted Imaging	10
1.3.1 The pulsed-gradient spin echo sequence	10
1.3.2 Microscopic description : random walk	11
1.3.3 Macroscopic description : the Bloch-Torrey equations	12
1.3.4 Superposition principle	14
1.4 Microstructure imaging : open challenges	15
1.4.1 Examples of traditional models	16
1.4.2 Challenges of microstructure imaging	18
1.4.3 A dictionary of synthetic signals for microstructure imaging	20
2 Synthetic generation of DW-MRI signals : a hybrid approach	22
2.1 Limitations of traditional data synthesis techniques	23
2.2 Monte Carlo simulations	24
2.2.1 Description	24
2.2.2 Advantages and limitations	25
2.3 The multiple correlation function approach	27
2.3.1 Description	27
2.3.2 Advantages and limitations	28
2.4 A hybrid approach for DW-MRI signal synthesis	29

2.4.1	Validation	29
2.4.1.1	Single array of identical cylinders	30
2.4.1.2	Crossing arrays of identical cylinders	31
2.4.1.3	Array of Gamma-distributed cylinders	32
2.4.2	Precision-efficiency gain	33
3	Creation of a dictionary of DW-MRI signals	36
3.1	Selection of acquisition sequences	37
3.1.1	Traditional acquisition schemes selected for the dictionary	38
3.1.2	Supplementary HARDI shells	39
3.2	Selection of microstructure configurations	41
3.2.1	Single fascicles of identical axons	42
3.2.2	Crossing fascicles of identical axons	46
3.2.3	Single fascicles of Gamma-distributed axons	48
3.2.4	Glial cells	50
4	Exploratory analysis of the dictionary	51
4.1	Challenging the superposition hypothesis for crossing fascicles	52
4.1.1	Procedure	52
4.1.2	Assessment of microstructural similarity	53
4.1.3	Results	54
4.1.4	Discussion	56
4.2	Resistance to noise	56
4.2.1	Procedure	57
4.2.2	Assessment of resistance to noise	58
4.2.3	Results	58
4.2.4	Discussion	59
	Conclusion	62
A	The spin echo experiment	63
B	The SGP and GPD approximations	64
C	The multiple correlation function approach	66
D	Traditional acquisition protocols selected for the dictionary	70
E	Validation of the generated DW-MRI signals	73
E.1	Single fascicles of identical axons	73
E.2	Crossing fascicles of identical axons	75
E.3	Single fascicles of Gamma-distributed axons	77
E.4	Glial cells	79
F	Dictionary parameters	81
G	Rotation of single-fascicle atoms	83

H Exploratory analysis of the dictionary	85
---	-----------

Bibliography	90
---------------------	-----------

List of Figures

1	Microstructure characterization through dictionary matching	2
1.1	Longitudinal magnetization in external magnetic field	5
1.2	$T2$ vs $T2^*$ relaxation	7
1.3	Diffusion from thermal motion	9
1.4	SE-based PGSE sequence	11
1.5	Superposition principle	14
1.6	Brain WM microstructure at different scales	15
2.1	Elastic reflection of random walkers	25
2.2	MC vs hybrid method for a single fascicle of axons	31
2.3	MC vs hybrid method for two crossing fascicles of axons	32
2.4	MC vs hybrid method for a single array of Gamma-distributed cylinders .	33
2.5	Precision-efficiency gain of the hybrid method	35
3.1	Typical length scale of hexagonally-packed cylinders	43
3.2	Convergence of MC simulations through standard deviation analysis . . .	45
3.3	Convergence of MC simulations through mean analysis	45
3.4	Cylinder packing of crossing fascicles	48
3.5	Axons with Gamma-distributed radii	48
4.1	Superposition principle : intermediate setup	55
4.2	1-micron error probability in Gaussian scenario	60
4.3	1-micron error probability in ncX scenario	61
A.1	Spin echo experiment	63
E.1	Generated signals of fascicle of identical axons $r = 0.5 \mu\text{m}$, $f_{in} = 0.7$. . .	74
E.2	Generated signals of fascicle of identical axons $r = 7.5 \mu\text{m}$, $f_{in} = 0.6$. . .	74
E.3	Generated signals of fascicle of identical axons $r = 18 \mu\text{m}$, $f_{in} = 0.7$. . .	75
E.4	Generated signals of crossing fascicles of identical axons $r = 0.5 \mu\text{m}$, $f_{in} =$ 0.5 , $\theta = \frac{\pi}{4}$	76
E.5	Generated signals of crossing fascicles of identical axons $r = 9 \mu\text{m}$, $f_{in} =$ 0.75 , $\theta = \frac{\pi}{2}$	76
E.6	Generated signals of crossing fascicles of identical axons $r = 16 \mu\text{m}$, $f_{in} =$ 0.65 , $\theta = \frac{3\pi}{8}$	77
E.7	Generated signals of Gamma-distributed atom of parameters $\mu_r = 0.532 \mu\text{m}$ and $f_{in} = 0.737$	78
E.8	Generated signals of Gamma atoms : effect of f_{in}	78
E.9	Generated signals of all Gamma-distributed atoms for $b = 2319 \text{ s mm}^{-2}$. .	79

E.10	Generated signals of spherical glial cells	80
G.1	Rotation of single-fascicle atoms	84
H.1	Superposition principle : easy setup	86
H.2	Superposition principle : difficult setup	87
H.3	Average rank in Gaussian scenario	88
H.4	α -level radius precision in Gaussian scenario	89

List of Tables

F.1	Acquisition protocols used for the generation of the dictionary	81
F.2	Microstructure parameters of the elementary atoms of the dictionary . . .	82

Abbreviations

CSF	Cerebrospinal fluid
CUSP	Cube and sphere (diffusion MRI)
DIAMOND	Distribution of anisotropic microstructural environments with DWI
DSI	Diffusion spectrum imaging
DTI	Diffusion tensor imaging
DWI	Diffusion-weighted imaging
DW-MRI	Diffusion-weighted magnetic resonance imaging
FID	Free induction decay
GM	Grey matter
GPD	Gaussian phase distribution
HARDI	High angular resolution diffusion imaging
MC	Monte Carlo
MCF	Multiple correlation function
MRI	Magnetic resonance imaging
ML	Maximum likelihood
NMR	Nuclear magnetic resonance
NODDI	Neurite orientation dispersion and density imaging
PGSE	Pulsed-gradient spin echo (sequence)
RF	Radio frequency
SE	Spin echo (sequence)
SGP	Short gradient pulse
SNR	Signal-to-noise ratio
STE	Stimulated spin echo (sequence)
TE	Echo time
WM	White matter

Physical Constants

Diffusivity of water	D	$=$	$2.0 \times 10^{-9} \text{m}^2 \text{s}^{-1}$	(commonly-used value in DWI)
Gyromagnetic ratio of hydrogen	γ	$=$	$2\pi \cdot 42.576 \times 10^6 \text{ rad s}^{-1} \text{T}^{-1}$	

Symbols

b	b-value	s m^{-2}
E	DW-MRI signal attenuation	/
$f_{in} (f_{ex})$	intra- (extra-) axonal volume fraction	
$\mathbf{g} = G\hat{\mathbf{g}}$	magnetic gradient	T m^{-1}
L_{step}	spins' fixed step length	m
N	number of spins (unless otherwise specified)	/
S_0	unweighted, reference T2-signal	/
T	number of time steps (unless otherwise specified)	/
$T1$	spin-lattice relaxation time	s
$T2$	spin-spin relaxation time	s
$\text{Tr } \mathbf{A}$	trace of matrix \mathbf{A}	/
δ	duration of gradient pulse	s
Δ	diffusion time	s
τ	time between RF pulses in spin-echo sequence	s
ω_0	Larmor angular frequency	rad s^{-1}
Ω	(bounded) diffusion environment	/

Introduction

Diffusion-weighted magnetic resonance imaging (DW-MRI) is a powerful non-invasive imaging tool sensitive to the diffusion of water molecules in tissues and able to provide valuable information about the structure of our brain at the microscopic scale, known as the *brain microstructure*. Earlier this year, DW-MRI images have enabled researchers [1] to establish a link between a certain type of multiple sclerosis and microstructural abnormalities: damage of small-diameter *axons*, which are the long "electric cables" constituting the circuitry of our brain, was found to be linked to cognitive impairment while damage of large-diameter axons was shown to be related to physical disability. Improving the characterization of our brain microstructure is of utmost importance for the better and earlier diagnosis of many neurological disorders.

In DW-MRI, we can decide in which direction and with which sensitivity we observe the diffusion of water by controlling certain experimental parameters. Each cubic pixel of the imaged brain, known as a *voxel*, is then associated with a vector of grayscale values, each value corresponding to specific acquisition parameters, as illustrated in Figure 1a. The challenge of microstructure imaging is then a classic *inverse problem*: based on P acquisitions of a given voxel (vector $y \in \mathbb{R}^P$ in Figure 1a), what can we infer about the underlying microstructure (schematically represented by the top-right drawing in Figure 1a) ? This problem is particularly challenging because the related *direct problem* of generating signals from given experimental parameters and microstructure configuration does not possess a general, closed-form analytic solution, even when the microstructure is reduced to an arrangement of simple geometric structures such as cylinders and spheres, as in Figure 1. Strong mathematical assumptions are then usually made in traditional parametric models. The presentation of microstructure imaging, its theoretical background, traditional models and open challenges will be the topic of Chapter 1.

This thesis proposes the preliminary exploration of a novel framework based on a large dictionary of pre-generated elementary DW-MRI signals such as illustrated in Figure 1b. We conjecture that sparse linear combinations of the signals arising from elementary

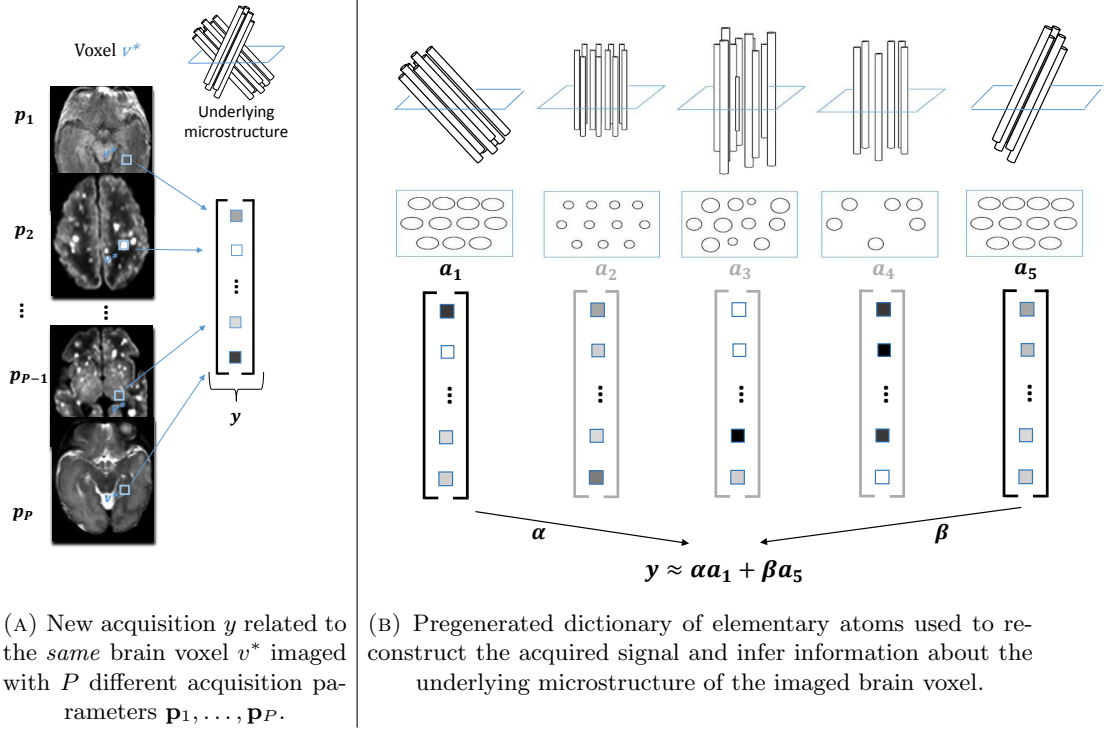


FIGURE 1: **Characterizing the brain microstructure through sparse dictionary matching.** We investigate whether the microstructure parameters of a new acquisition y , shown in (A), can be obtained by sparse linear combinations of signals a_1, a_2, \dots arising from simpler microstructure configurations, stored in the pre-computed dictionary shown in (B).

microstructure configurations can provide an accurate estimation of the microstructure parameters associated with newly-acquired data.

More specifically, this work focuses on the direct problem and is mainly concerned with the generation of a dictionary of DW-MRI signals based on methods making as few mathematical approximations as possible. Chapter 2 describes the hybrid method we designed for the accurate and efficient generation of DW-MRI signals, based on the combination of Monte Carlo (MC) simulations and more advanced analytical results. Chapter 3 provides a detailed description and justification of the experimental parameters and microstructure configurations we chose to integrate to our dictionary, including useful heuristics for reproducible and accurate MC simulations.

A last chapter provides a brief preliminary analysis of our generated dictionary. We investigate the feasibility of the proposed linear signal reconstruction framework by verifying whether superposition of elementary signals provides an accurate description of more complex signals. We then examine the accuracy and reliability of dictionary-matching in the presence of acquisition noise.

Chapter 1

DW-MRI : theoretical background

This chapter introduces the reader to the basic physical principles of magnetic resonance imaging (MRI) and to diffusion processes, the two building blocks of diffusion-weighted magnetic resonance imaging (DW-MRI), the medical imaging modality we will be making use of throughout this document. The emphasis is laid on two ways to mathematically describe clinical DW-MRI signals : a macroscopic and a microscopic approach. A final section presents the way DW-MRI is used for the finer study of our brain, an area known as brain microstructure imaging. We discuss open challenges and conclude by showing how a dictionary of synthetic DW-MRI signals such as the one we started developing in this thesis could help overcome these challenges.

The main results of this chapter may be summarized as follows. The first two sections may be omitted for a faster reading.

§ 1.1 *We introduce the basic physical principles of MRI and the fundamental spin echo (SE) sequence, which allows to measure the transverse magnetization due to the magnetic moments of hydrogen nuclei, abundant in the human body. The macroscopic Bloch equation, a linear ODE, provides a good phenomenological description of MRI signals.*

§ 1.2 *Diffusion processes can be accurately described at the macroscopic scale with the diffusion equation and at the microscopic scale through the random motion of molecules in thermal agitation, both approaches being closely related. Diffusion in the absence of physical barriers leads to Gaussian-distributed displacements.*

§ 1.3 *DW-MRI is based on the pulsed-gradient spin echo (PGSE) sequence, which adds external magnetic gradients to a traditional MRI sequence such as the SE sequence.*

Combining the Bloch equation with the diffusion equation leads to the macroscopic Bloch-Torrey equation, a non-trivial PDE. An equivalent microscopic description is obtained by leveraging the physics of diffusion at the microscopic scale. In the so-called slow-exchange limit, a superposition principle conveniently allows to compute the total signal for a whole domain as the sum of the signals from each sub-compartment.

§ 1.4 *The spatial resolution of DW-MRI is limited by hardware imperfections. Brain microstructure imaging consists in providing higher-resolution knowledge of the tissue structure of our brain (axons, glial cells, etc.) through appropriate mathematical modeling. Current challenges include a trade-off between complexity and accuracy, the choice of acquisition parameters (i.e. "machine settings") and the determination of the ultimate resolution of DW-MRI. We believe a large dictionary of elementary DW-MRI signals combined with efficient sparse-reconstruction techniques justified by the superposition principle could help with all three challenges.*

1.1 Basics of Magnetic Resonance Imaging

Magnetic resonance imaging (MRI) is a non-invasive medical imaging technique based on the nuclear magnetic resonance (NMR) properties of nuclei with an uneven number of protons and/or neutrons such as hydrogen, the most abundant element in the human body due to its presence in water molecules.

Such nuclei bear a non-zero spin quantum number and are characterized by a magnetic moment $\boldsymbol{\mu}_0$ induced by the spinning motion around their own axis. When a uniform and constant external magnetic field \mathbf{B}_0 is applied, conventionally along the z -axis of direction \mathbf{e}_z , the magnetic moments of these spin-bearing particles, commonly referred to as *spins*, tend to align with \mathbf{B}_0 . In the case of hydrogen nuclei (i.e. protons), spins either adopt a parallel alignment (low-energy state) or an anti-parallel alignment (high-energy state). Just like spinning-tops in a gravitational field experience a torque that causes them to rotate or *precess* around the axis of the gravitational field, spinning protons in an external magnetic field \mathbf{B}_0 will start to precess around the direction of \mathbf{B}_0 at an angular frequency ω_0 given by

$$\omega_0 = \gamma B_0,$$

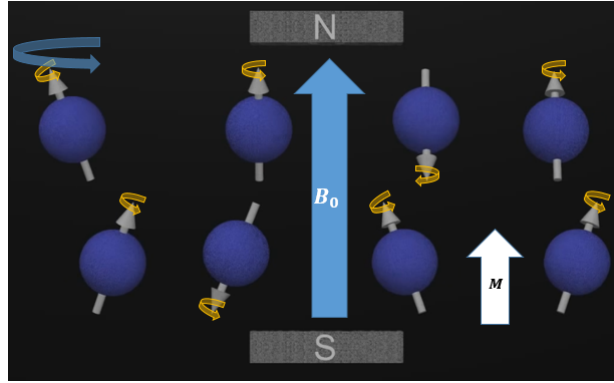


FIGURE 1.1: **A constant external magnetic field B_0 induces longitudinal magnetization.** The small orange arrows indicate the spinning motion inducing each proton's individual magnetic moment while the larger blue arrow (only drawn above the top-left spin for clarity) indicates the precession motion around B_0 at the Larmor frequency. The net magnetization M is longitudinal, parallel to B_0 because there are more parallel than anti-parallel spins in thermal equilibrium.

known as the *Larmor precession frequency*, γ being the *nuclear gyromagnetic ratio*, sometimes expressed as $\gamma = 2\pi\gamma$, where $\gamma = 42.58 \text{ MHz T}^{-1}$ for protons.

In the presence of such a magnetic field B_0 , the net magnetization M resulting from summing up all the individual spin's magnetic moments is longitudinal, i.e. $M = M_0 e_z$, because there are more low-energy, parallel protons than high-energy, anti-parallel protons in thermal equilibrium, as illustrated in Figure 1.1¹. The transverse magnetization in the xy -plane is zero because the phases of all the spins are randomly distributed.

1.1.1 The spin echo experiment

The goal of a spin echo (SE) experiment is to measure the transverse magnetization in the xy -plane. This is done by successively applying two radio-frequency (RF) pulses, as explained below. Detailed graphical illustrations are available in Appendix A.

We have seen that in a constant, uniform magnetic field B_0 , the net magnetization only has a longitudinal component. If a linearly-polarized magnetic field is applied in the xy -plane with an amplitude oscillating at the Larmor frequency, it can be shown that low-energy spins will make a transition to the higher-energy states and that the spins will tend to precess together in phase, thereby gradually tilting the net magnetization

¹Figure adapted from a video realized by Dr. Klioze, radiologist at the Eastern Virginia Medical School, resident at the University of Florida, available on his Youtube channel https://www.youtube.com/watch?v=J_aamnRJE8.

away from the z -axis towards the xy -plane [2]. A resonant magnetic field that is maintained long enough to convert the longitudinal magnetization into a purely-transverse magnetization in the xy -plane is called a 90° radio-frequency (RF) pulse. This transverse magnetization, rotating in the xy -plane at the Larmor frequency and known as the free induction decay (FID), is not directly measurable because of the severe decrease of its amplitude known as $T2^*$ -relaxation and resulting from the combined effect of

- static field non-uniformity due to local inhomogeneities of \mathbf{B}_0 and to magnetic susceptibility changes in the patient, making some spins experience a higher Larmor frequency and precess more rapidly than others, resulting in a rapid loss of phase coherence;
- intrinsic spin-spin quantum interactions, known as $T2$ -relaxation, which operate on a much slower timescale than the global $T2^*$ effects (see Figure 1.2).

In a spin echo sequence, at time $t = \tau$, a 180° RF pulse is applied to flip all the magnetic moments into the opposite direction in the xy -plane and reverse the direction of rotation, thereby compensating the effects of magnetic field inhomogeneities. After a time $t = 2\tau$ known as the echo time (TE), all the spins are thus in phase again : a "spin echo" is formed, consisting of a net transverse magnetization with an amplitude that can be experimentally measured since it has only been affected by intrinsic $T2$ -relaxation. It is worth noting that *$T2$ -effects do imply an exponential decrease of our useful signal and that consequently long echo times are not desirable* when dealing with noisy MRI acquisitions.

Such a sequence of RF pulses, known as a spin-echo acquisition sequence, forms the basis of virtually all the diffusion MRI experiments that we will be dealing with later on.

1.1.2 Macroscopic description : the Bloch equations

A phenomenological description of the evolution of the magnetization $\mathbf{M}(\mathbf{r}, t)$ in the presence of an external magnetic field $\mathbf{B}(\mathbf{r}, t)$ around a bulk point \mathbf{r} is given by the well-known macroscopic Bloch equations. From now on we assume that $\mathbf{B}(\mathbf{r}, t) = B(\mathbf{r}, t)\mathbf{e}_z$, i.e. the external magnetic field is directed along the z -axis, which means in particular that we are not looking at times when an RF pulse is being applied in the xy -plane. Making use of the complex notation $M_{xy}(\mathbf{r}, t) = M_x(\mathbf{r}, t) + iM_y(\mathbf{r}, t)$, the Bloch equations for the evolution of the components of the transverse magnetization constitute the

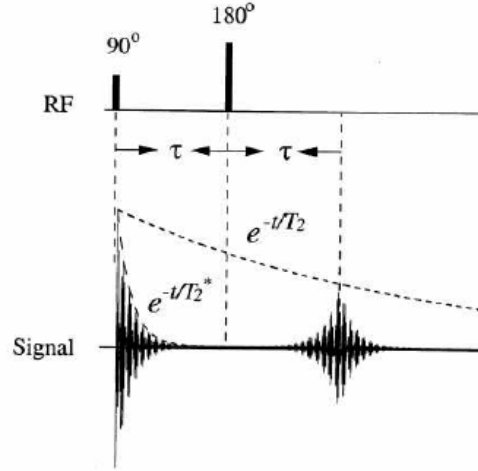


FIGURE 1.2: **T_2 -relaxation operates on a much slower time scale than T_2^* -relaxation and can be effectively measured.** Representation of the x -component of the transverse magnetization in a spin-echo sequence. The continuous curve is the hard-to-measure FID and the dashed curve is the effectively-measured signal [2].

following system of coupled linear ODE's [3, §2.3.2]

$$\frac{\partial M_{xy}}{\partial t}(\mathbf{r}, t) = \underbrace{-i\gamma B(\mathbf{r}, t)M_{xy}}_{\text{Larmor precession}} - \underbrace{\frac{M_{xy}}{T_2}}_{\text{T2-relaxation}}, \quad (1.1)$$

where γ is the gyromagnetic ratio of protons and T_2 is the spin-spin relaxation time of protons in the medium under investigation. This thus corresponds to the dashed curve in Figure 1.2.

In the SE experiment described above, we had $\mathbf{B}(\mathbf{r}, t) = B_0 \mathbf{e}_z$. This spatial profile will change when we later add magnetic gradients to the sequence in Section 1.3.

1.1.3 Statistical model for the acquisition noise

Modern phased-array MRI systems possess various coils able to acquire multiple images in parallel. The detected signal S_l in each of the N coils can be accurately described by [4]

$$S_l = A_l + n_l, \quad l = 1, \dots, N, \quad (1.2)$$

where n_l is a complex-valued white Gaussian noise process of variance σ_g^2 assumed identical for all N coils. A popular choice is to recover a final *magnitude* or *Sum-of-Squares (SoS)* signal M as $M = \sqrt{\sum_{l=1}^N |S_l|^2}$. If we assume that there is no correlation between the coils, M can be shown to follow a non-central Chi distribution of $2N$ degrees

of freedom with the following pdf [4, 5]

$$p_{\bar{\chi}}(m|\eta, \sigma_g, N) = \frac{m^N}{\sigma_g^2 \eta^{N-1}} \exp\left(-\frac{m^2 + \eta^2}{2\sigma_g^2}\right) I_{N-1}\left(\frac{m\eta}{\sigma_g^2}\right), \quad m > 0 \quad (1.3)$$

where $\eta = \sqrt{\sum_{l=1}^N |A_l|^2}$ is known as the underlying intensity and I_j is the j -th order modified Bessel function. It can be shown that the SoS reconstruction asymptotically (i.e. for large SNR) leads to an optimal SNR of η/σ_g , inducing a SNR gain of \sqrt{N} compared to the ratio A_l/σ_g in each coil [6].

1.2 Diffusion processes

Diffusion is a transport mechanism widely used in physics to describe the seemingly random movement of a substance in a given medium, for example water molecules in human body tissues. Two widely-used approaches to study diffusion will be useful later on : a macroscopic approach and a microscopic approach.

In the macroscopic, also known as phenomenological or continuous approach, one considers the general equation for mass conservation

$$\frac{\partial c}{\partial t}(\mathbf{r}, t) = -\nabla \cdot \mathbf{J}(\mathbf{r}, t), \quad (1.4)$$

where c is the concentration of the substance and \mathbf{J} its net flux, and Fick's law

$$\mathbf{J}(\mathbf{r}, t) = -\mathbf{D} \cdot \nabla c(\mathbf{r}, t), \quad (1.5)$$

stating that a substance tends to diffuse from regions of high concentration to regions of low concentration and where \mathbf{D} is a symmetric, positive-definite diffusion tensor. Combining (1.4) and (1.5) leads to the *diffusion equation*

$$\frac{\partial c}{\partial t}(\mathbf{r}, t) = \nabla \cdot (\mathbf{D} \cdot \nabla c(\mathbf{r}, t)) = D \Delta c(\mathbf{r}, t), \quad (1.6)$$

where the last equality only holds in the case of *isotropic diffusion*, with $D > 0$. This description of diffusion will be easily incorporated into the Bloch equations presented earlier and will lead to useful analytic results in diffusion-weighted imaging.

In the microscopic, also known as molecular or discrete approach, diffusion is treated as the motion of molecules colliding with each other under the effect of thermal agitation (Figure 1.3). The trajectory $\mathbf{r}(t)$ of each individual molecule is modeled as a discrete-time random walk on a discretized spatial grid, i.e. a succession of random

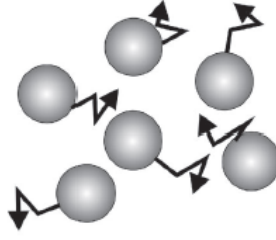


FIGURE 1.3: **Thermal agitation induces diffusion.** Diffusion resulting from seemingly random thermal motion of molecules [3].

”jumps” between adjacent positions on the spatial grid, each jump being independent from the past trajectory of the molecule (*Markov property*). The transition probabilities are generally taken to be spatially symmetric, such that $\mathbb{E}_{\mathbf{r}}[\mathbf{r} - \mathbf{r}_0] = 0$. The central limit theorem ensures that after a sufficiently long time t , the probability distribution of the displacement $\mathbf{r} - \mathbf{r}_0$ converges to a normal distribution of mean 0 and standard deviation proportional to \sqrt{t} , thus satisfying the hypotheses of a Brownian motion. This description is particularly well-suited for numerical investigations and it will form the basis of the Monte Carlo simulations used in diffusion-weighted imaging.

The two above descriptions are closely related. It can be shown for instance that the continuous diffusion equation can be retrieved in the limit of finer time and space discretization of a random walk, i.e. when $\Delta t, \Delta x \rightarrow 0$, if the ratio $\frac{\Delta x^2}{\Delta t}$ is kept constant [7].

We conclude this section by a remark on the difference between free, *Gaussian* diffusion and restricted diffusion. It can be shown that if the domain consists of the entire n -dimensional space \mathbb{R}^n , then the solution of (1.6) is a weighted average of the fundamental Gaussian kernel defined as [8, §2.3]

$$\begin{aligned} K(\mathbf{r}, \mathbf{r}_0, t) &= \frac{1}{\sqrt{(4\pi t)^n \det \mathbf{D}}} \exp\left(-\frac{1}{2}(\mathbf{r} - \mathbf{r}_0)^T \frac{\mathbf{D}^{-1}}{2t} (\mathbf{r} - \mathbf{r}_0)\right) \\ &= \frac{1}{(4\pi Dt)^{\frac{n}{2}}} \exp\left(-\frac{|\mathbf{r} - \mathbf{r}_0|^2}{4Dt}\right), \end{aligned} \quad (1.7)$$

for any $\mathbf{r}_0 \in \mathbb{R}^n$, where the last equality only holds in the isotropic case. This kernel can be interpreted as the probability for a particle to diffuse from \mathbf{r}_0 to \mathbf{r} over a time t . It can be verified that the mean displacement is 0 and that the mean-squared displacement is consistent with the microscopic random-walk description, since

$$\mathbb{E}_{\mathbf{r}}[\|\mathbf{r} - \mathbf{r}_0\|^2] = 2t \operatorname{Tr} \mathbf{D}.$$

However, if the diffusion is confined to a bounded domain $\Omega \subset \mathbb{R}^n$, such as for instance

water molecules in a cylindrical axon of the brain where the axonal membrane acts as a physical barrier, the solution *will no longer be Gaussian*. This is where the whole interest of diffusion-weighted imaging lies.

1.3 Diffusion-Weighted Imaging

Diffusion-weighted magnetic resonance imaging (DW-MRI) or diffusion-weighted imaging (DWI) is a non-invasive medical technique that aims at probing the diffusion of water molecules in biological tissues. It combines classical MRI sequences of radio-frequency (RF) pulses such as the spin echo (SE) sequence presented in Section 1.1.1 with successive applications of non-uniform magnetic fields serving as a way to "label" or "spatially encode" the spin-bearing particles (*spins*) of the sample. The measured signal becomes sensitive to the diffusing motion of molecules through the tissues occurring during the acquisition, making it possible to infer information about the underlying tissue microstructure, i.e. the physical barriers that affected the diffusion during the acquisition.

This section first presents the DW-MRI acquisition sequence we have used for all of our studies : the *PGSE sequence*. After that the three main mathematical tools used in this thesis are discussed : a microscopic description of the DW-MRI signal measured at the end of a PGSE sequence, an equivalent macroscopic description that will allow us to give an analytic expression of the DW-MRI signal in the absence of diffusion barriers, thereby introducing the well-known *b-value*, and lastly the so-called *superposition principle* for DW-MRI signals.

1.3.1 The pulsed-gradient spin echo sequence

In a pulsed-gradient spin echo (PGSE) sequence, two linear magnetic fields of magnitude $B_1(\mathbf{r}, t) = \mathbf{g} \cdot \mathbf{r}$ are successively superposed to the constant, uniform magnetic field B_0 already present along the z -axis, through two applications of a uniform magnetic gradient \mathbf{g} . A PGSE sequence is characterized by the parameters $\mathbf{p}_{pgse} = (\mathbf{g}, \Delta, \delta)$, schematically illustrated in Figure 1.4 and described as follows

- \mathbf{g} , the 3-dimensional phase-encoding magnetic gradient, usually represented by a unit direction $\hat{\mathbf{g}}$ and a magnitude G ;
- δ , the duration of each of the magnetic gradient pulses ;
- Δ , the time between the onsets of the pulses, also known as the diffusion time.

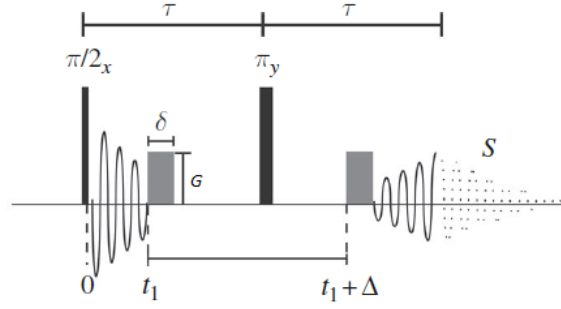


FIGURE 1.4: **Probing diffusion by applying magnetic gradients.** A classical PGSE sequence consists of two magnetic gradients of intensity G and duration δ applied respectively after the $\pi/2$ - and π - RF pulses of the SE sequence. Figure adapted from [3, §2.2.4.1].

The first gradient pulse dephases the spins that were precessing together after the 90° RF pulse by making them experience distinct Larmor frequencies. The second gradient pulse is of the same duration, direction and intensity as the first one but since the rotation of the spins has been inverted by the 180° RF pulse, its effect is to refocus all the spins. If the spins of the sample were stationary, their phase would be perfectly refocused after the application of the second pulse and the measured signal would be that of a classical SE sequence, thus only affected by T_2 -relaxation (see Section 1.1.1). However, since they are actually experiencing random diffusion through the tissues, the refocusing is imperfect and a loss of signal is observed.

Other basic MRI sequences such as the stimulated echo (STE) sequence make use of a different series of RF pulses but the overall effect of the magnetic gradient pulses remains the same. We now proceed to mathematically formulate the signal attenuation due to diffusion in a PGSE experiment.

1.3.2 Microscopic description : random walk

This mathematical formulation builds on the microscopic description of the diffusion of particles discussed in Section 1.2. We note $\mathbf{B}_1(\mathbf{r}, t) = (f(t)\mathbf{g} \cdot \mathbf{r})\mathbf{e}_z$ the linear magnetic field superposed to the constant, uniform field $\mathbf{B}_0 = B_0\mathbf{e}_z$. In our PGSE experiment, the temporal profile of the gradient $f(t)$ is a piecewise-constant function taking the values 0, 1 and -1 so as to match the gradient profile of Figure 1.4, where the negative sign accounts for the inverting RF pulse at time τ .

Let us assume N spin-bearing protons are evolving in Brownian motion in a given environment, such as a cube, or *voxel*, of human brain. At time $t = 0$ right after the first 90° RF pulse, all N spins are precessing together at the Larmor angular frequency

$\omega_0 = \gamma B_0$. The dephasing ϕ_k of each spin at the echo time $t = TE = 2\tau$ is

$$\begin{aligned}\phi_k(TE) &= \gamma \int_0^{TE} B_1(\mathbf{r}_k(t), t) dt \\ &= \underbrace{\gamma \int_{t_1}^{t_1+\delta} \mathbf{g} \cdot \mathbf{r}_k(t) dt}_{\text{gradient dephasing}} - \underbrace{\gamma \int_{t_1+\Delta}^{t_1+\Delta+\delta} \mathbf{g} \cdot \mathbf{r}_k(t) dt}_{\text{gradient rephasing}},\end{aligned}\quad (1.8)$$

where $\mathbf{r}_k(t)$ is the random trajectory of spin k , for $k = 1, \dots, N$, and is *completely independent from the applied magnetic gradient pulses*. The minus sign reflects the effect of the inverting 180° RF pulse applied at $t = \tau$. The uniform magnetic field \mathbf{B}_0 contributes equally to the phase of each spin by a factor $\gamma B_0 \cdot TE$ and can thus be lumped into an initial reference phase ϕ_0 that does not affect the measured signal.

Once the phase ϕ_k of each spin is known, making use of the complex notation $S = M_x + iM_y$ for the transverse components of the net magnetization, the attenuation $E(\mathbf{p}_{pgse}; \Omega)$ of the transverse magnetization associated to the PGSE sequence of parameters \mathbf{p}_{pgse} in the diffusion environment Ω is obtained as

$$E(\mathbf{p}_{pgse}; \Omega) = \frac{S(TE)}{S_0} = \frac{e^{-\frac{TE}{T_2}} \sum_{k=1}^N \frac{M_0}{N} e^{i\phi_k}}{M_0 e^{-\frac{TE}{T_2}}} = \frac{1}{N} \sum_{k=1}^N e^{i\phi_k}, \quad (1.9)$$

where $M_0 = M_{x0} + iM_{y0}$ is the net magnetization in the xy -plane right after the first 90° RF pulse resulting from the equal contributions $\frac{M_0}{N}$ of the N spins, and where S_0 is the reference T_2 -weighted signal associated with that sample, when no gradients are applied.

Equation (1.9) could be rewritten as a continuous expectation over ϕ : $E(\mathbf{p}_{pgse}; \Omega) = \mathbb{E}_\phi[e^{i\phi}]$. However, there is generally no closed-form expression for the probability distribution $P_\Phi(\phi)$ and more or less valid mathematical approximations must be used such as the SPG or the GDP approximations to estimate it, which we will discuss in Section 2.1. We note that Equations (1.8) and (1.9) only require as input the Brownian trajectories $\mathbf{r}_k(t)$ which only depend on the underlying tissue microstructure Ω . The Monte Carlo simulations we perform in subsequent chapters for the generation of DW-MRI signals will precisely consist in generating these N random trajectories in Ω .

1.3.3 Macroscopic description : the Bloch-Torrey equations

We combine the phenomenological Bloch equations presented in Section 1.1.2 with the diffusion equation derived in Section 1.2 to obtain the macroscopic Bloch-Torrey system of coupled linear PDE's for the evolution of the complex-valued transverse magnetization

$$M_{xy} = M_x + iM_y \text{ [3, §2.3.2]}$$

$$\frac{\partial M_{xy}}{\partial t}(\mathbf{r}, t) = \underbrace{\nabla \cdot (\mathbf{D} \cdot \nabla M_{xy}(\mathbf{r}, t))}_{\text{diffusion}} \underbrace{- i\gamma B_1(\mathbf{r}, t) M_{xy}(\mathbf{r}, t)}_{\text{gradient encoding}}, \quad (1.10)$$

where $B_1(\mathbf{r}, t) = f(t)\mathbf{g} \cdot \mathbf{r}$. We left out the T_2 -relaxation term since it only affects the measured signal by a known exponential factor as well as the contribution of B_0 since it only gives the oscillating component $e^{i\gamma B_0 t} = e^{i\omega_0 t}$ of the FID whereas we are rather interested in its amplitude (see Figure 1.2).

If the spatial domain is bounded, e.g. a sphere to model a glial cell in the human brain, we express the conservation of mass through the general Robin boundary condition

$$\underbrace{(\mathbf{D} \cdot \nabla M_{xy}(\mathbf{r}, t)) \cdot \hat{\mathbf{n}}}_{\text{diffusion}} + \underbrace{K M_{xy}(\mathbf{r}, t)}_{\text{permeability}} = 0, \quad (1.11)$$

where $\hat{\mathbf{n}}$ is the outward unit normal and K denotes the molecules' probability of crossing the boundary. In the remainder of this thesis, only the Neumann condition corresponding to perfectly reflecting cellular membranes are considered setting $K = 0$. The attenuation $E(\mathbf{p}_{pgse}; \Omega)$ of the transverse magnetization associated to the PGSE sequence of parameters \mathbf{p}_{pgse} in the diffusion environment Ω at the echo time TE is obtained as

$$E(\mathbf{p}_{pgse}; \Omega) = \frac{1}{S_0} \int_{\Omega} M_{xy}(\mathbf{r}, TE) d\mathbf{r}, \quad (1.12)$$

where S_0 is the reference T_2 -weighted signal associated with that sample, i.e. when no gradients are applied. The Bloch-Torrey equation is in general difficult to solve for arbitrary domains Ω , making synthetic generation of DW-MRI signals in arbitrary geometries a challenging task.

Solution for free diffusion

The Bloch-Torrey equations (1.10) can be solved in the case of so-called free, *Gaussian* diffusion (see Section 1.2). One obtains the following attenuation of the measured signal [3, §2.3.2, §4.4.1]

$$\begin{aligned} E(\mathbf{p}_{pgse}; \mathbb{R}^n) &= e^{-b_{pgse} \hat{\mathbf{g}}^T \mathbf{D} \hat{\mathbf{g}}} \quad (\text{anisotropic case}), \\ &= e^{-b_{pgse} D} \quad (\text{isotropic case}), \end{aligned} \quad (1.13)$$

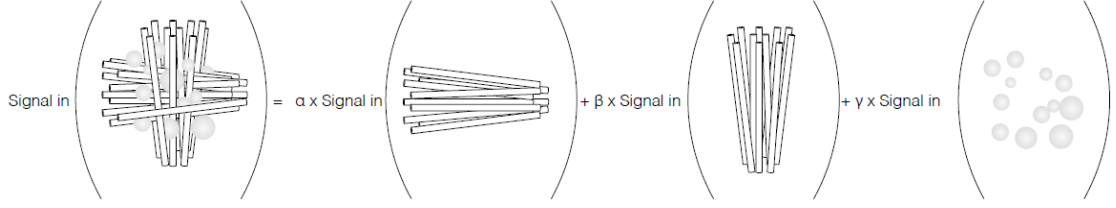


FIGURE 1.5: **Superposition of DW-MRI signals holds with impermeable membranes.** The total normalized signal is the sum of the DW-MRI attenuation of each compartment weighted by the respective volume fractions α, β and γ . In the context of brain imaging, the cylinders could represent axons, organized in bundles known as fascicles while spheres could model glial cells. We do not consider the signal arising from water molecules in the extra-cellular space, i.e. outside the spheres and cylinders represented in the figure.

where $\hat{\mathbf{g}}$ is the unit gradient direction and where the quantity b_{pgse} is the well-known b-value associated with the PGSE sequence, defined as

$$b_{pgse} = (\gamma \delta G)^2 (\Delta - \delta/3). \quad (1.14)$$

The solution presented here in the case of *free* diffusion is used in a wide range of mathematical models used to approximate DW-MRI signals in the case of *restricted* diffusion as we will see in Section 1.4.1. The parameters $\hat{\mathbf{g}}$ and b_{pgse} could be interpreted as the direction and sensitivity with which we probe the diffusion of water in tissues, as we hinted at in the introduction of this document.

1.3.4 Superposition principle

If the diffusion environment Ω can be expressed as the union of K mutually-disjoint compartments $\Omega_1, \dots, \Omega_K$ with perfectly-reflecting boundaries, then the total signal attenuation $E(\mathbf{p}_{pgse}; \Omega)$ associated to the PGSE sequence of parameters \mathbf{p}_{pgse} in the diffusion environment Ω is obtained as

$$E(\mathbf{p}_{pgse}; \Omega) = \sum_{i=1}^K f_i E(\mathbf{p}_{pgse}; \Omega_i), \quad (1.15)$$

where $f_i = \frac{|\Omega_i|}{|\Omega|}$, for $i = 1, \dots, K$, are the volume fractions of each compartment, as illustrated in Figure 1.5. This result holds if the T_2 characteristic time and the proton density is uniform across all subdomains Ω_i .

In practice, cell membranes are seldom completely impermeable. However, at the time scale of a DW-MRI acquisition, typically of the order of 100 ms, very little molecule transfer between compartments occurs. This is referred to as the *slow-exchange limit* and will be assumed throughout all subsequent developments.

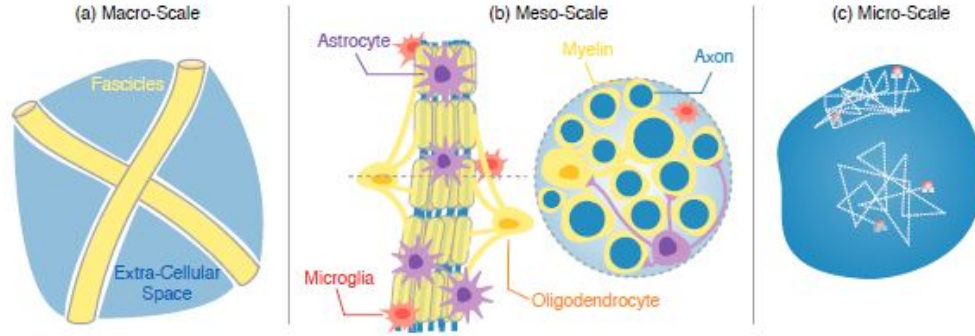


FIGURE 1.6: **Studying the brain WM is a multi-scale problem.** (a) At the macroscopic scale (spanning multiple voxels), multiple fascicles of axons are present alongside the extra-cellular space, as well as partial volumes of cerebrospinal fluid (CSF) and/or grey matter. (b) At an intermediate scale (typically one voxel), we observe the presence, within a fascicle, of various axons, possibly covered with a myelin sheath, as well as several types of glial cells (astrocytes, microglia, oligodendrocytes). The extra-axonal space usually refers to the space within a fascicle, outside the axons and also contributes to DW-MRI signals. (c) The water molecules diffusing in the intra-axonal space, at typical sub-voxel scales of a few micrometers, are at the heart of DW-MRI acquisitions. [9].

1.4 Microstructure imaging : open challenges

The *brain microstructure* describes the organization of cellular structures within the brain. It chiefly consists of *neurons*, nervous cells possessing a cell body (*soma*) and a long "electric cable" known as *axon*, and *glial cells*, which among others produce the *myelin*. Axons can be covered with a myelin sheath and are usually bundled together in fiber tracts known as *fascicles*, as shown in Figure 1.6. The main difference between the gray matter (GM) and the white matter (WM) is that the GM possesses neuron somas while the WM does not. The finer study of the brain microstructure (particularly that of the WM) based on DW-MRI acquisitions is referred to as *brain microstructure imaging*.

In practice, a number N of scalar DW-MRI images are acquired with distinct combinations of parameters $\mathbf{p}_1, \dots, \mathbf{p}_N$, with N determined so as to ensure bearable acquisition times for patients and reasonable financial costs. The volume of the imaged brain is divided into cubic subregions known as *voxels* of typical volume $\Delta v \approx 8 \text{ mm}^3$. It can be shown [2] that the signal-to-noise ratio (SNR) of a general MRI acquisition is proportional to Δv , thus limiting the MRI spatial resolution. The challenge of microstructure imaging is in a way to overcome this limitation and to provide higher-resolution insights through the characterization of the tissue microstructure at the *sub-voxel* level (Figure 1.6) : we are interested in obtaining the number and orientation of fascicles inside the voxel, the mean radius and radius heterogeneity of the axons making up each fascicle, the intra- and extra-axonal volume fractions, the volume fraction of glial cells, etc.

Traditionally, a parametrized analytical expression is established relating the brain microstructure and the acquisition parameters to the measured DW-MRI signal. The model parameters are then estimated through a continuous optimization using metrics that attempt to take the acquisition noise into account.

In this section we briefly present the most widely-used classes of continuous models of the brain microstructure, categorized as *phenomenological* and *microstructural*. From this basis, we briefly discuss three current challenges in microstructure imaging. We conclude this chapter by a section explaining how the generation of a dictionary of high-accuracy synthetic DW-MRI signals could improve on these limitations.

1.4.1 Examples of traditional models

Most traditional models are phenomenological models, i.e. models that try to fit a mathematical expression to the signal with parameters that do not directly represent the biological microstructure. Microstructural models, on the other hand, provide a more direct link between the brain microstructure and the observed signal, usually at the expense of a more complex mathematical formulation. We briefly present a few examples of each type of model and conclude by identifying a first challenge in microstructure imaging.

Phenomenological models

The prime example of a phenomenological model is the diffusion tensor imaging model (DTI), which models the DW-MRI signal attenuation of a PGSE sequence as [10]

$$E_{DTI} = e^{\gamma^2 \delta^2 (\Delta - \delta/3) \mathbf{g}^T \mathbf{D} \mathbf{g}}, \quad (1.16)$$

and fits a symmetric, positive-definite diffusion tensor \mathbf{D} to a set of at least 6 DW-MRI acquisitions, for each voxel. This model comes from the exact solution of the Bloch-Torrey equations for free, anisotropic diffusion presented in Section 1.3.3 and is reasonably accurate for voxels containing one single fascicle of axons, the principal eigenvector of \mathbf{D} turning out to be a good indicator of the fascicle's principal direction. However, at typical clinical spatial resolutions, voxels containing crossing fascicles could account for 60 to 90% of all voxels, as recently suggested in [11]. A direct extension of the DTI model for multiple crossing fascicle is the multi-tensor model of the form [12, 13]

$$E_{mDTI} = \sum_{i=1}^N f_i e^{\gamma^2 \delta^2 (\Delta - \delta/3) \mathbf{g}^T \mathbf{D}_i \mathbf{g}}, \quad (1.17)$$

where the f_i are the volume fractions of each fascicle. More recently, the DIAMOND model [14] proposed a much refined extension of a multi-tensor model through the generative formula

$$E_{DMD} = \int_{\mathbf{D} \in \mathcal{S}_3^+} \sum_{j=0}^N f_j P_{p^j, \Sigma^j}(\mathbf{D}) \exp(-b \mathbf{g}^T \mathbf{D} \mathbf{g}) d\mathbf{D}, \quad (1.18)$$

representing the signal arising from N fascicles ($j = 0$ corresponding to the isotropic diffusion of free water) of volume fractions f_j , in the slow-exchange limit (see Section 1.3.4). The heterogeneity of axons within a fascicle is represented by a matrix-variate Gamma distribution P_{p^j, Σ^j} over the space of positive-definite symmetric matrices \mathbf{D} , as histological studies have revealed that axon radii within a fascicle tend to follow Gamma distributions [15, 16]. It can be shown that the integral in (1.18) can be solved analytically, simplifying the optimization of the model parameters.

All these phenomenological models have reasonably simple mathematical formulations and lead to tractable parameter optimizations. However, these estimated parameters (the tensors \mathbf{D}_i , the fractions f_i , or the parameters of the matrix-variate Gamma distribution) represent diffusion features rather than actual microstructural features such as axon radii. What they represent biologically is sometimes unclear.

Microstructural models

Microstructural models are generally multi-compartment models that take advantage of the superposition principle presented in Section 1.3.4. One example thereof is the ActiveAx model [17] which considers the signal contributions from 4 compartments

- intra-axonal (A_1) : DW-MRI signal due to water molecules confined within a cylinder of radius r calculated with the GDP approximation mentioned in Section 1.3.2 and further discussed in Section 2.1;
- extra-axonal I (A_2) : also known as the *hindered* compartment, models the contribution of molecules that evolve near cylindrical axons through a slightly-modified DTI model with diffusion tensor \mathbf{D} having its principal eigenvector parallel to the cylinders of the intra-axonal compartment;
- extra-axonal II (A_3) : *cerebrospinal fluid* (CSF) compartment, corresponding to freely-diffusing molecules in an isotropic brain fluid, using the formula $A_3 = e^{-bD}$ (see (1.13), Section 1.3.3);
- extra-axonal III (A_4) : stationary molecules, for instance molecules trapped in cellular membranes : $A_4 = 1$.

The slow-exchange hypothesis is assumed and the total signal attenuation of the ActiveAx model E_{AX} is calculated as

$$E_{AX} = \sum_{i=1}^4 f_i A_i, \quad (1.19)$$

where the f_i are the volume proportions of each compartment within the voxel under study. This model thus only assumes one principal fascicle of axons.

In the NODDI model [18], only the first 3 compartments of the ActiveAx model are present but with different mathematical formulations. The model assumes axons of zero radius and parallel diffusivity $d_{//}$ and introduces an orientation distribution function $f(\mathbf{n})$ to capture the dispersion of axons about one principal direction in a fascicle. The intra-axonal signal A_1 makes use of the solution (1.7) for Gaussian diffusion in \mathbb{R} , after projecting the gradient \mathbf{g} onto the direction \mathbf{n} of each axon

$$A_1 = \int_{S^2} f(\mathbf{n}) e^{-(\gamma\delta)^2 (\Delta - \frac{\delta}{3}) d_{//} \|\mathbf{g} \cdot \mathbf{n}\|^2} d\mathbf{n}. \quad (1.20)$$

The signal S_2 of the hindered compartment is computed with a DTI model averaged by the same orientation distribution function $f(\mathbf{n})$ and the signal S_3 is identical to the ActiveAx model.

These microstructural models provide more insight into the underlying microstructure but present much more complicated mathematical formulations. The GPD formula for a cylinder used in ActiveAx for instance involves the exponential of an infinite sum where each term has a $\frac{1}{r^2}$ dependence with the radius, which is a parameter of the model. To maintain an acceptable complexity, strong assumptions such as assuming only one fascicle of axons or NODDI's zero-radius assumption have to be made.

In both types of model, there is thus a trade-off between obtaining accurate and quantitative information on the underlying microstructure and resorting to (over-)simplifications in order to make the parameter estimation mathematically tractable. This first challenge is further developed in our next section, followed by two more challenges that are more model-independent : the choice of optimal DW-MRI acquisition sequences and the intrinsic resolution of microstructure imaging.

1.4.2 Challenges of microstructure imaging

We present three current challenges in microstructure imaging.

Challenge I : accuracy-complexity trade-off

We have seen that establishing models that more closely reflect the underlying microstructure involves handling more complex mathematical formulations. The related parameter optimizations used in microstructural models are typically non-convex. The optimization algorithms may then not always converge to global maxima and the estimated parameters therefore suffer from uncontrolled uncertainties. This finally boils down to a traditional dilemma in the mathematical modeling of physical phenomena : choosing between exactly solving an approximate model or approximately solving a more accurate model.

Challenge II : optimization of acquisition sequences

Recall that a PGSE sequence has 5 degrees of freedom through the parameters $(\mathbf{g}, \Delta, \delta)$. If N DW-MRI acquisitions are allowed (limited by acquisition time or cost restrictions, for instance), one could wonder how to select the *optimal* N PGSE sequences $\{\mathbf{g}_i, \Delta_i, \delta_i\}_{1 \leq i \leq N}$. All N acquisitions could for instance be realized with the same b-value, as defined in Equation (1.14), with varying or fixed gradient directions, with fixed or distinct diffusion times Δ , etc. In [12, 17, 18] for example, specific acquisition protocols are designed that are supposed to be optimal for the parameter estimation of their particular models. However, it remains unclear whether some "model-independent", universal optimal protocol exists. We will attempt to explore this issue in Chapter 4.

Challenge III : intrinsic resolution of microstructure imaging

A question related to the previous issue is that of the very resolution of brain microstructure imaging. It has been shown that acquisition with a single b-value does not allow to distinguish properties of different crossing fascicles within a voxel [13, 14]. However, it remains unclear whether a DW-MRI acquisition with multiple b-values and/or multiple diffusion times allows to distinguish parameters of interest in a noise-free and noisy scenario. In other words, we currently do not know whether there are some intrinsic limitations in microstructure imaging wherein multiple microstructural configurations lead to the same diffusion signal regardless of the choice of acquisition parameters. This will be partially investigated in Chapter 4.

1.4.3 A dictionary of synthetic signals for microstructure imaging

The present thesis aims at the generation of high-accuracy synthetic DW-MRI signals based on the PGSE sequence for a wide range of PGSE parameters $(\mathbf{g}, \Delta, \delta)$ and a considerable number of elementary *microstructural atoms*. More details will be provided in Chapter 3, but for the sake of illustration, one atom could be for instance the signal associated with fascicles made of parallel axons of radius r_1 , a second atom could be similar but for axons of radius r_2 , etc. As such, these atoms could be viewed as possible compartments for the aforementioned microstructural models, after discrete sampling of their parameter space (the axon radius r in our example). Such a dictionary could help overcome the previously identified limitations of microstructure imaging in the following way.

- **Accuracy-complexity (Ch. I)** : we investigated and selected some of the most *quantitatively-accurate* methods available for the synthetic generation of DW-MRI : Monte Carlo (MC) simulations and the Multiple Correlation Function (MCF) approach [22], combined in an efficient hybrid method presented in Chapter 2. These methods, as opposed to the formulations presented earlier, require little to no simplifying assumptions on the underlying tissue microstructure. MC simulations in particular are widely used in the literature as pseudo ground truth for the validation of models such as those described in Section 1.4.1. It is conjectured that the superposition principle can be used to accurately express DW-MRI signals as weighted sums of elementary atoms of our dictionary. The validity of this hypothesis will be explored in Section 4.1. Cumbersome continuous optimization routines could then be replaced by much more *efficient sparse-optimization-like* techniques on large dictionaries, as discussed in [23]. Finally, a dictionary-based framework would allow to account for the *actual structure of the acquisition noise*, through direct Maximum Likelihood estimation for instance, as investigated in Section 4.2.
- **Optimal acquisition parameters (Ch. II)** : since a large number of PGSE parameters $(\mathbf{g}, \Delta, \delta)$ are tested for each dictionary atom, such a dictionary allows us to further investigate the determination of the subset of parameters that would lead to the most precise characterization of the brain microstructure with or without noise. An preliminary study is carried out in Section 4.2.
- **Intrinsic resolution of microstructure imaging (Ch. III)** : if two atoms of our dictionary remain "mathematically indistinguishable" for all the combinations of PGSE parameters we tested, then there is little hope that any algorithm will be

able to properly discriminate between these two types of microstructure configurations based on DW-MRI acquisitions using the PGSE sequence. We perform an exploratory analysis of how accurately microstructure properties can be recovered based on our dictionary in Section 4.2.

Chapter 2

Synthetic generation of DW-MRI signals : a hybrid approach

This chapter tackles the problem of synthetically and efficiently generating an accurate DW-MRI signal $E(\mathbf{p}_{pgse}; \Omega)$ from given PGSE parameters $\mathbf{p}_{pgse} = (\mathbf{g}, \Delta, \delta)$ and a given diffusion environment Ω .

In Chapter 1, the problem was formulated in two different ways : a first approach based on a microscopic description of water molecules in Brownian motion, a second one based on a macroscopic linear PDE. It was shown that the second approach leads to a simple closed-form solution in the case of free diffusion. However, we are now interested in the much more complex case of bounded domains Ω containing diffusion barriers, in particular cylindrical domains since, at the scale of a voxel, the axons of the brain can be reasonably modeled as long, thin cylinders. The slow-exchange hypothesis is assumed throughout.

The main results of this chapter may be summarized as follows.

§ 2.1 *Traditional approaches such as the GPD and SGP approximations that have long been considered as standards in DW-MRI do not present the desired accuracy and even require solving a more complex equation than in the method of Section 2.3.*

§ 2.2 *Monte Carlo (MC) simulations have over the last few years become a reference for the generation of pseudo ground truth in DW-MRI. MC techniques are of great flexibility as they allow to simulate, in theory, any diffusion environment and any DW-MRI acquisition sequence. Its drawbacks are found, in present implementations such as in the Camino toolkit [24, 25], to be extremely high, sometimes barely manageable, computational loads.*

- § 2.3 Based on more advanced theoretical results, the multiple correlation function (MCF, [22]) approach proves to be very-well suited for the generation of DW-MRI signals in simple geometries such as cylinders and spheres, of utmost importance in brain microstructure imaging. The method is however not applicable to more complex geometries such as the extra-axonal space.
- § 2.4 Our hybrid approach combines intra-axonal signal obtained by the MCF approach with extra-axonal signal obtained by MC simulations through the superposition principle. We show that for a given computation time, the obtained precision of our method is superior to that of usual all-out MC simulations. Conversely, we show that similar levels of accuracy are obtained in less simulation time than by conventional MC simulations.

2.1 Limitations of traditional data synthesis techniques

We first stress that all DTI-like formulations based on positive-definite symmetric tensors such as those presented in Section 1.4.1 are not considered as potential tools for signal generation because they do not even consider restricted diffusion with actual physical barriers. It was suggested in [26] for instance that models incorporating real, physical intra-axonal restriction generally explain the data better than those that do not.

Other mathematical methods have been developed to consider the effect of actual physical barriers such as the membranes of axons, blocking the passage of water molecules undergoing diffusion. Such methods include the short-gradient pulse (SGP) approximation and the Gaussian phase distribution (GPD) approximation and are described in more details in Appendix B. Although these two methods have been - and are still - extensively used in the literature, they are only valid under sometimes restrictive hypotheses. SGP formulas are only accurate for very short values of gradient duration δ and GPD results are typically reliable for very short or very long diffusion times Δ , while we would like to test any PGSE parameters in our dictionary of DW-MRI signals and not restrict ourselves to limited ranges of values.

In addition, both methods require solving the diffusion equation, a PDE with time and space dependence. We will see in Section 2.3 that we can obtain better results by solving a simpler problem with no time dependence, the Laplace eigenvalue problem.

2.2 Monte Carlo simulations

We present the principles of Monte Carlo (MC) simulations for the generation of DW-MRI signals and discuss their advantages and limitations.

2.2.1 Description

MC simulations are directly based on the microscopic description of DW-MRI signals presented in Section 1.3.2 and mainly consists in generating the trajectories of N spins or *random walkers*, initially uniformly distributed across the geometry, by means of a discrete-time random walk.

If $\{0=t_0, t_1, \dots, t_{T-1}, t_T=TE\}$ is a partition of the time interval from the initial 90° -pulse to the echo time (TE), then from a random initial position $\mathbf{r}_0 = \mathbf{r}(t_0)$ in the domain Ω , each spin's trajectory is updated as

$$\mathbf{r}(t_{i+1}) = \mathbf{r}(t_i) + \Delta \mathbf{r}_i, \quad (2.1)$$

where each step $\Delta \mathbf{r}_i$ is of random orientation and of fixed length

$$L_{step} = \sqrt{2nD\delta t_i}, \quad (2.2)$$

with n the spatial dimension of the diffusion environment and $\delta t_i = t_i - t_{i-1}$ for $i = 1, \dots, T$. As the steps sum up, the central limit theorem ensures that the distribution of all n components of the position $\mathbf{r}(t)$ at time t will tend to a Gaussian distribution of mean zero (by symmetry) and of variance $2Dt$ as expected from Brownian motion (see Section 1.2). The accumulated phase ϕ of each spin is then updated at each iteration $i = 1, \dots, T$ by the discretization of the time integral (1.8) through a rectangle-like method

$$\phi(t_{i+1}) = \phi(t_i) + \gamma f(t_i) \mathbf{g} \cdot \mathbf{r}(t_i) \delta t_i, \quad (2.3)$$

where $f(t)$ is the temporal profile of the applied magnetic gradient, and would take the values 0, 1 or -1 in a PGSE sequence, as in Figure 1.4 on page 11. The final signal attenuation is computed as the sample mean of $e^{i\phi}$

$$E(\mathbf{p}_{pgse}; \Omega) = \frac{1}{N} \sum_{k=1}^N e^{i\phi_k}.$$

In the context of synthetic generation, it actually suffices to compute the real component of the signal since it has been shown that DW-MRI signals are real and positive under relatively mild assumptions, usually met in our experiments [27]. Also note that the

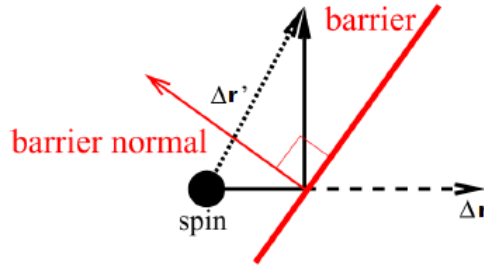


FIGURE 2.1: **Membranes are considered perfectly reflecting.** Spins that encounter a barrier during a step update $\Delta \mathbf{r}$ are elastically reflected and take an effective step $\Delta \mathbf{r}'$. Figure adapted from [25].

trajectory of each spin is independent from the computation of its accumulated phase. One set of spins dynamics can thus be used to compute the signals associated to several different sets of PGSE parameters $(\mathbf{g}, \Delta, \delta)$.

Since we consider perfectly impermeable membranes, spins that encounter a barrier are elastically reflected, as illustrated in Figure 2.1.

Implementing MC simulations in arbitrary confining geometries is a challenging task and lied outside the scope of this Master's thesis. We therefore based our subsequent experiments on the UCL Camino Diffusion MRI Toolkit [24, 25], the only available and validated implementation of the above-described method as of now, to our knowledge. The following paragraph discusses the capabilities and limitations of the Camino software and of MC techniques in general, in the context of the generation of a *large quantity* of DW-MRI signals.

2.2.2 Advantages and limitations

The main advantages of MC simulations can be listed as

+ accuracy: the involved formulas for the generation of the random trajectory and the phase accumulation have sound theoretical foundations and results will thus be correct up to a numerical discretization error (Equation (2.3)), which should diminish as the time steps δt_i are made smaller, and a statistical sampling error, which should diminish with the number of simulated spins N . MC simulations are often used in the literature as the ground-truth against which simpler parametric models are assessed, such as in [17, 28];

+ flexibility: the flexibility of MC techniques also make them appealing. Any sequence of magnetic gradients can be implemented and arbitrary geometries can be modeled, such

as the extra-axonal space between parallel cylindrical axons (see Figure 1.6 on page 15), which we will extensively use in Chapter 3;

+ potential parallelization : each of the N random walkers evolves independently. In addition, as mentioned in the previous paragraph, the generation of the spins' dynamics and the computation of the PGSE signals can also be decoupled.

However, MC techniques in general and current software implementations such as Camino usually suffer from

- high computational effort : the computation time and memory requirements are proportional to the number of spins N , the number of time steps T and the number P of PGSE sequences that are generated. The statistical bias of the generated signals are typically proportional to $1/\sqrt{N}$ when the time step δt allows sufficient accuracy. As we will discuss in Chapter 3, on a non-parallelized software such as Camino, simulation times ranged from 1.5 hrs in the simplest geometries to about 50 hrs in more complex configurations. In the context of the generation of a dictionary of DW-MRI signals, one must keep in mind that each of these simulations has to be carried out hundreds of time to account for different microstructure configurations;

- determination of simulation parameters : as will be discussed in Chapter 3, careful determination of N and T should be carried out for every diffusion environment and every PGSE sequence, through convergence analyses similar to those in [25], involving a lot of simulation time;

- fixed time steps : in its current implementation, Camino does not support variable time steps, i.e. $\delta t_i = \delta t, \forall i$ in the previous paragraph. This implies that δt must be selected so that the step length L_{step} given by (2.2) is adapted to the the spatial scale of the diffusion environment Ω , which can have a negative impact on simulation time when Ω consists of compartments with distinct typical length scales, such as cylinders of different radii, since the smallest compartment will slow down the entire simulation. Artifacts due to δt can also occur during the discrete evaluation (2.3) of the spins's dephasing when the gradient intensity G is high since we would then be integrating a rapidly-varying function with a simple rectangle quadrature rule. Recently-developed algorithms with adaptive time steps such as the *Fast Random Walk* presented in [29] could be a significant improvement in the future;

- implementation overhead : although arbitrary geometries are theoretically possible, only a few of them are currently implemented, mostly based on parallel cylinders to model fascicles of axons, and even so, their current implementation in Camino still exhibits some lack of stability (e.g. simulation failures due to spins crossing barriers they should not, rounding errors, etc.). Camino does offer to run simulations on triangulated

meshes but the computational burden of such simulations becomes almost prohibitive and is certainly not suited for the generation of large numbers of DW-MRI signals such as in this thesis. What's more, the generation of meshes based on real biological tissues is a technically and technologically delicate task (see [30]) and was certainly outside the scope of this thesis.

2.3 The multiple correlation function approach

We present the principles of the multiple correlation function (MCF) approach for the synthetic generation of DW-MRI signals and discuss their advantages and limitations.

2.3.1 Description

Grebenkov's multiple correlation function approach [7, 22] is a unified mathematical framework for solving the macroscopic Bloch-Torrey PDE (1.10) presented in Section 1.3.3 based on the decomposition of the solution into Laplace eigenfunctions. **It yields exact results for a sequence of applied magnetic gradients \mathbf{g} with fixed direction $\hat{\mathbf{g}}$ and piecewise-constant intensity profile.** A detailed mathematical derivation is available in Appendix C.

If we consider a microstructural environment Ω of typical length scale L_0 (for instance, Ω could be an infinitely-long cylinder and L_0 its radius), the DW-MRI signal attenuation $E(\mathbf{p}_{pgse}; \Omega)$ associated to the PGSE parameters $\mathbf{p}_{pgse} = (\mathbf{g} = G\hat{\mathbf{g}}, \Delta, \delta)$ is given by

$$E(\mathbf{p}_{pgse}; \Omega) = \left[\underbrace{e^{-(p\Lambda - iq\mathcal{B})\frac{\delta}{T}}}_{\text{gradient rephasing}} \underbrace{e^{-p\Lambda\frac{(\Delta-\delta)}{T}}}_{\text{pure diffusion}} \underbrace{e^{-(p\Lambda + iq\mathcal{B})\frac{\delta}{T}}}_{\text{gradient dephasing}} \right]_{0,0}, \quad (2.4)$$

where $p = \frac{DT}{L_0^2}$ and $q = \gamma GL_0 T$ are two dimensionless numbers with T being related to the typical time scale of the PGSE experiment, for instance $T = \Delta + \delta$, where the exponentials are matrix exponentials on the diagonal matrix Λ and the symmetric matrix \mathcal{B} , both of infinite dimension and defined in Appendix C and where $[\cdot]_{0,0}$ denotes the first diagonal element. The matrices Λ and \mathcal{B} only depend on the geometry Ω through the resolution of the Laplace eigenvalue problem (C.2) in Ω and, once computed, can be used for any PGSE parameters.

In practice, we will only keep the first M terms of the eigenfunction expansion (C.6), i.e. the first M lines and columns of Λ and \mathcal{B} , with M chosen so that

$$p\lambda_M \gg q, \quad (2.5)$$

where λ_i is the i -th diagonal element of Λ , thus ensuring that the real, damping factor $p\Lambda$ dominates the imaginary, oscillating factor $iq\mathcal{B}$ in Equation (2.4). The strictly monotonous increase of the diagonal elements of Λ ensures that this will always be the case. Note that Equation (2.4) can not be further simplified since the matrices Λ and \mathcal{B} do not commute in general.

2.3.2 Advantages and limitations

The main advantages of the MCF approach can be listed as

+ accuracy : formula (2.4) is exact up to a truncation error that is generally negligible with a truncation parameter $M \approx 50$ for the two geometries we will extensively use in our simulations : disks in \mathbb{R}^2 (for infinite-length cylinders) and spheres in \mathbb{R}^3 (for glial cells);

+ efficiency : the matrices Λ and \mathcal{B} must be computed once and for all thanks to the initial nondimensionalization. These are available on D. Grebenkov's website¹ for the 1D-interval (*slab*), the 2D-disk and the 3D-sphere. Computing Formula (2.4) requires 2 matrix exponentials and one simple real-valued exponentiation, which is a matter of milliseconds on softwares such as MATLAB. In contrast, MC simulations achieving similar levels of accuracy in a cylinder can take up to a few hours, depending on the necessary time step δt .

The drawbacks of the method are identified as

- only valid for a few simple geometries : the Laplace eigenvalue problem (C.2), which allows to compute the matrices Λ and \mathcal{B} , does not have a known analytical solution in general. In particular, the MCF approach is thus **not suited to study the DW-MRI signal of the more complicated extra-axonal space**, i.e. related to water molecules evolving between parallel axons in a fascicle, outside these axons (see Figure 1.6 (b));

- not suited for parametric models : Formula (2.4) depends on the microstructure and PGSE parameters in a complicated fashion through p, q and matrix exponentials and therefore does not easily lend itself to traditional parameter estimation such as described in Section 1.4.1. This might be one of the reasons why the MCF approach is

¹http://pmc.polytechnique.fr/pagesperso/dg/MCF/MCF_e.htm

still relatively little used in microstructure imaging, but this is not a limitation in our dictionary-based framework.

2.4 A hybrid approach for DW-MRI signal synthesis

Assuming that the diffusion environment Ω is made of two compartments Ω_1, Ω_2 of respective volume fractions f_1 and f_2 , that the MCF approach is applicable in Ω_1 and that there is little to no exchange between the two compartments, we can apply the superposition principle presented in Section 1.3.4 and obtain our total hybrid signal E_{hyb} as

$$E_{hyb}(\mathbf{p}_{pgse}; \Omega) = f_1 E_{MCF}(\mathbf{p}_{pgse}; \Omega_1) + f_2 E_{MC}(\mathbf{p}_{pgse}; \Omega_2), \quad (2.6)$$

for given PGSE parameters \mathbf{p}_{pgse} , using a traditional MC simulation in Ω_2 . In all our subsequent experiments, Ω_1 will be the inside of cylinders, the intra-axonal space, and Ω_2 will be the geometrically more complicated extra-axonal space.

We first proceed to validate our approach by comparing its results with complete MC simulations, which are still considered to provide ultimate ground truth in DWI as long as the simulation parameters N and T are appropriately selected, as discussed in Section 2.2.

We then discuss the gain in precision-efficiency trade-off of our hybrid method compared to complete, all-out MC simulations.

2.4.1 Validation

We validate the hybrid approach on the three most important elementary microstructural configurations that will be part of our dictionary :

- an infinite array of infinitely-long, parallel, hexagonally-packed cylinders of given radius and separation, serving as a good model of single fascicles of axons (see Figure 3.1 on page 43);
- two crossing arrays of infinitely-long, parallel, regularly-packed cylinders, where the crossing occurs in interleaved planes, as depicted in Figure 3.4 on page 48. This is used as a representation of two crossing fascicles of axons;
- 100 infinitely-long, parallel cylinders of varying radii packed in a square region of given size which is then periodically repeated to infinity, as illustrated in Figure 3.5 on page 48. The radii are drawn from a Gamma distribution, which is known to be biologically realistic [15, 16].

We report for each validation the number of spins N and time steps T for the complete MC simulations as well as for the "partial" MC simulations (i.e. simulating only extra-axonal spins) used in the hybrid method.

2.4.1.1 Single array of identical cylinders

All cylinders have radius $r = 3 \mu\text{m}$ and the spacing between cylinders is $s = 6.1 \mu\text{m}$, which in the case of hexagonal packing leads to an intra-axonal volume fraction of $f_{in} = \frac{2\pi}{\sqrt{3}} \left(\frac{r}{s}\right)^2 = 0.877$. We test 4 different combinations of PGSE parameters (G, Δ, δ) corresponding to 4 b-values ranging from 496 to 2635 s mm^{-2} and use 90 gradient directions $\hat{\mathbf{g}}$ per b-value.

Parameters of the complete MC simulation The reference MC simulation uses $N = 1 \times 10^5$ spins, as suggested in [25] for a similar type of cylinder array. The smoothness of the dashed curves in Figure 2.2 suggests that this number was sufficient to limit the statistical variability associated with MC simulations. We take a number of time steps $T = 1000$, yielding a step length $L = \sqrt{4D\frac{TE}{T}} = 0.65 \mu\text{m}$ (using the commonly-used value for water diffusivity $D = 2.0 \times 10^{-9} \text{ m s}^{-1}$), which is relatively small compared to the typical length scale of the diffusion environment, of the order of $r = 3 \mu\text{m}$ here.

Parameters of the hybrid approach The simulation for the extra-axonal signal uses the same number of time steps T and a number of spins $N = 20000$, which is proportionally **more** than in the total simulation given the intra-axonal volume fraction f_{in} . The truncation parameter M is set to 60 for the computation of the intra-axonal signal with the MCF method. The hybrid signal is thus obtained as the sum of the extra-axonal MC simulation and the MCF signal, weighted by $(1 - f_{in})$ and f_{in} respectively.

Comparison The results obtained in both cases are almost identical, as can be observed in Figure 2.2, confirming the reliability of the hybrid method. We plotted the signals as a function of the dot product between the cylinders' unit direction \mathbf{n} and each gradient unit direction \mathbf{g}/G and also indicated the signal corresponding to free, unrestricted diffusion $E_{free} = \exp(-bD)$ from Equation (1.13). When the gradients are parallel to the cylinders, corresponding to a unit dot product on the graph, the obtained signals correspond to free diffusion since the diffusion along the axis of the infinitely-long cylinder is unrestricted. Magnetic gradients applied perpendicular to the cylinders' axis yield the highest diffusion signal, since they correspond to the direction in which spin motion is most restricted.

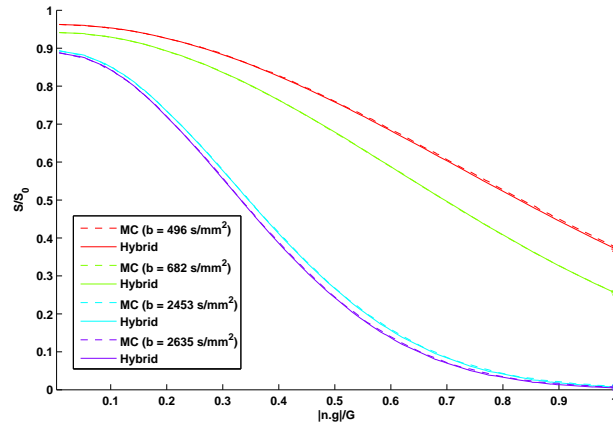


FIGURE 2.2: **Hybrid method yields groundtruth results for identical cylinders.** Total signal of an array of parallel cylinders obtained by complete MC simulations, considered exact, and by our hybrid combination of MC and MCF methods. The asterisks correspond to the free-diffusion signals. We tested 90 gradient directions for each of the 4 b -values. The two curves for each b -value are barely distinguishable.

2.4.1.2 Crossing arrays of identical cylinders

We consider two arrays of hexagonally-packed cylinders crossing in the xz -plane at an angle $\theta = \frac{\pi}{4}$, as illustrated in Figure 3.4 on page 48. All cylinders have radius $r = 1 \mu\text{m}$ and are separated by a distance $s = 2.1 \mu\text{m}$, leading to an intra-axonal volume fraction of $f_{in} = \pi \left(\frac{r}{s}\right)^2 \approx 0.71$. We test the same 4 b -values as in the validation of the single array of cylinders, with 90 gradient directions per b -value. The dot-product of each gradient direction with the direction of either fascicle or their bisector no longer leads to a smooth representation of the signal. We therefore choose to use a 2D-parametrization of the gradient direction in terms of the elevation angle α and the angle β from the fascicles' bisector, as shown in Figure 3.4 (page 48).

Parameters of the complete MC simulation We use $N = 1.1 \times 10^5$ and a slightly higher $T = 1200$ to account for smaller spatial dimensions and reduce the step length. These parameter values seem to lead to relatively smooth and sensible results, as can be observed in Figure 2.3.

Parameters of the hybrid approach The simulation for the extra-axonal signal uses the same number T and a number of spins $N = 35\,000$ in phase with the extra-axonal volume fraction $(1 - f_{in})$ of the diffusion environment. The truncation parameter M is set to 60 for the MCF intra-axonal signal of both cylinders.

Comparison As can be observed in Figure 2.3, the surfaces obtained in the case of full MC simulations can barely be differentiated from the surfaces resulting from the hybrid method, except for gradient directions whose projections in the fascicles' plane

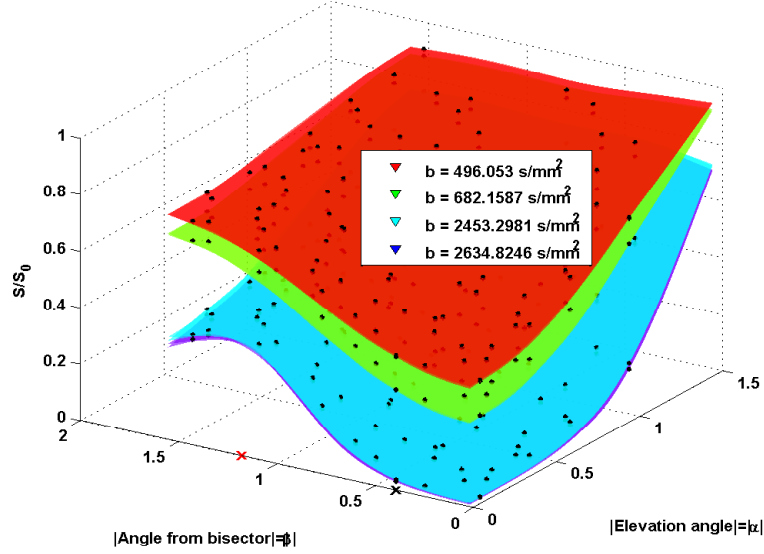


FIGURE 2.3: **Hybrid method yields groundtruth results for crossing cylinders.** Signal of fascicles crossing at an angle $\theta = \pi/4 \approx 0.785$ rad, obtained by complete MC simulations, considered exact, and our hybrid approach. The MC and hybrid surfaces are almost indistinguishable, except near $\beta \approx 1.5$ rad. The black marker at $(\alpha, \beta) = (0, \frac{\theta}{2})$ corresponds to the presence of fascicles either side of the bisector while the red marker at $(\alpha, \beta) = (0, \frac{\pi}{2} - \frac{\theta}{2})$ indicates the direction perpendicular to either fascicle in the fibers' plane ($\alpha = 0$), where a signal maximum seems to occur.

are perpendicular to the fascicles' bisector, i.e. $\beta \approx \frac{\pi}{2}$, at the 2 highest b -values. Note that all 8 surfaces are obtained by smooth approximation of the 90 data points available per b -value, indicated by black markers. As expected, the absolute maximum occurs in the direction normal to the fascicles' plane, i.e. $\alpha = \frac{\pi}{2}$, when the diffusion as "seen by the gradient" is most restricted. In the fascicles' plane ($\alpha = 0$), signal maxima seem to occur when the applied magnetic gradient is perpendicular to either one of the fibers, as indicated by the red cross on the graph.

2.4.1.3 Array of Gamma-distributed cylinders

In this validation experiment, 100 parallel cylinders with radii drawn from a Gamma distribution of shape parameter $a = 16.275$ and scale parameter $b = 2.86 \times 10^{-6}$, thus having mean $\mu_r = ab = 0.465 \mu\text{m}$ and standard deviation $\sigma_r = \sqrt{ab} = 0.115 \mu\text{m}$, are packed into a square region of side length $l = 10.45 \mu\text{m}$ through a trial-and-error algorithm implemented in Camino. The obtained radii lead to an intra-axonal volume fraction of $f_{in} = 0.65$ and range from $r_{min} = 0.243 \mu\text{m}$ to $r_{max} = 1.025 \mu\text{m}$. We test 90 gradient directions for 3 rather high b -values.

Parameters of the complete MC simulation The reference MC simulation is run with $N = 1.6 \times 10^5$ spins and $T = 5000$ time steps, as it was proven sufficient in [17]. This leads to a step length of $L_{step} = 0.293 \mu\text{m}$, which seems too large for the smaller

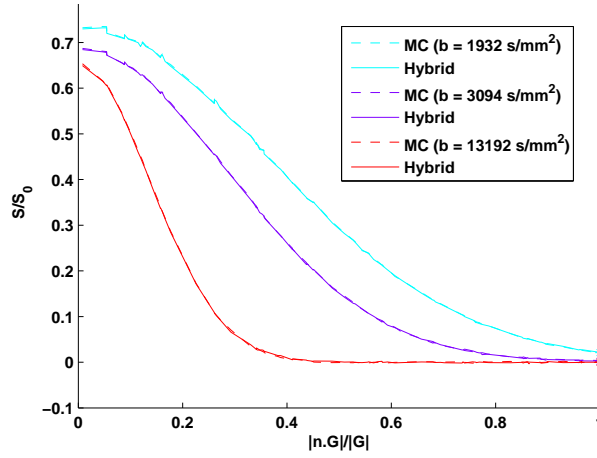


FIGURE 2.4: **Hybrid method yields groundtruth results for Gamma-distributed cylinders.** Signal of so-called Gamma-distributed cylinders obtained by complete MC simulations (dashed curves, considered exact) and our hybrid approach (solid curves) for 3 fixed b -values and 90 gradient directions per b -value. The asterisks correspond to the free-diffusion signals. The two methods are again almost perfectly identical.

cylinders. We can indeed observe a **few discontinuous jumps** in Figure 2.4, especially at high b -values and gradient directions perpendicular to the cylinders.

Parameters of the hybrid approach The MC simulation for the extra axonal space uses $N = 62000 \approx f_{in} \cdot 1.6 \times 10^5$ random walkers and the same number of time steps $T = 5000$. The MCF method is run 100 times for each cylinder radius and each signal is weighted by the relative volume fraction of its cylinder.

Comparison Figure 2.4 shows again nearly perfect resemblance between the two methods. Although the **b -values are high**, which generally makes the **evaluation of the dephasing through Equation (2.3) less accurate**, the obtained signals remain rather smooth.

2.4.2 Precision-efficiency gain

We proceed to a simple variance analysis of the signal obtained by complete MC simulations and the hybrid signal presented above. If we note $W_k = e^{i\phi_k}$ the random variable representing the (non-normalized) signal contribution of spin k , where ϕ_k is the accumulated phase shift, then the hybrid signal S_H is the random variable

$$S_H = f_{in}S_{in} + f_{ex}\frac{1}{N_H}\sum_{k=1}^N W_k,$$

where N_H is the number of spins used to simulate the extra-axonal signal and where S_{in} is the value obtained with the MCF method assumed applicable for the intra-axonal signal and considered deterministic and exact. The spins' trajectories (and any function

thereof) are independent by definition, and we further assume that an initial uniform distribution of spins across the domain ensures that they are identically distributed, which allows to compute the variance σ_H^2 of S_H as a function of the variance σ_W^2 of all the random variables W_i

$$\sigma_H^2 = \frac{f_{ex}^2 \sigma_W^2}{N_H}.$$

Defining the precision p as the inverse of the standard deviation, we obtain the precision p_H associated with the hybrid signal

$$p_H = \frac{\sqrt{N_H}}{f_{ex} \sigma_W}, \quad (2.7)$$

while the precision p_M of a complete MC simulation performed with a total of N_C spins can be written as

$$p_M = \frac{\sqrt{N_M}}{\sigma_W}, \quad (2.8)$$

assuming intra-axonal and extra-axonal spin phases are identically distributed. We can now analyze the gain in precision-efficiency trade-off through three different situations, illustrated in Figure 2.5

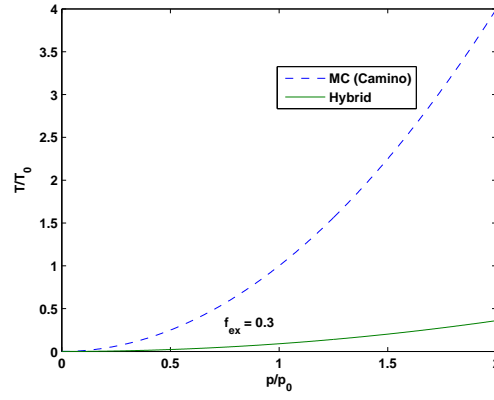
- **Fixed diffusion environment** For a given intra-axonal volume fraction f_{in} where the MCF method is applicable, we predict the **simulation time T** of the two methods as a function of the desired precision p as

$$\begin{aligned} T_H &= T_0 N_H = T_0 \sigma_W^2 f_{ex}^2 p^2 \\ T_M &= T_0 N_M = T_0 \sigma_W^2 p^2, \end{aligned} \quad (2.9)$$

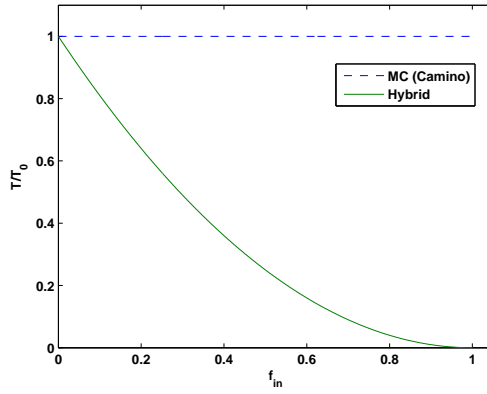
where the common factor T_0 accounts for the number of time steps and of PGSE sequences. There is therefore a gain factor f_{ex}^2 for the hybrid method, which is non-negligible for typical values $f_{ex} \approx 0.3$, leading to a reduction of **81%** in computation time for the same precision, as shown in Figure 2.5a.

- **Fixed precision** Figure 2.5b illustrates Equations (2.9) as a function of the intra-axonal volume fraction f_{in} , for a given precision. We see the **advantage of using the hybrid method, especially for typical microstructural values $f_{in} \geq 0.5$** .
- **Fixed simulation time** If we set $N_H = N_M = N$, then the precision p_M of a MC simulation will remain constant irrespective of the intra-axonal volume fraction f_{in} , i.e. $p_M = \frac{\sqrt{N}}{\sigma_W}$, while the precision p_H of the hybrid method evolves as

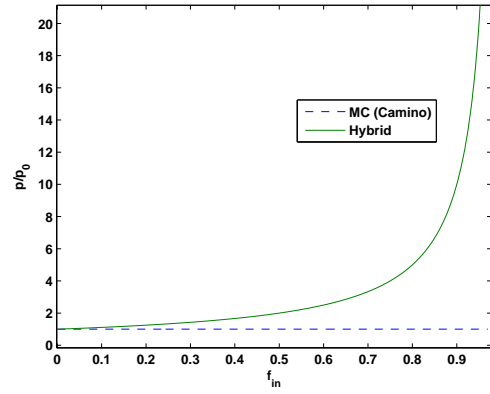
$$p_H = \frac{\sqrt{N}}{\sigma_W (1 - f_{in})}, \quad (2.10)$$



(A) Simulation time vs precision



(B) Simulation time vs intra-axonal volume fraction



(C) Precision vs intra-axonal volume fraction

FIGURE 2.5: **Hybrid method leads to gain in precision-efficiency trade-off for commonly-used microstructural configurations.** The reference values T_0 and p_0 include factors common to both methods, such as the number of PGSE sequences or the number of time steps used. These results hold when part of the signal arises from geometric compartments where the MCF method is applicable.

tending to the (nearly) infinite precision of the MCF approach when there is no extra-axonal space, as presented in Figure 2.5c.

Chapter 3

Creation of a dictionary of DW-MRI signals

This chapter details the construction of our dictionary of DW-MRI signals made of elements or atoms $E(\{\mathbf{p}_i\}_{1 \leq i \leq P}; \Omega)$ related to a given diffusion environment Ω , considered as vectors in \mathbb{R}^P , where P is the number of acquisition parameters. We try to generate as complete and finely sampled a dictionary as possible with respect to both the "microstructure parameter space" and the "acquisition parameter space" while maintaining tractable simulation times for such a Master's thesis¹. We present biological and physical justification for the selection of both the acquisition sequences and the microstructure parameters and set up a careful simulation procedure to ensure the quality of our generated signals.

The main results of this chapter may be summarized as follows.

§ 3.1 *We select $P = 6095$ combinations of PGSE acquisition parameters from the associated 5-dimensional parameter space for each atom of our dictionary, ensuring clinical feasibility, for instance through the use of traditional acquisition protocols taken from the literature, while making room for less conventional parameter values. All the selected sequences are summarized in Table F.1.*

§ 3.2 *We settle for 4 types of elementary atoms, of great interest in microstructure imaging*

– *single fascicles of identical axons (180 atoms);*

¹We acknowledge and are grateful that computational resources have been provided by the supercomputing facilities of the Université catholique de Louvain (CISM/UCL) and the Consortium des Équipements de Calcul Intensif en Fédération Wallonie Bruxelles (CÉCI) funded by the Fond de la Recherche Scientifique de Belgique (F.R.S.-FNRS) under convention 2.5020.11.

- crossing fascicles of identical axons (216 atoms);
- single fascicles with radius heterogeneity (44 atoms);
- glial cells modeled as simple spheres (150 atoms).

Heuristics are designed to select simulations parameters that ensure the quality, consistency and accuracy of all the signals generated with our previously-validated hybrid method. Considerable simulation times are required and reported in Table F.2.

3.1 Selection of acquisition sequences

Recall that we are dealing with the Pulsed Gradient Spin-Echo (PGSE) experiment presented in Section 1.3.1, characterized by sequences such as illustrated in Figure 1.4 on page 11, where the three main tunable parameters are the magnetic gradient vector $\mathbf{g} \in \mathbb{R}^3$, the duration of the gradient pulses δ and the diffusion time Δ between the onsets of the pulses, summing up to 5 degrees of freedom. Besides the classical scalar quantity known as b-value defined by Equation 1.14, we will make use of the b-vector notation

$$\mathbf{b} := (\gamma\delta G)^2 \frac{\mathbf{g}}{G} (\Delta - \delta/3) = b\hat{\mathbf{g}}. \quad (3.1)$$

A set of PGSE parameter combinations $\{\mathbf{g}_i, \Delta_i, \delta_i\}_{1 \leq i \leq P}$ is referred to as an *acquisition scheme* or *acquisition protocol*. These parameters can be thought of as machine settings and affect the measured signal $E(\mathbf{p}_{pgse}; \Omega)$ as much as the geometry Ω in which water molecules are diffusing. In practice the number of acquisitions is limited and the parameter values are carefully chosen. However, since our ultimate goal is to generate a large dictionary and to compare for instance which acquisition parameters lead to a better characterization of our brain, we will investigate as large a number of PGSE sequences as possible.

After careful investigation of the available scientific literature, we have selected

- an ActiveAx-like scheme [17] ;
- a NODDI-like scheme [18] ;
- a DSI-like scheme [27] ;
- CUSP-like schemes based on the projection onto a cube of the ActiveAx and NODDI schemes [13];
- 50 more HARDI-type schemes [12],

for a total of $P = 6095$ sets of acquisition parameters, i.e. 6095 combinations of $(\mathbf{g}, \Delta, \delta)$. The next paragraph below introduces the popular HARDI protocols as they

form the basis of nearly all the selected acquisition schemes. Then a section will be devoted to briefly presenting the gist of the ActiveAx, NODDI, DSI and CUSP-like schemes, more thoroughly described in Appendix D. We will then take more time to explain according to which criteria we determined 50 supplementary HARDI-type acquisition schemes. Table F.1 in Appendix F summarizes all the selected acquisition sequences.

Basics of HARDI schemes A High Angular Resolution Diffusion Imaging (HARDI) scheme basically consists in probing diffusion in tissues with a fixed b-value from many different angles [12]. The idea behind HARDI is that the acquisition and the subsequent parameter estimation of the model should be orientationally invariant. Mathematically, the values of Δ , δ and the gradient strength G are fixed while the gradient directions are uniformly distributed across the three-dimensional unit sphere S^2 . The 3-D representation of the gradient vectors or of the b-vectors (since these differ only by a constant) then resembles a spherical shell.

In multi-shell HARDI, the values of Δ and δ are fixed and M shells of different b-values are created by varying the gradient intensity G , each shell containing N gradient directions. Maintaining Δ and δ constant throughout all DW-MRI acquisition shells has the advantage of leading to the same Eddy currents distortion patterns and making subsequent image alignment easier.

3.1.1 Traditional acquisition schemes selected for the dictionary

All 4 acquisition protocols, ActiveAx, NODDI, CUSP and DSI are explained in more details in Appendix D and their specific values are summarized in Table F.1 in Appendix F.

Both the ActiveAx and the NODDI protocols are 4-shell HARDI schemes with gradients and b-vectors (differing only by a constant) distributed over spherical shells. The shell parameters (G, Δ, δ) and the number of gradient directions per shell N are determined by attempting to minimize the variance of the parameters of a simple microstructural model such as those presented in Section 1.4.1 fitted on DW-MRI acquisitions.

CUSP-like schemes basically consist in projecting the gradient directions of a HARDI scheme from a sphere onto an enclosing cube, allowing to get higher values of gradient intensity G while maintaining Δ and δ and thus the echo time TE constant, thereby limiting T2 signal losses (see Section 1.1.1) and maximizing the SNR.

DSI schemes are slightly different in that the so-called q-vector, differing from the b-vector by a constant, does not take values on a sphere or a cube but rather on a lattice. Such a scheme generally requires more acquisitions and its intended use is related to the Fourier relationships associated with the SGP approximation, briefly introduced in Section 2.1 and presented in Appendix B.

3.1.2 Supplementary HARDI shells

We want to probe diffusion through as complete a sampling of the PGSE parameter space as possible and therefore investigate more combinations of \mathbf{g} , Δ and δ . In order to preserve rotational invariance, we adopt the HARDI-shell formalism with M shells containing N uniformly distributed gradient directions. The triplets $(G_i, \Delta_i, \delta_i)_{1 \leq i \leq M}$ are generated so as to fill in the gaps left by the previously proposed samplings of the parameter space (ActiveAx, NODDI, CUSPed ActiveAx, CUSPed NODDI, DSI). They are also subject to the following considerations

- the total number of sequences MN should not exceed 5000 to keep the generation of our dictionary of DW-MRI signals computationally tractable ;
- the number N of gradient directions determines the angular resolution θ of the scheme

$$\theta = \sqrt{\frac{4\pi}{N}} \quad (3.2)$$

in steradians [27] and provides an indication of how finely crossing bundles of axons in the white matter could be separated. Setting $N = 90$ yields an angular resolution of 21.4° while allowing us to try up to $M = 55$ different combinations of G , Δ and δ ;

- the gradient strength G is limited by the capabilities of present-day MRI scanners. Human systems can typically reach G_{max} between 40 and 80 mT m⁻¹ while small-bore animal systems can generally reach 200 mT m⁻¹ [17]. More powerful animal systems can even provide gradient magnitudes as high as 1 T m⁻¹, as reported recently in [31]. Since the previously described sampling schemes chiefly cover the range [0, 60] mT m⁻¹, we choose to try the higher values $G = [40, 60, 70, 80, 120, 140]$ mT m⁻¹. Note that we keep the more standard value $G = 40$ mT m⁻¹ to later combine it with other values of Δ and δ ;
- from the definition of the PGSE experiment, we must have $\Delta \geq \delta$ (see figure 1.4), neglecting the time required for the RF pulses coming after the first gradient block;

- the echo time (TE) clearly admits the lower bound $TE \geq \Delta + \delta$, neglecting the time required for the RF pulses and signal read out. It is a quantity of importance because it is closely related to the SNR of the DW-MRI measurements. The attenuation of the measured DW-MRI signal due to spin-spin relaxation presented in Section 1.1.1 is given by

$$E_{relax} = \exp\left(-\frac{TE}{T_2}\right), \quad (3.3)$$

where T_2 is the spin-spin relaxation time, typically of the order of 70 ms in human white matter [32]. Longer TE's make the useful signal impossible to distinguish from the noise floor. We allow a relatively high limit of 180 ms on TE, imposing

$$\Delta + \delta \leq 180 \text{ ms}; \quad (3.4)$$

- the parameter Δ is of utmost importance since it corresponds to the time water molecules are given to diffuse around the tissue structures and should therefore be matched with the typical length scale of the microstructure configuration under investigation. The formula relating the unidirectional rms displacement r of a particle undergoing Brownian diffusion during a time span Δ

$$r = \sqrt{2D\Delta}, \quad (3.5)$$

where the diffusivity of the medium D provides a reference for interesting values of Δ . For instance, taking $D \approx 2.1 \cdot 10^{-9} \text{ m}^2 \text{ s}^{-1}$, an axon of radius $10 \mu\text{m}$ requires in theory a diffusion time Δ of at least ≈ 23.8 ms. Since diffusion times as low as 1.9 ms ([31], although with an OGSE instead of a PGSE sequence) and as high as 87 ms ([17]) have been proposed in DW-MRI experiments, we choose to test $\Delta = [2, 5, 10, 15, 20, 38, 66, 80, 100] \text{ ms}$;

- a direct interpretation of the parameter δ is more difficult to establish. It is clear that the b-value increases with δ when $\Delta \geq \delta$ (see equation (1.14)). Values ranging from 2.5 ms [33] to 60 ms [27] have been reported in DW-MRI experiments. We consequently decide to test the values $\delta = [2, 15, 30, 70] \text{ ms}$;
- we finally set a lower and upper bound on the b-value associated to each triplet (G, Δ, δ) . Intuitively, the signal associated with free, Gaussian diffusion $E_{free} = \exp(-bD)$ presented in Section 1.3.3 provides an indication of the order of magnitude we can expect from an acquisition at the b-value b . High b-values will then yield signals of low intensity comparable to the acquisition noise and very low b-values will induce no signal attenuation, as if the molecules were stationary. In the study conducted in [34], it is suggested that DW-MRI signals acquired at

up to $b = 18000 \text{ s mm}^{-2}$ can still be considered to carry relevant information. The b-values used in ActiveAx and NODDI stay below 3000 s mm^{-2} and the b-values in the DSI scheme reach 17000 s mm^{-2} . To limit the number of admissible sequences, we therefore set

$$200 \leq b \leq 20000, \quad (3.6)$$

expressed in $[\text{s mm}^{-2}]$.

Combining all the candidate values for G, Δ and δ while enforcing all the aforementioned constraints leads to $M = 50$ admissible triplets $(G_i, \Delta_i, \delta_i)$ and a total of **4500** acquisition sequences, with G taking values in $[40, 140] \text{ mT m}^{-1}$, Δ in $[15, 100] \text{ ms}$, δ in $[2, 30] \text{ ms}$ and b in $[2095, 19253] \text{ s mm}^{-2}$. Most parameter values lie on the verge of clinically realistic parameter ranges but none of them seems utterly aberrant.

Care should probably be taken with strong gradients of short duration as real-life MRI-scanners might not be able to deliver rectangle-shaped gradient blocks such as depicted in figure 1.4 (page 11), but might instead create a trapezoidal waveform because of a limited slew rate. Here the ratio G/δ ranges from 1.33 to 70 with a 13.12 average over the 50 shells (all expressed in $[\text{mT m}^{-1} \text{ s}^{-1}]$), which seems quite high given that the highest G/δ ratio found in the previously described DW-MRI protocols is $57/5 = 11.4$ in the ActiveAx scheme.

3.2 Selection of microstructure configurations

Now that we have sampled the "acquisition parameter space", we turn our attention to the sampling of the "microstructure parameter space". We will consider 4 types of elementary microstructure configurations or *atoms* in our dictionary

- **single fascicles of identical axons** modeled by infinitely long, parallel cylinders of constant radius;
- **two crossing fascicles of identical axons** modeled by two crossing fascicles such as described above;
- **single fascicles of axons with Gamma-distributed radii** modeled by infinitely long parallel cylinders with radii drawn from a Gamma distribution;
- **glial cells** modeled by simple spheres.

For each type of atom successively, we briefly justify why it is biologically relevant, identify the main parameters characterizing the diffusion environment and select a discrete set of representative parameter values so as to cover as large and finely sampled a range

as possible while maintaining the size of the dictionary and the associated simulation time tractable for a Master's thesis. We synthesize the signals using the hybrid method validated in Section 2.4, combining an exact analytic results for the intra-axonal signal with MC simulations for the extra-axonal signal. We explain how appropriate MC simulation parameters were determined (N and T) and validate the synthesized signals through graphical inspection using suitable 1D- or 2D-representations of the generated data.

The choice of these 4 elementary atom types was driven by the current capabilities of validated MC softwares such as Camino and by the ultimate use we would like to make of our dictionary, namely microstructure parameter estimation based on sparse linear reconstruction. Such a method would be deemed very satisfactory if it were already able to use these 4 types in order to reliably recover the number and principal orientations of fascicles within a voxel and the volume fraction related to "non-cylindrical" structures such as glial cells. In the future, it will certainly be of interest to add more refined microstructure atoms to the dictionary such as myelinated or undulating axons to further improve the characterization of our brain.

We report typical simulation times all along the section. Monte Carlo simulations, used for the extra-axonal signal, were carried out with the Camino software presented in Section 2.2 [24] and executed on the CISM computing clusters while less intensive tasks related for instance to the MCF method and intra-axonal signal (Section 2.3) were run on a standard laptop equipped with a 2.27 GHz Intel dual core processor. All the parameter values and simulation times are compiled in Table F.2 in Appendix F.

Finally, we assume throughout that all axons' membranes are impermeable at the timescale of our DW-MRI acquisitions and therefore apply the superposition principle (Section 1.3.4) necessary for our hybrid signal generation method (Section 2.4).

3.2.1 Single fascicles of identical axons

Fascicles of axons are the main constituents of the brain white and grey matter. At the scale of voxel, i.e. a cube of about 1 to 2 mm of side length, it is reasonable to focus on straight, non-bending fascicles, and since the radius of the axons making up the fascicles is of the order of the micrometer, they are by far longer than they are thick and it is thus common to model them as infinitely-long cylinders. We assume that all axons have identical radii for simplicity in this section and study radius heterogeneity in Section 3.2.3. We consider hexagonal packing of the cylinders because it is the tightest packing of circles in \mathbb{R}^2 and will therefore allow for large intra-axonal volume fractions (Figure 3.1).

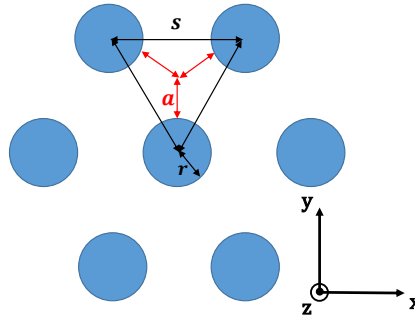


FIGURE 3.1: **Single fascicles modeled as hexagonally-packed axons.** Hexagonal packing of cylinders of radius r with cylinder separation s . We consider that the distance from the center of a gap in the extra-axonal space to the nearest axons, a , is the typical length scale of the diffusion environment.

Selection of microstructure parameters

The main parameter of this type of dictionary atom is the axon radius r . Radius values depend on the precise location within the human nervous system and are still not perfectly identified, but they can usually be considered to lie in the range $[0.5 - 10] \mu\text{m}$ [15, 16, 35]. We choose to sample the radius space up to $20 \mu\text{m}$ for different reasons: in case it might be relevant for humans, to account for the additional thickness of the myelin sheath we did not explicitly model (see Figure 1.6 for instance), and finally because it is not uncommon to encounter larger radius values when performing validation on animals, as described in [36].

The second parameter is the cylinder separation s , which must naturally be such that $s \geq 2r$. It is however more convenient to characterize a fascicle by its intra-axonal volume fraction f_{in} , related to r and s through the formula ²

$$f_{in} = \frac{2\pi}{\sqrt{3}} \left(\frac{r}{s}\right)^2. \quad (3.7)$$

The value of f_{in} is typically 0.71 in human white matter tissues [25] and is mathematically limited by $f_{in} \leq \frac{\pi}{2\sqrt{3}} \approx 0.9069$. We therefore choose to sample 6 values from 0.4 to 0.9, staying just below the upper limit so that cylinders do not abut, thereby avoiding potential instabilities during MC simulations of the extra-axonal signal. All the selected parameter values are summarized in Table F.2 in Appendix F.

²Formula (3.7) is readily checked by considering the black equilateral triangle in Figure 3.1 as the elementary, infinitely-repeating pattern in a hexagonal packing of circles.

Determination of Monte Carlo simulation parameters

The MC simulations to obtain the extra-axonal signal of each atom must be executed with carefully-selected simulation parameters N and T in order to achieve sufficient accuracy and precision while keeping tractable computation times. The difficulty resides in the fact that there is here no known groundtruth against which the accuracy of MC results can be assessed. In [25, 30], it was suggested to look for an optimal ratio N/T and keep that ratio constant subsequently, after a bias analysis based on pseudo groundtruth from a simplified analytic model similar to those presented in Section 1.4.1. We conjecture however that this ratio is of lesser importance than the number of time steps T since the statistical variance always decreases with the number of spins N . The parameter T should be chosen in accordance with the total duration of each simulation (related to TE) and so that the fixed step length L_{step} of the spins at each iteration (Equation (2.2)) is adapted to the spatial scale of the diffusion environment.

We therefore proceed to a similar mean and variance analysis of the generated signals for different number of spins N and time steps T , keeping $N, T \geq 10^2$, for a "representative" atom of microstructure parameters $r = 3 \mu\text{m}$ and $s = 6.1 \mu\text{m}$, leading to $f_{in} = 0.877$, using the 360 parameter sets of the ActiveAx protocol described in Appendix D. The largest standard deviations of the generated DW-MRI signals among all 360 sequences over 10 repetitions are shown in Figure 3.2 and present the steady $\frac{1}{\sqrt{N}}$ decrease typical of MC simulations, confirming our first intuition. The analysis of the mean of the signal in Figure 3.3 shows a departure from a stable plateau when the number of time steps T gets below a certain threshold value. Further inspection reveals that this critical value occurs when the step length L_{step} of the diffusing spins is approximately equal to the distance a presented in Figure 3.1, computed as $a = \frac{s}{\sqrt{3}} - r$, which we will call the typical length scale of single fascicles of identical axons. We thus decide to compute the number of time steps T as a function of a for all such single-fascicle atoms, setting

$$T = \max \left\{ 1000, \frac{4D TE}{a^2} \right\}, \quad (3.8)$$

for a given echo time TE and making sure T does not get too small for diffusion environments of larger typical length scale. We select the number N_{ex} of extra-axonal spins for the simulation such that

$$f_{ex} N_0 \leq N_{ex} \leq N_0, \quad (3.9)$$

where $N_0 = 10^5$ is the number of spins used for the *entire* diffusion environment in [25].

We conclude this paragraph by stressing that conducting such a signal-mean analysis for all 180 microstructural configuration of this type instead of using the heuristic (3.8) does not seem realistic. The simulation times for this particular dictionary atom ranged

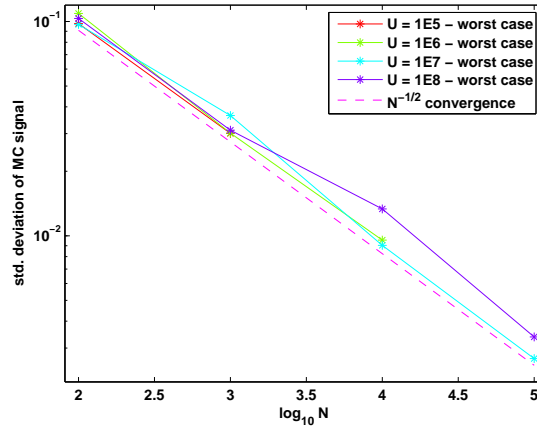
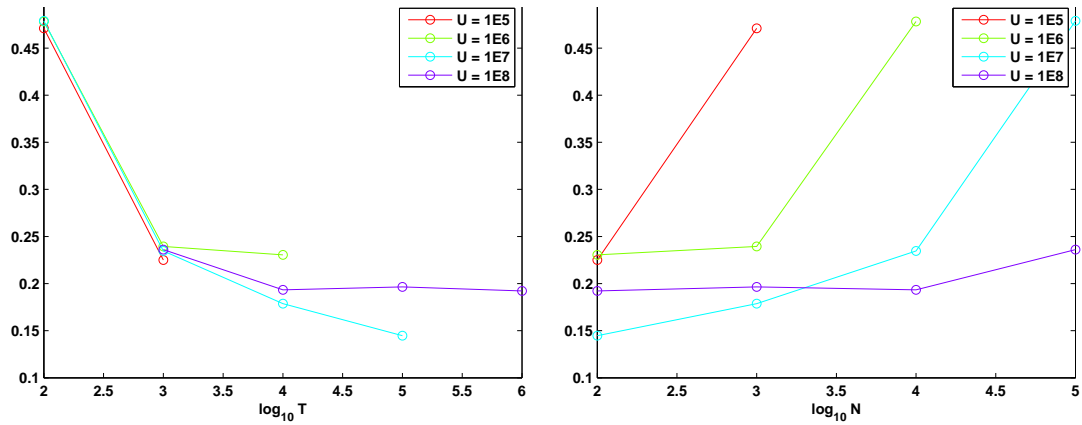


FIGURE 3.2: **Increasing the number of spins yields a steady increase in MC results precision.** Standard deviation (worst case over the 360 tested sequences) of MC extra-axonal signal over 10 repetitions for each pair (N, T) , with $N, T \geq 10^2$. We observe a steady decrease proportional to $N^{-1/2}$, as is to be expected with MC simulations although the value of T varies along each curve.



(A) A bias seems to occur for values of $\log_{10}(T) \in [3, 4]$. (B) A bias seems to occur at (N, T) pairs corresponding to $\log_{10}(T) \in [3, 4]$.

FIGURE 3.3: **Accurate MC results are only achievable above a critical number of time steps.** Mean of MC extra-axonal signal over 10 repetitions for different complexity values U , with $N, T \geq 10^2$. The simulated signal seems to be biased for values of T lower than a critical value located between 10^3 and 10^4 and then seems to stabilize.

from 5 s for $U = 10^5$ to about 1 h15 min for $U = 10^8$ which, multiplied by the number of repetitions, amounted to over 55 h of simulations, and the complexity U is likely to increase drastically through T for atoms of smaller typical length scales a , as suggested by Equation (3.8). The computational burden associated with just generating the actual atoms already amounted to over 3600 h by itself, as indicated in Table F.2, Appendix F.

Validation of generated signals

Figures E.1, E.2, E.3 available in Appendix E.1 show signals obtained at HARDI shells of different b-values plotted as a function of the angle between the magnetic gradients and the axons' direction, in the case of respectively small, moderately large and very large radius values of 0.5, 7.5 and 18 μm . All signals associated with small radii exhibit very good quality. From $r \geq 7 \mu\text{m}$, a few irregularities start to appear at lower intra-axonal volume fractions (since they suffer more from MC simulation bias in our hybrid method), at higher (and somewhat less realistic) b-values, and for gradient directions perpendicular to the axons, probably due to numerical errors during the discretized evaluation of the spins' dephasing through Equation (2.3) under intense magnetic gradients. All these atoms correspond to extra-axonal signals simulated with $T = T_{min} = 1000$ and suggest that our heuristic (3.8) might overestimate the tolerable step length L_{step} when spins have more space to diffuse. However, most of our 6095 acquisition sequences presented in Section 3.1 correspond to high-quality signals and smoothing interpolators could easily be applied if necessary.

3.2.2 Crossing fascicles of identical axons

Crossing fascicles of axons are of tremendous importance in microstructure imaging since voxels of typical clinical size containing more than 1 fascicle could account for 60 to 90% of all brain voxels. Integrating crossing-fascicle atoms into our dictionary allows us to

- verify if the superposition principle holds, i.e. if two crossing fascicles (sharing the *same* extra-axonal space) can be accurately modeled by the sum of two single fascicles with distinct orientations and generated with *independent* extra-axonal spaces;
- potentially facilitate the estimation of the parameters associated to 3 or more fascicles of axons, as the sum of one crossing-fascicle atom and of one single-fascicle atom for instance, when it comes to using our dictionary in the context of sparse estimation of microstructure parameters.

Crossing-cylinder atoms are created by first generating the intra-axonal signals associated with two cylinders of distinct orientations by the MCF approach, and then running a MC simulation with random walkers uniformly distributed across the common extra-axonal space, shared by both fascicles. We only consider two identical fascicles because of the current capabilities of our available MC simulation software.

Selection of microstructure parameters

The two fascicles being identical, crossing-fascicle atoms are characterized by a single cylinder radius r and separation s and by their crossing angle θ in the xz -plane, after rotation of the cylinder aligned with the z -axis about the y -axis, as shown in Figure 3.4. The intra-axonal volume fraction f_{in} is given by³

$$f_{in} = \pi \left(\frac{r}{s} \right)^2, \quad (3.10)$$

and admits the upper bound $f_{in} \leq \frac{\pi}{4} \approx 0.7854$. We therefore keep the values 0.5, 0.65 and 0.75. To limit the number of atoms and the required simulation time, we discard a few of the intermediate radius values we had selected for single-fascicle atoms, as well as those larger than $17 \mu\text{m}$, as indicated in Table F.2 in Appendix F. It suffices to keep values of $\theta \in [0, \frac{\pi}{2}]$ by rotational symmetry. To be consistent with the theoretically achievable angular resolution of our 90-direction HARDI shells of about 21.4° (Equation (3.2), Section 3.1.2), we select the values $\theta = k\frac{\pi}{8}$, with $k = 1, \dots, 4$, since the increment $\frac{\pi}{8}$ then corresponds to a resolution of 22.5° . A total of 216 crossing-fascicle atoms are thus incorporated into our dictionary.

Determination of Monte Carlo simulation parameters

We determine the number N_{ex} of extra-axonal random walkers and the number of time steps T in a manner similar to that explained in Section 3.2.1 through Equations (3.8) and (3.9), with the typical atom dimension a defined here as (see Figure 3.4b)

$$a = \frac{\sqrt{2}}{2}s - r. \quad (3.11)$$

Validation of generated signals

Results are available in Appendix E.2 in Figures E.4, E.5 and E.6, which illustrate various crossing angles, intra-axonal fractions and radius values. It is interesting to note the similarity with single-fascicle atoms in terms of signal profile and order of magnitude, comparing for instance the curve/surface crossings associated with mid-size radii in Figures E.2 and E.5. Data visualization is performed by parametrizing the magnetic gradient directions of a given HARDI shell by the elevation angle α from the fascicles' plane and the angle β from the fascicles' bisector within the fascicles' plane, as drawn in Figure 3.4, after smooth interpolation from the 90 available data points. All

³Formula (3.10) is readily checked by considering the black square in Figure 3.4 as the elementary, infinitely-repeating pattern.

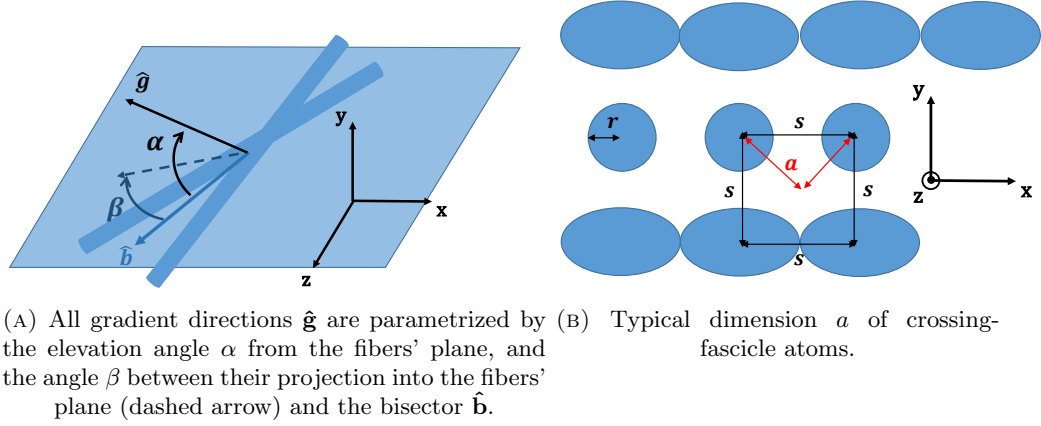


FIGURE 3.4: **Crossing fascicles modeled as arrays of axons crossing in interwoven planes.** Cylinder packing of fascicles crossing in interwoven planes parallel to the xz -plane. Cylinders have radius r and are a distance s from their neighboring cylinders.

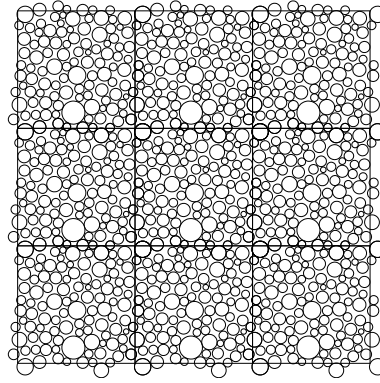


FIGURE 3.5: **Radius heterogeneity modeled through a Gamma distribution.** View in the xy -plane of a diffusion environment made of the repetition of a square region enclosing 100 cylinders with radii drawn from a Gamma distribution of given shape and scale parameters. This models axonal radius heterogeneity within fascicles.

signals appear relatively smooth, except maybe at high b -values again, when they are heavily attenuated.

3.2.3 Single fascicles of Gamma-distributed axons

The goal of this type of atom is to introduce radius heterogeneity within a single fascicle of infinite-length axons, as it has been histologically observed that axon radii might tend to follow Gamma distributions [15, 16]. To emulate this, we draw 100 radii from a given $\Gamma(a, b)$ distribution and attempt to pack the corresponding circles into a square region of the plane of side length L , through a trial and error algorithm implemented in the Camino software, a method described in [17]. The pattern is then periodically repeated to infinity, as depicted in Figure 3.5.

Selection of microstructure parameters

We use a basis of 11 pairs of Gamma shape and scale parameters (a, b) identified in [17] from radius histograms in [15, 16] and also consider the same distribution with radius values doubled, as in [17]. For each of the 22 (a, b) pairs, we determine by trial and error the smallest square length L able to fit all 100 cylinders, leading to intra-axonal volume fractions of $f_{in} \approx 0.733$ on average. We then experimentally increase L in order to get intra-axonal volume fractions of about 0.1 less. We thus generate a total of 44 atoms with parameter values summarized in Table F.2 in Appendix F.

Determination of Monte Carlo simulation parameters

We determine the number of time steps through Equation (3.8), taking the typical length a as

$$a = \mu_r - \sigma_r, \quad (3.12)$$

where $\mu_r = ab$ and $\sigma_r = \sqrt{ab}$ are respectively the mean and standard deviation of the distribution $\Gamma(a, b)$, and often adjusted to even smaller values to improve the quality of the extra-axonal signal simulation. This short length scale was clearly driven by smaller radii and led to large values of T and very long computation times, as reported in Table F.2 in Appendix F. As we had mentioned in Section 2.2.2, MC simulation algorithms allowing adaptive time steps such as the one proposed in [29] could lead to considerable gains in computation time.

The number of spins was determined on the basis of N_0 and f_{in} for each substrate as in Equation (3.9), taking $N_0 = 1.6 \times 10^5$ as suggested in [17] for the complete MC simulation.

The MCF method was run 100 times to generate the intra-axonal signal.

Validation of generated signals

Appendix E.3 provides graphs of the generated data. Figure E.7 presents the curves associated with one atom for HARDI shells spanning a large range of b-values, they seem smooth even at high b-values. Figure E.8 compares that same atom with its related atom of identical Gamma-distribution parameters (i.e. the same cylinders) but of lower packing density (i.e. packed in a larger square region). We observe lower signals at lower intra-axonal volume fractions, which was to be expected since large values of f_{in} correspond to tightest barriers and more restricted diffusion. Finally, Figure E.9 compares the signals from all 22 radius distributions at the highest f_{in} for a fixed

$b = 2319 \text{ s mm}^{-2}$. The curves are very similar to each other due to the fact that the distinct radius distributions present high similarity too. The mean radius takes values in the limited range $[0.232, 1.608] \text{ }\mu\text{m}$ for instance. Magnetic gradients perpendicular to the fiber direction seem most likely to discriminate between the different distributions.

3.2.4 Glial cells

Glial cells are abundant in the human brain as they serve to nurture and protect the neurons' axons, notably through the production of myelin (see Figure 1.6). Glial cells possess so-called *processes*, i.e. cellular extensions originating from the main cell body with lengths reaching 50 and up to 300 μm for some types of glial cells known as *astrocytes*, giving them a star-like appearance. Nearly all models in diffusion imaging therefore incorporate some sort of isotropic diffusion compartment or explicit spherical diffusion boundaries to account for the presence of more or less sphere-shaped cellular structures [13, 14, 17, 18, 26, 37]. It was shown in [26] that simple spherical models fitted and explained DW-MRI data better than more elaborate "astrostick" models, attempting to more faithfully reproduce the biological shape of glial cells. We therefore settle for a simple spherical model.

Selection of microstructure parameter

It is difficult to estimate typical sizes of glial cells since they can present complex cellular processes. The sphere model is more phenomenological than the models presented earlier for fascicles of axons and a wide range of sphere radii will likely need to be tested. Since no extra-axonal space is associated with this type of dictionary atom, we only have to run the much faster MCF method and can afford to sample radius values spanning the relatively large interval $[1, 150] \text{ }\mu\text{m}$.

Validation of generated signals

Only the exact result related to the MCF method is used here, which ensures the validity of the results presented in Appendix E.4.

Chapter 4

Exploratory analysis of the dictionary

In this chapter, we proceed to a preliminary analysis of our generated dictionary in order to assess the feasibility of ultimately characterizing microstructure configurations based on linear combinations of elementary atoms of the dictionary. Specifically, we first investigate whether fascicles of axons crossing in interwoven planes can be accurately described by the superposition of two single fascicles of axons. We then design a simple synthetic experiment to study the effect of noise on dictionary-matching of elementary atoms and examine which acquisition parameters yield the best performances.

The main results of this chapter may be summarized as follows.

§ 4.1 *Mixed results are obtained concerning the approximation of crossing-fascicle atoms through superposition of single-fascicle atoms, especially at high intra-axonal volume fraction f_{in} . Strong correlation is consistently observed between mathematical similarity of the atoms and similarity of their crossing angle, but this is not always the case for their intra-axonal volume fraction and the radius of their axons. Better results do seem to be obtained when the dictionary presents sufficient resolution or "fine granularity" in parameter values.*

§ 4.2 *Our experiment suggests that the estimation of microstructure parameters presents better accuracy when more acquisition parameters and more gradient intensity values are used, generally at moderately-high b-values. The gain in SNR of N-coil systems is retrieved and satisfactory preliminary results are presented regarding direct maximum-likelihood matching taking into account the non-central Chi structure of the acquisition noise, impractical in traditional non-dictionary frameworks.*

4.1 Challenging the superposition hypothesis for crossing fascicles

The purpose of this section is to investigate the validity of the superposition principle for fascicles of axons with different orientations, more specifically to check whether crossing fascicles can be accurately represented by the sum of two single fascicles. It is clear that the signal due to water molecules trapped *inside* axons follows the superposition principle if the axons' membranes are perfectly reflecting, which is assumed here. However, water molecules diffusing in the *extra*-axonal space experience different environments when they are evolving between two crossing fascicles or when only one fascicle of single orientation is present, compare for instance Figure 3.1 on page 43 and Figure 3.4 on page 48. Demonstrating that the superposition principle holds would allow us to considerably reduce the size of our dictionary and the subsequent complexity of sparse dictionary-matching. We could then only consider single-fascicle atoms and would not have to integrate every combination of 2, 3,... crossing fascicles at different angles, different radii, etc.

We denote by \mathcal{D}_{sing} the sub-dictionary made of the 180 single-fascicle atoms presented in Section 3.2.1 and by \mathcal{D}_{cross} the sub-dictionary made of the 216 crossing-fascicle atoms presented in Section 3.2.2. The microstructure parameters of \mathcal{D}_{sing} , i.e. the radius r and the intra-axonal volume fraction f_{in} are sampled more finely than in \mathcal{D}_{cross} , as summarized in Table F.2. We consider atoms defined over the $P = 360$ acquisition parameters of the clinically-realistic ActiveAx protocol presented in Section 3.1.1. Atoms can be thought of as vectors in \mathbb{R}^P and we will thus linearly combine them with one another.

4.1.1 Procedure

All single-fascicle atoms $A_i^{(sing)}$ from \mathcal{D}_{sing} are rotated by a given angle α_{ref} through an interpolation procedure explained in Appendix G and currently only possible with rotation-invariant acquisition schemes such as traditional HARDI shells, thus not yet adapted to CUSP-like and DSI schemes. Each rotated atom, taken as a vector in \mathbb{R}^P , is then added to the original atom to form a "crossing-fascicle-like" atom $\tilde{A}_i^{(cros)}$ with equal normalization factors 0.5 since we consider that the two fascicles occupy identical volumes. We then calculate the similarity between the "artificial" atom $\tilde{A}_i^{(cros)}$ and all the actual crossing-fascicle atoms $A_j^{(cros)}$ from \mathcal{D}_{cros} and investigate the relationship between mathematical similarity and microstructural "resemblance" in terms of the microstructural parameters r, f_{in} and α , with a simple similarity metric defined as the

cosine between two atoms taken as vectors in \mathbb{R}^P , where P is the number of acquisition parameters. Note that we tested other metrics such as the sum-of-squares and obtained similar results and conclusions. What matters here is to show that there exists at least one mathematical metric in which superposed single fascicles prove to be a good approximation of actual crossing fascicles.

4.1.2 Assessment of microstructural similarity

Consistence between microstructural and mathematical similarity is assessed by examining whether the similarity metric increases when crossing-fascicle atoms $A^{(cros)}$ have radii, intra-axonal volume fraction and crossing angle similar to those of $\tilde{A}_i^{(cros)}$. Note that an artificial atom $\tilde{A}_i^{(sing)}$ with cylinder radius 8.5 or 19 μm for instance cannot have a perfect match among \mathcal{D}_{cros} since those radius values are not present. We produce four types of graphs, for a given artificial atom $\tilde{A}^{(cros)}$ of characteristics $r_{ref}, f_{ref}, \alpha_{ref}$.

- **Similarity versus intra-axonal volume fraction** evolution of the similarity metric with the intra-axonal volume fraction f_{in} of crossing-fascicle atoms from \mathcal{D}_{cros} , considering only those crossing-fascicle atoms with crossing angle α_{ref} and cylinder radius as close to r_{ref} as possible, according to the possibilities of the sub-dictionaries;
- **Similarity versus cylinder radius** evolution of the similarity metric with the cylinder radius of crossing-fascicle atoms from \mathcal{D}_{cros} , considering only those crossing-fascicle atoms with crossing angle α_{ref} and intra-axonal volume fractions as close to f_{ref} as possible, according to the possibilities of the sub-dictionaries;
- **Similarity versus crossing angle** evolution of the similarity metric with the crossing angle of the crossing-fascicle atoms from \mathcal{D}_{cros} , considering only those crossing-fascicle atoms with cylinder radius as close to r_{ref} and intra-axonal volume fractions as close to f_{ref} as possible, according to the possibilities of the sub-dictionaries;
- **Matched radius** we compare r_{ref} to the cylinder radius of the true crossing-fascicle atom from \mathcal{D}_{cros} that presents the highest similarity with $\tilde{A}^{(cros)}$. Note that this matching atom does not necessarily posses the characteristics α_{ref} and f_{ref} .

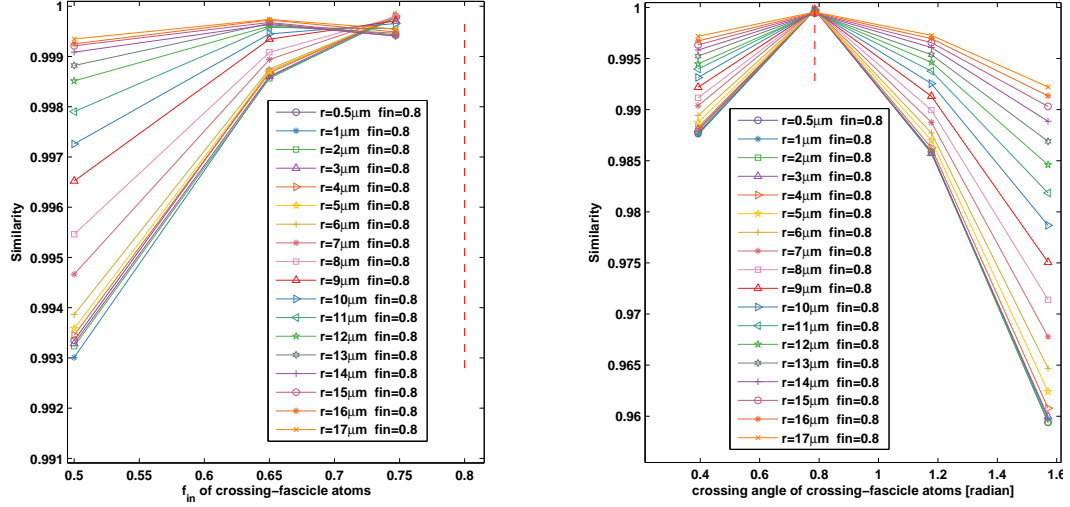
We consider three set-ups. In the "easy" set-up, both α_{ref} and f_{ref} of the artificial atom $\tilde{A}^{(cros)}$ are comprised in the sub-dictionary \mathcal{D}_{cros} . In the "intermediate" set-up, $\alpha_{ref} \in \mathcal{D}_{cros}$ but f_{ref} is no longer present in \mathcal{D}_{cros} . In the "difficult" set-up neither α_{ref} nor f_{ref} belongs to the sub-dictionary \mathcal{D}_{cros} of true crossing-fascicle atoms.

4.1.3 Results

The results associated to the easy set-up are available in Appendix H. Figure H.1 suggests that a maximum of similarity occurs at matching microstructural characteristics in relatively good agreement with the superposition principle.

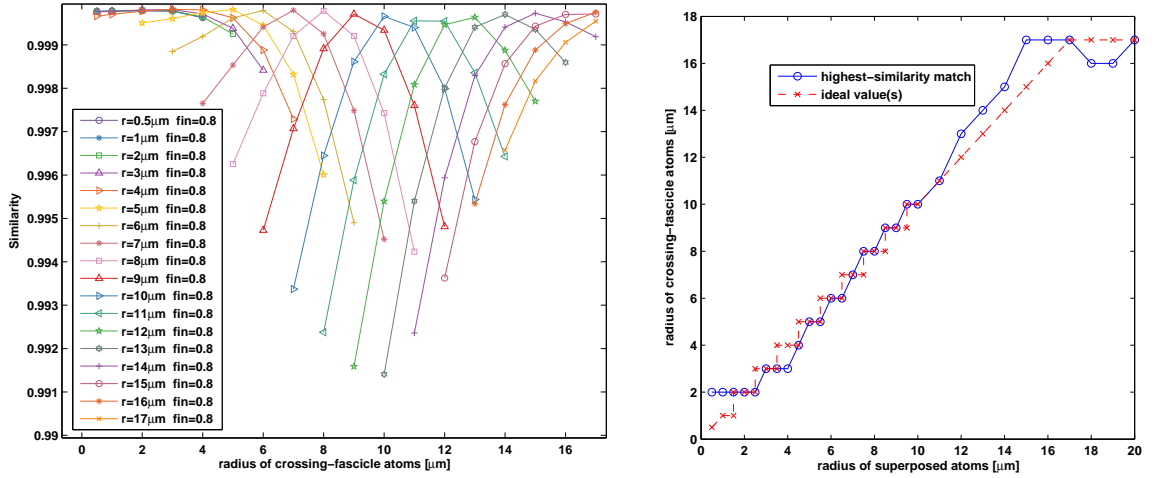
Figure 4.1 shows the results of the intermediate set-up. Similarity exhibits the expected "extrapolation" behavior, providing higher similarity values at the highest f_{in} available in the sub-dictionary, 0.75, for small radii up to 10 μm . However, artificial atoms with larger radii present higher similarity with crossing-fascicle atoms having lower $f_{in} = 0.65$. If the crossing angle is still recovered exactly in all cases, the matched radius values are imperfect for large and small radii outside the range $[5, 12]$ μm . These unexpected phenomena remain to be further investigated.

The results of the difficult set-up (Figure H.2 in Appendix H) confirm the excellent correlation between the fascicles' crossing angle and mathematical similarity, as a maximum would seem to occur at the true α_{ref} . However, departures from the expected extrapolation behavior are again observed at large radius values (9 μm and higher) for f_{in} and poorer radius matches are obtained.



(A) Similarity vs intra-axonal volume fraction of actual crossing fascicles at matching cylinder radius and crossing angle.

(B) Similarity vs crossing angle of actual crossing fascicles at matching cylinder radius and intra-axonal volume fraction.



(C) Similarity vs cylinder radius of actual crossing fascicles, at matching crossing angle and intra-axonal volume fraction. Curves associated to artificially-created atoms with radius that did not have a perfect match among \mathcal{D}_{cros} are not represented.

(D) Cylinder radius of matched crossing-fascicle atom in \mathcal{D}_{cros} vs true radius of artificial atom (up to 2 acceptable values).

FIGURE 4.1: **Superposition principle partially supported by "intermediate" set-up.** When $\alpha_{ref} = \frac{\pi}{4} \approx 0.785$ belongs to the sub-dictionary \mathcal{D}_{cros} while $f_{ref} = 0.8$ does not, (A) the intra-axonal volume fraction f_{in} seems well-extrapolated for radii up to 11 μm while larger radii tend to match lower-density crossing fascicles; (B) the crossing angle is still perfectly recovered ; (C)-(D) highest-similarity radii are only correct in the range 5 to 12 μm .

4.1.4 Discussion

The determination of the crossing angle through sparse reconstruction on large dictionaries seems promising as a peak of similarity never failed to occur at the best crossing angle available in the sub-dictionary \mathcal{D}_{cros} , in all three set-ups. Recovering the intra-axonal volume fraction and cylinder radius seems more delicate, particularly when extrapolation is required. This could indicate a limit of the superposition principle, which we recall is assumed in virtually every model in diffusion MRI (see Section 1.4.1).

However, in the "easy" set-up wherein f_{ref} and α_{ref} have an exact match in \mathcal{D}_{cros} , the results were almost perfect. This might indicate that the reconstruction of crossing fascicles from the superposition of single fascicles will gain accuracy if we incorporate sufficiently many microstructural parameter values in the elementary atoms of \mathcal{D}_{sing} . What's more, the case $f_{ref} = 0.5$ can probably be considered difficult because of its large fraction of "problematic" extra-axonal water molecules (f_{in} is typically 0.71 in human WM tissues [25]), recalling that the superposition principle is *exact* for intra-axonal signals when axonal membranes are perfectly reflecting as is the case here.

The mixed results obtained in the "intermediate" and "difficult" set-ups with $f_{ref} = 0.8 \notin \mathcal{D}_{cros}$ might be related to an apparent paradox: regularly-packed axons in a single fascicle can reach densities f_{in} of approximately 0.9 according to Equation (3.7), while density of fascicles crossing in interwoven planes (Figure 3.4, page 48) is limited to about 0.78. We leave it as an open question to investigate how to properly tackle the superposition of high-density fascicles.

We finally note that an experimental framework similar to the one described in this section could be used to assess the (dis)similarity between single fascicles of identical axons and fascicles presenting radius heterogeneity, for instance.

4.2 Resistance to noise

We now only consider the sub-dictionary \mathcal{D}_{sing} of single-fascicle atoms. The goal is to assess the quality of simple dictionary matching in the presence of noise, both in the Gaussian and non-central Chi (ncX) scenarios (see Section 1.1.3) while comparing the various acquisition protocols with which the data has been generated. Our subsequent experiments are thus closely related to Challenges II (sequence optimization) and III (DW-MRI resolution) presented in Section 1.4.

4.2.1 Procedure

Each of the 180 atoms of \mathcal{D}_{sing} is selected, synthetic noise is added to it and maximum-likelihood (ML) matching is performed among all 180 atoms of the sub-dictionary. The experiment is repeated N_{rep} times for each "noisy" acquisition.

We could in fact assume Gaussian noise *without loss of generality* because even in the case of magnitude-reconstructed image where the noise follows a ncX distribution (see Section 1.1.3), procedures such as outlined in [5] allow to approximately recover the underlying Gaussian signal of mean $\sqrt{N}S_{true}$ and variance σ_g , thus effectively increasing the SNR by a factor \sqrt{N} , where S_{true} is the true signal amplitude, N the number of detecting coils and where the SNR is defined as S_{true}/σ_g .

We first consider a purely Gaussian framework where we compare i) all 54 90-direction HARDI shells separately, ii) 8 single HARDI shells and their corresponding CUSP-like projections and iii) five complete acquisition protocols: the ActiveAx scheme and its CUSP-like counterpart, the NODDI scheme and its CUSP-like projection and the DSI scheme (more details in Section 3.1.1). ML-matching in the Gaussian scenario is done through the well-known Sum-of-Squares minimization.

We then consider a ncX-noise framework with N -coil magnitude-reconstructed acquisitions, studying the five traditional schemes mentioned above. We compare two maximum-likelihood methods, given a ncX-distributed acquisition $x \in \mathbb{R}^P$

- we assume the method in [5] operates a perfect transformation \tilde{x} of x so that $\tilde{x} \sim \mathcal{N}(\sqrt{N}S_{true}, \sigma_g^2)$ and use Sum-of-Squares matching as before;
- we perform direct ML-matching without resorting to any data transformation, computing the likelihood L_k of each atom k of the dictionary given the acquisition x , using Formula (1.3)

$$L_k = \prod_{i=1}^P f_{\tilde{x}}(x_i | \eta_{i,k}, \sigma_g, N) = \prod_{i=1}^P \frac{x_i^N}{\sigma_g^2 \eta_{i,k}^{N-1}} \exp\left(-\frac{x_i^2 + \eta_{i,k}^2}{2\sigma_g^2}\right) I_{N-1}\left(\frac{x_i \eta_{i,k}}{\sigma_g^2}\right), \quad (4.1)$$

where $\eta_{i,k} = \sqrt{N}E(\mathbf{p}_i, \Omega_k)$ is the scaled dictionary element corresponding to the i -th combination of PGSE parameters \mathbf{p}_i of the investigated protocol and where we suppose that σ_g has been reliably estimated. Unlike in traditional model fitting such as presented in Section 1.4.1, the mathematical complexity of the ncX pdf is not a limitation in the context of a discrete dictionary.

The matching quality is assessed through the statistics described below, at various SNR levels.

4.2.2 Assessment of resistance to noise

For each experiment, we extract the following statistics at different SNR levels

- **Average classification rank** : ranges from 1 (optimal) to 180 (worst possible). Average is taken over all the noisy atoms tested and N_{rep} repetitions;
- **1-micron-precision probability** : we compare the true cylinder radius value of the noisy atom to the cylinder radius of the first match and determine the (empirical) probability $P[|r_{true} - r_{match}| \leq 1 \mu\text{m}]$ that the error on the estimated cylinder radius be less than $1 \mu\text{m}$ (recalling that this is approximately the radius granularity of the sub-dictionary \mathcal{D}_{sing}) over all tested atoms and all N_{rep} repetitions;
- **Radius precision with confidence level α** : conversely, this gives the minimum precision value Δr_α for which

$$P[|r_{true} - r_{match}| \leq \Delta r_\alpha] \geq 1 - \alpha$$

holds, computed empirically over all tested atoms and all N_{rep} repetitions.

4.2.3 Results

We first present the results associated with the Gaussian framework in Figure 4.2, which displays the 1-micron-precision probability in the three cases i), ii) and iii) explained above. The two other types of graphs lead to identical observations and are available in Appendix H, Figures H.3 and H.4.

i) Single HARDI shells For clarity, the results of only 10 shells are presented in Figure 4.2a including the best 5 and 5 more among the 49 remaining shells, classified according to their results at the SNR level of 20. Moderate gradients of 40 mT m^{-1} and reasonably high b-values in the range $[1500, 2500] \text{ s mm}^{-2}$ seem to yield the best results. However, the accuracy is unsatisfactory at typically-encountered SNR values of about 20, indicating that 90 acquisitions at the same b-value do not allow to reliably discriminate between different microstructural fascicle configurations.

ii) HARDI vs CUSP shells We investigate whether using the same number of acquisitions but using multiple b-values can help increase the matching accuracy in noisy scenarios by comparing 8 HARDI shells with varying number of gradient directions to their CUSP counterparts. For clarity, only 4 comparisons are displayed in Figure 4.2b. Two trends appear

- the more acquisitions, the better : 90-direction shells fare better than 60- and 30-direction shells ;
- advantage for CUSP-like shells : it seems that using various gradient intensity values gives CUSP-like schemes a slight edge over regular HARDI shells as they consistently exceed the HARDI 1-micron error probability.

iii) Traditional acquisition schemes Since 90 acquisitions do not seem enough for the reliable estimation of microstructure parameters, we now compare traditional acquisition protocols with realistic numbers of acquisitions P ranging from 180 for NODDI to 515 in the DSI scheme. Figure H.3c now shows acceptable accuracy at usual SNR levels, with 1-micron-precision probabilities above 0.85 for all schemes except the NODDI-related protocols. The domination of the DSI scheme might be somewhat unfair and mainly due to a higher number of acquisitions.

Non-central Chi framework Figure 4.3 shows the comparison of Gaussian-based and ncX-based ML matching in the case of magnitude-reconstructed DW-MRI acquisitions, displaying only two out of the five acquisition protocols for clarity. As expected, we observe the effective gain in SNR of $\sqrt{\frac{N_1}{N_0}}$ when comparing N_0 -coil to N_1 -coil systems in the Gaussian framework. In the ncX case, this formula is only valid asymptotically for large SNR values (see Section 1.1.3).

We also see that ML-matching on the transformed data consistently outperforms direct ML matching on the untouched, ncX-distributed data, assuming that the data transformation to recover the underlying Gaussian-distributed data is perfect. This is further discussed in the next paragraph.

4.2.4 Discussion

The preceding experiments seem to suggest that increasing the number of acquisitions and the number of gradient intensity values leads to better matching and parameter estimation, particularly at moderately high b-values in the range $[1500, 2500]\text{s mm}^{-2}$. The exact influence of each individual parameter G, Δ, δ remains unclear at first sight and further investigation could be directed towards their optimization.

The experiments realized with ncX-distributed acquisitions would encourage the use of data-transformational frameworks such as outlined in [41] as it seems that working with Gaussian-distributed data leads to better results than directly using the ncX data. We should stress however that the procedure in [41] is unlikely to perfectly recover the underlying Gaussian distribution because it requires a potentially delicate smooth

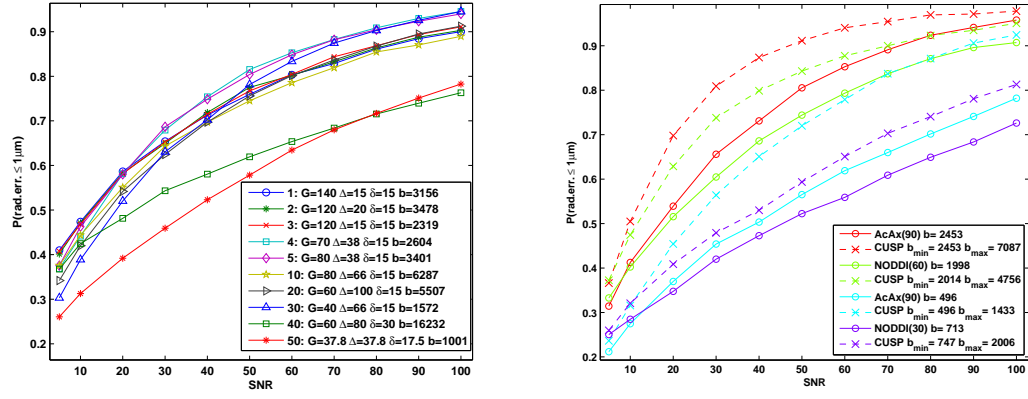
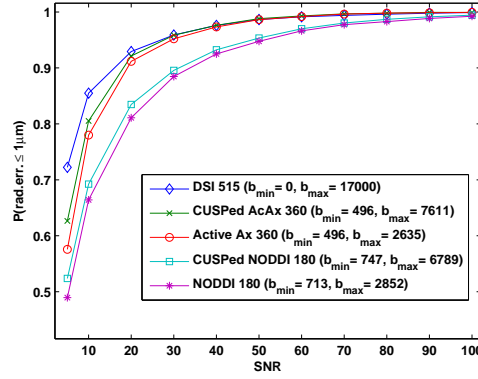
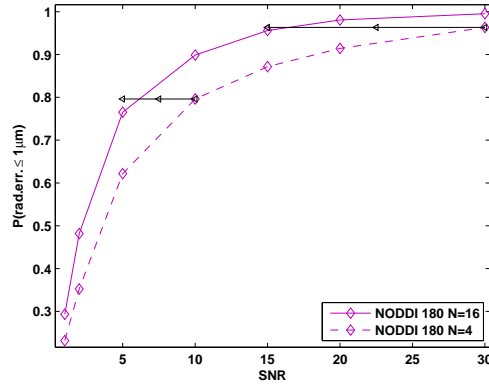
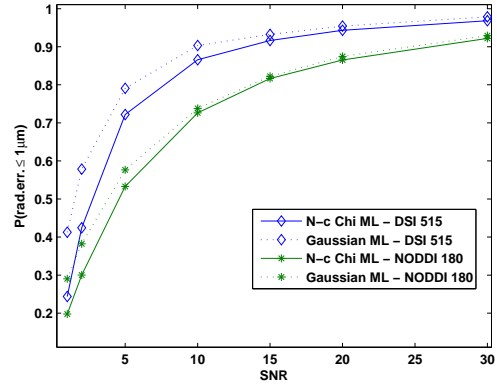
(A) 10 out of the 54 available 90-direction HARDI shells ($N_{rep} = 50$).(B) HARDI vs CUSP shells ($N_{rep} = 75$).(c) Complete traditional acquisition protocols ($N_{rep} = 75$).

FIGURE 4.2: **More acquisitions and more gradient intensities lead to better matching.** Probability of making less than a 1-micron error on the estimated radius for (A) single HARDI shells, (B) HARDI shells and their CUSP projections, (C) five traditional acquisition protocols (the number in the legend indicates the number of acquisitions). The order of appearance in the legend is based on an SNR level of 20. Units of G are in mTm^{-1} , Δ and δ in ms and b in mm^{-2} .

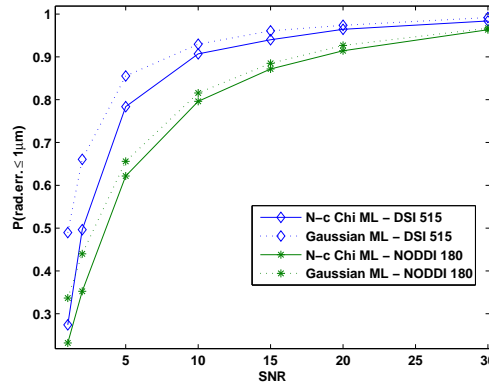
interpolation of the data as a function of the acquisition parameters \mathbf{p} (i.e. up to 5 independent variables in a general PGSE sequence), an estimation of σ_g^2 and the resolution of a numerically-sensitive non-linear equation. In contrast, direct ML matching on the acquired data only requires an estimate of σ_g^2 for which various experimental procedures have been proposed [20, 38–41] and might therefore be of practical interest.



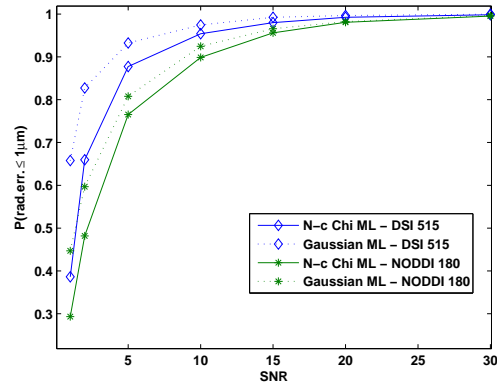
(A) \sqrt{N} -shift on SNR resulting from increasing N at fixed σ_g in each coil.



(B) $N = 2$.



(C) $N = 4$.



(D) $N = 16$.

FIGURE 4.3: **Gaussian ML theoretically leads to better matching than ncX ML.** $P[|r_{true} - r_{match}| \leq 1 \mu\text{m}]$ as a function of the SNR in a single coil, for different numbers of coils N , both in the Gaussian and non-central Chi ML framework. We observe an effective gain of approximately $\sqrt{16/4} = 2$ between (C) and (D), as illustrated in (A). Performing ML matching on the underlying Gaussian signals seems to provide more accurate results than directly on the non-central-Chi-distributed acquired signals, supposing the Gaussian distribution is perfectly recovered from the acquisitions.

Conclusion

In this work, we have generated a dictionary of elementary but biologically relevant microstructure configurations, large enough for insightful preliminary analyses.

During the construction of the dictionary, we have investigated methods that make little to no mathematical simplifications in generating DW-MRI data. The hybrid method validated in Chapter 2 provides higher efficiency and accuracy than complete Monte Carlo simulations, traditionally considered as providing groundtruth, for a few important microstructure configurations. The generated signals can thus be safely used for the validation of simpler mathematical models.

More sophisticated MC simulation methods such as the Fast Random Walk algorithm [29] along with code parallelization could allow to expand our dictionary in a more convenient way by significantly reducing the very high computation times that we have reported throughout Chapter 3 while avoiding the need to resort to heuristics for the determination of acceptable MC simulation parameters.

Our dictionary has already allowed us to identify limitations related to the approximation of complex DW-MRI signals as the superposition of simpler signals, a hypothesis made in nearly all traditional models and an issue that will need to be addressed if we want to further pursue parameter estimation based on sparse linear combinations. We were also able to show that the optimization of acquisition sequences can be performed when such a dictionary is available.

In the future, it will probably be of interest to integrate more types of elementary atoms into our dictionary such as undulating or myelinated axons, of great biologic relevance, or other types of DW-MRI sequences than the PGSE sequence we have limited ourselves to. It will also be necessary to mathematically compare single fascicles of identical axons to fascicles incorporating radius heterogeneity. Many more studies can certainly be carried out on such a rich database of signals, hopefully contributing to a better characterization of our brain.

Appendix A

The spin echo experiment

Figure A.1 provides a schematic description of the evolution of the net magnetization during the spin echo experiment, which forms the basis of nearly all diffusion MRI experiments.

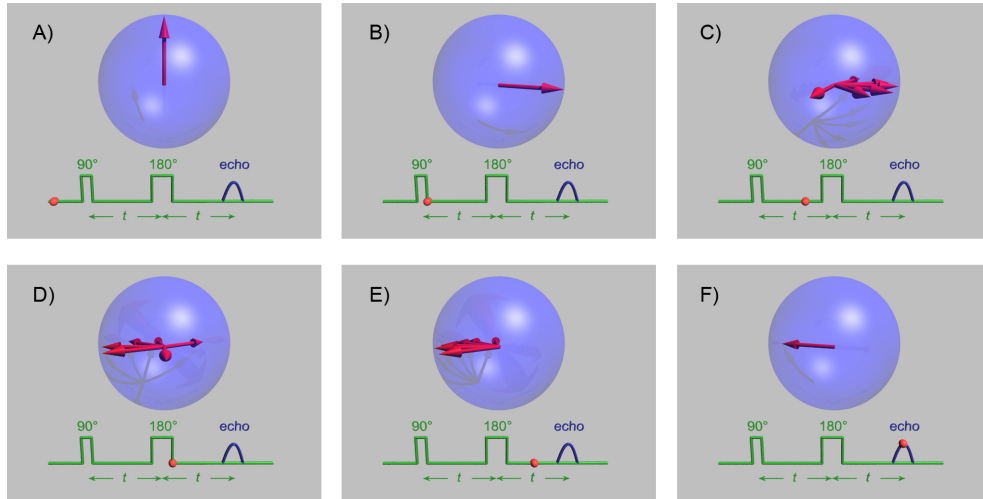


FIGURE A.1: **Measuring the transverse magnetization made possible by the spin echo experiment.** **A.** All the protons' magnetic moments are parallel or anti-parallel to the the external magnetic field \mathbf{B}_0 (not represented). Net magnetization (red arrow) is longitudinal. **B.** The first RF pulse makes protons precess together in phase, the net magnetization is in the transverse xy -plane. **C.** Local magnetic field inhomogeneities cause some protons to precess more rapidly than others, a dephasing occurs. **D.** A second RF pulse is applied to invert all the protons' phases. **E.** Slow-precessing protons now catch up with the main transverse magnetization while fast-precessing ones drift back. **F.** Refocusing is complete, a "spin echo" is formed with strong transverse magnetization than can be measured. Note that the concurrent return of the net magnetization towards the vertical (T1-relaxation) is not shown here.

Source: http://en.wikipedia.org/wiki/Spin_echo.

Appendix B

The SGP and GPD approximations

This appendix briefly describes to commonly-used approximations used in diffusion-weighted imaging.

The SGP approximation

In the short gradient pulse (SGP) approximation, it is assumed that the the duration δ of each gradient $\mathbf{g} = G\hat{\mathbf{g}}$ is so short that the diffusion of spins during their application is negligible. In particular, this requires, in an n -dimensional space, that $\delta \ll \frac{L^2}{2nD}$, where L is the characteristic length of the medium (e.g. the radius of a sphere-shaped glial cell) and D the diffusivity. However, it is assumed that the dephasing of spins during each gradient pulse takes a finite, non-zero value. In short : $\delta \rightarrow 0$ with $0 < \delta G < \infty$. Under these assumptions, it can be shown that the signal attenuation $E(\mathbf{p}_{pgse}; \Omega)$ associated with the PGSE parameters $\mathbf{p}_{pgse} = (\mathbf{g}, \Delta, \delta)$ and the diffusion environment Ω is given by [3, §2.2.3]

$$E(\mathbf{p}_{pgse}; \Omega) = \int_{\Omega} P(\mathbf{r}, \Delta) e^{i2\pi \mathbf{q} \cdot \mathbf{r}} d\mathbf{r} = \text{FT} \{P(\mathbf{r}, \Delta)\}(\mathbf{q}), \quad (\text{B.1})$$

where we defined the vector $\mathbf{q} = \frac{1}{2\pi} \gamma \delta \mathbf{g}$ and where $P(\mathbf{r}, \Delta)$ is the average diffusion propagator in Ω . This propagator, just like the Gaussian kernel for unbounded domains of equation (1.7), can be interpreted as the probability for a spin to make a displacement \mathbf{r} in a time interval Δ , and is independent of the starting position thanks to the spatial homogeneity of Brownian motion [42, §6.3]. Equation (B.1) leads to an elegant Fourier relationship between the measured signal and the average propagator $P(\mathbf{r}, \Delta)$, a technique known as \mathbf{q} -space imaging that has been extensively used [37, 43, 44].

We chose not to make use of the SGP approximation in our subsequent developments because of the restrictive hypothesis on δ whereas we wish to test as diverse a range of PGSE parameters as possible in our dictionary. In addition, computing (B.1) involves finding $P(\mathbf{r}, \Delta)$, which amounts to solving the diffusion equation (1.6) in Ω . We will see in Section 2.3 that we can do much better by solving an even simpler equation.

The GPD approximation

Inspecting equation (1.8), which gave the accumulated phase shift of a diffusing spin of Brownian trajectory $\mathbf{r}(t)$

$$\phi = \underbrace{\gamma \int_{t_1}^{t_1+\delta} \mathbf{g} \cdot \mathbf{r}(t) dt}_{\text{gradient dephasing}} - \underbrace{\gamma \int_{t_1+\Delta}^{t_1+\Delta+\delta} \mathbf{g} \cdot \mathbf{r}(t) dt}_{\text{gradient rephasing}}, \quad (\text{B.2})$$

we see that if $\mathbf{r}(t)$ is a zero-mean Gaussian variable, such as in the case of free, Gaussian diffusion, then as a consequence of the central limit theorem, so is ϕ [3, §2.3.3]. This is the main assumption behind the Gaussian phase distribution (GPD) approximation. The distribution of ϕ is then entirely determined by its second moment $\langle \phi^2 \rangle$ which can be shown to ultimately depend on an integral involving the probability $\rho(\mathbf{r}_0)$ of a spin to be at the initial position \mathbf{r}_0 (usually taken to be uniform) and the diffusion propagator $P(\mathbf{r}_0, \mathbf{r}_1, t)$ in Ω [3, §2.3.3]. With $P_\Phi(\phi)$ known, the signal attenuation E_{pgse} follows from $E_{pgse} = \mathbb{E}[e^{i\phi}]$ (see equation (1.9)).

Although the GPD approximation does take into account a finite value of δ , it is only valid in cases where the diffusion can be considered to be Gaussian (i.e. free, unrestricted) which is usually the case for short diffusion times Δ , as most particles are not given enough time to reach the boundaries of the enclosing geometry. Conversely, for very long Δ 's, a spin will explore the domain multiple times, its displacements will look like independent jumps between random points of Ω and the accumulated displacements will again converge to a Gaussian trajectory. The GPD approximation has long been conjectured to be valid in the intermediate case too until counterexamples were experimentally found [45] and remains widely used in practice, recall for instance the ActiveAx model presented in Section 1.4.1. We will not use it to synthetically generate DW-MRI signals because of this important limitation. What's more, the determination of $\langle \phi^2 \rangle$ involves finding the diffusion propagator through the resolution of the diffusion equation in Ω , just as in the SGP approximation. We can obtain better results by solving a simpler problem, as we will see in Section 2.3.

Appendix C

The multiple correlation function approach

This appendix details the mathematical derivation of the MCF formula for DW-MRI signals resulting from the applications of gradients \mathbf{g} with fixed direction $\hat{\mathbf{g}}$ and piecewise-constant intensity profile $f(t)$. This profile would successively take the values $G, 0$ and $-G$ in a PGSE sequence for instance (see Figure 1.4).

We first make the equation non-dimensional for convenience. We then briefly review the theory associated with the Laplace operator and see how we can proceed to a eigenfunction expansion of the solution. This expansion allows to reduce the problem of solving the difficult Bloch-Torrey PDE into two simpler problems : first solving the time-independent Laplace eigenvalue problem to extract the eigenfunctions, and then solving an infinite system of linear EDO's, which admits a simple analytical solution.

Nondimensionalization First of all, it is convenient to set $\mathbf{r} = L_0 \tilde{\mathbf{r}}$, with L_0 the characteristic length scale of the diffusion environment Ω , $\tilde{M}_{xy}(\tilde{\mathbf{r}}, t) = M_{xy}(L_0 \tilde{\mathbf{r}}, t)$ and $\mathbf{g} = G \hat{\mathbf{g}}$. Then we obtain the operator $\Delta_{\mathbf{r}} = \frac{1}{L_0^2} \Delta_{\tilde{\mathbf{r}}}$ and the Bloch-Torrey equation for the complex-valued transverse magnetization $M_{xy}(\mathbf{r}, t)$ becomes, in the case of isotropic diffusion ($\mathbf{D} = D \cdot \mathbf{Id}$) and dropping the tildes for convenience,

$$T \frac{\partial M_{xy}}{\partial t}(\mathbf{r}, t) = \underbrace{\frac{DT}{L_0^2}}_{:=p} \Delta M_{xy}(\mathbf{r}, t) - i \underbrace{\gamma G L_0 T}_{:=q} B(\mathbf{r}) M_{xy}(\mathbf{r}, t), \quad (\text{C.1})$$

where we multiplied both sides by a characteristic time scale T , for instance the echo time TE , and where $B(\mathbf{r}) = \hat{\mathbf{g}} \cdot \frac{\mathbf{r}}{L_0}$ is the normalized dimensionless spatial profile of

the applied magnetic field, assumed constant for now. We also defined two important dimensionless numbers $p = \frac{DT}{L_0^2}$ and $q = \gamma GL_0 T$.

Spectrum of the Laplace operator The eigenfunctions $u_m(\mathbf{r})$ and eigenvalues λ_m of the Laplace operator in a bounded domain Ω with Neumann boundary conditions are defined as

$$\begin{cases} \Delta u_m(\mathbf{r}) + \lambda_m u_m(\mathbf{r}) = 0 & \forall \mathbf{r} \in \Omega \\ \frac{\partial u_m}{\partial \hat{\mathbf{n}}}(\mathbf{r}) = 0 & \forall \mathbf{r} \in \partial\Omega. \end{cases} \quad (\text{C.2})$$

It can be shown that since the Laplace operator is compact and self-adjoint on the separable Hilbert space $L^2(\Omega)$ ¹ for any open, bounded set Ω , its eigenvalues are such that $0 \leq \lambda_0 < \lambda_1 < \dots$ with $\lim_{n \rightarrow +\infty} \lambda_n = +\infty$, and its associated eigenfunctions form an orthonormal basis of $L^2(\Omega)$ [46, §9.8], i.e.

$$\int_{\Omega} u_m(\mathbf{r}) u_n(\mathbf{r}) d\mathbf{r} = \delta_{mn} \quad \forall m, n \geq 0, \quad (\text{C.3})$$

$$f(\mathbf{r}) = \sum_{m=0}^{\infty} \underbrace{\int_{\Omega} f(\mathbf{r}') u_m(\mathbf{r}') d\mathbf{r}'}_{c_m} u_m(\mathbf{r}) \quad \forall f \in L^2(\Omega), \quad (\text{C.4})$$

where δ_{mn} is the kronecker symbol. Further inspection of the eigenvalue problem (C.2) reveals that $\lambda_0 = 0$ with $u_0(\mathbf{r}) = \frac{1}{\sqrt{|\Omega|}}$, and that for $m > 0$

$$\int_{\Omega} u_m(\mathbf{r}) d\mathbf{r} = -\frac{1}{\lambda_m} \int_{\Omega} \Delta u_m(\mathbf{r}) d\mathbf{r} = -\frac{1}{\lambda_m} \int_{\partial\Omega} \frac{\partial u_m}{\partial \hat{\mathbf{n}}}(\mathbf{r}) ds = 0, \quad (\text{C.5})$$

making use of the divergence theorem and recalling the Neumann boundary condition.

Decomposition of the solution in Laplace eigenfunctions, in the case of constant gradient Since the solution $M_{xy}(\mathbf{r}, t)$ of the Bloch-Torrey equation must physically be continuous on $\bar{\Omega}$ for all t and since Ω is bounded, we have $M_{xy}(\cdot, t) \in L^2(\Omega)$ for all t and may use (C.4) to decompose it as

$$M_{xy}(\mathbf{r}, t) = \sum_{m'} c_{m'}(t) u_{m'}(\mathbf{r}), \quad (\text{C.6})$$

with unknown coefficients $c_{m'}(t)$, defined in some given interval $[t_0, t_f]$ during which the applied gradient \mathbf{g} is constant. Substituting (C.6) into (C.1), multiplying by $u_m(\mathbf{r})$ and integrating over Ω leads to an infinite set of ODE's on the time-dependent coefficients

¹The Lebesgue space of *square-integrable* functions is defined as $L^2(\Omega) = \{f : \Omega \rightarrow \mathbb{R}; f \text{ is measurable and } \int_{\Omega} |f|^2 d\mathbf{r} < \infty\}$, where measurability and integrability are taken with respect to Lebesgue measure. It is a Hilbert space when equipped with the inner product $(u, v) = \int_{\Omega} uv$.

$c_m(t)$, for $t \in [t_0, t_f]$,

$$T \frac{\partial c_m}{\partial t}(t) = - \sum_{m'} \left(p \lambda_{m'} \delta_{m'm} + i q \int_{\Omega} u_m(\mathbf{r}) B(\mathbf{r}) u_{m'}(\mathbf{r}) d\mathbf{r} \right) c_{m'}(t) \quad (\text{C.7})$$

for any $m = 0, 1, \dots$, where we used (C.2) to replace $\Delta u_{m'}$ by $-\lambda_{m'} u_{m'}$ and the orthonormality relationships (C.3). Equations (C.7) can be compactly rewritten in matrix form, the solution of which is the matrix exponential

$$T \frac{\partial C}{\partial t}(t) = -(p\Lambda + iq\mathcal{B}) C(t) \Leftrightarrow C(t) = e^{-(p\Lambda + iq\mathcal{B}) \frac{(t-t_0)}{T}} \cdot C(t_0), \quad (\text{C.8})$$

where we consider $C(t)$ as an infinite-dimensional vector of components $c_0(t), c_1(t), \dots$. The diagonal matrix Λ has diagonal elements $\Lambda_{mm} = \lambda_m$ and the symmetric matrix \mathcal{B} has elements $\mathcal{B}_{mm'} = \int_{\Omega} u_m(\mathbf{r}) B(\mathbf{r}) u_{m'}(\mathbf{r}) d\mathbf{r}$. Writing $M_{xy}(\mathbf{r}, t_0) = \sum_{m'} c_{m'}(t_0) u_{m'}(\mathbf{r})$ from (C.6), we observe by identification with (C.4) that the coefficients $c_{m'}(t_0)$ making up $C(t_0)$ are the coefficients of the eigenfunction expansion of the initial condition $M_{xy}(\mathbf{r}, t_0)$, thus of the form $c_{m'}(t_0) = \int_{\Omega} M_{xy}(\mathbf{r}, t_0) u_{m'}(\mathbf{r}) d\mathbf{r}$.

Using the eigenfunction expansion at time t_f , we can express the transverse magnetization $M_{xy}(\mathbf{r}, t_f)$ as

$$\begin{aligned} M_{xy}(\mathbf{r}, t_f) &= \sum_{m'} u_{m'}(\mathbf{r}) c_{m'}(t_f) \\ &= U(\mathbf{r})^T C(t_f) \\ &= U(\mathbf{r})^T \exp \left(-(p\Lambda + iq\mathcal{B}) \frac{(t_f - t_0)}{T} \right) C(t_0), \end{aligned} \quad (\text{C.9})$$

where $U(\mathbf{r})$ is the infinite-dimensional vector with components $U_{m'} = u_{m'}(\mathbf{r})$, the last equality follows from (C.8) and where the final-value coefficient vector $C(t_f) = e^{-(p\Lambda + iq\mathcal{B}) \frac{(t_f - t_0)}{T}} \cdot C(t_0)$. $C(t_0)$ can be seen as some sort of time propagation of $C(t_0)$ through the matrix exponential.

Solution for general gradient profiles If the applied gradient has fixed direction $\hat{\mathbf{g}}$ and a piecewise constant intensity profile $f(t)$ taking values $f_k = f(t_k)$ for $t \in [t_k, t_{k+1}]$, then we can apply the previous procedure taking as initial value coefficient vector $C(t_k)$ in the interval $[t_k, t_{k+1}]$ the final-value coefficient vector $C(t_k)$ in the preceding interval

$[t_{k-1}, t_k]$. We then obtain, if $0 = t_0 < t_1 < \dots < t_{K-1} < t_K = TE$,

$$M_{xy}(\mathbf{r}, TE) = \sum_{m'} u_{m'}(\mathbf{r}) c_{m'}(TE) \quad (\text{C.10})$$

$$= U(\mathbf{r})^T \left[\prod_{k=1}^K \exp \left(- (p\Lambda + iqf_{k-1}\mathcal{B}) \frac{(t_k - t_{k-1})}{T} \right) \right] C(0). \quad (\text{C.11})$$

The DW-MRI signal attenuation $E_{\mathbf{g}}$ associated to a temporally piecewise constant magnetic gradient \mathbf{g} is finally obtained from integrating $M_{xy}(\mathbf{r}, TE)$, yielding

$$\begin{aligned} E_{\mathbf{g}} &= \int_{\Omega} M_{xy}(\mathbf{r}, TE) \, d\mathbf{r} \\ &= \sum_{m'} \int_{\Omega} u_{m'}(\mathbf{r}) \, d\mathbf{r} \, c_{m'}(TE) \\ &= \tilde{U}^T \left[\prod_{k=1}^K \exp \left(- (p\Lambda + iqf_{k-1}\mathcal{B}) \frac{(t_k - t_{k-1})}{T} \right) \right] C(0), \end{aligned} \quad (\text{C.12})$$

where \tilde{U} is an infinite dimensional vector of components defined as $\tilde{U}_{m'} = \int_{\Omega} u_{m'}(\mathbf{r}) \, d\mathbf{r}$.

Considering that the initial transverse magnetization is uniform just after the 90° RF pulse, i.e. $M_{xy}(\mathbf{r}, 0) = \frac{1}{\sqrt{|\Omega|}}$, and utilizing the identities (C.5), we obtain

$$\begin{aligned} c_0(0) &= \tilde{U}_0 = 1, \\ c_{m'}(0) &= \tilde{U}_{m'} = 0 \quad \forall m' > 0, \end{aligned} \quad (\text{C.13})$$

which yields the following *exact* result for the signal attenuation

$$E_{\mathbf{g}}(TE) = \left[\prod_{k=1}^K \exp \left(- (p\Lambda + iqf_{k-1}\mathcal{B}) \frac{(t_k - t_{k-1})}{T} \right) \right]_{0,0}, \quad (\text{C.14})$$

where $[\cdot]_{0,0}$ denotes the first diagonal element of the infinite-dimensional matrix.

Appendix D

Traditional acquisition protocols selected for the dictionary

This appendix describes 4 commonly-used PGSE acquisition protocols integrated into our dictionary of DW-MRI signals. We will make use of the b-vector notation, inspired from the traditional b-value defined in Equation 1.14

$$\mathbf{b} := (\gamma\delta G)^2 \frac{\mathbf{g}}{G} (\Delta - \delta/3) = b\hat{\mathbf{g}}. \quad (\text{D.1})$$

ActiveAx sampling scheme

This scheme was introduced in [17] to estimate distributions of axon diameters in human white matter in vivo. It is available on Camino’s ActiveAx tutorial page ¹.

The protocol is essentially an optimized multi-shell HARDI acquisition. The optimization procedure, originally described in [32], proposes to minimize the variance of the parameters of a simple model based on the CHARMED model [37] and similar to the microstructural models presented in Section 1.4.1, through the minimization of the Cramer-Rao Lower Bound, while ensuring that the obtained sequences remain clinically feasible. The minimization yields the optimal values of $M = 4$ shells of $N = 90$ gradient directions, yielding a total of 360 acquisition parameters, and provides the 4 related combinations of G, Δ and δ .

¹<http://cmic.cs.ucl.ac.uk/camino//index.php?n=Tutorials.ActiveAx>, although strictly speaking, the scheme file that is provided on the web page corresponds to experiments conducted on monkeys and reported in the same paper. We thus extracted the gradient directions and set the parameters G, Δ and δ to the values recommended for the human protocol provided in that same paper.

NODDI sampling scheme

Similarly, the NODDI protocol is a classical 2-shell HARDI scheme introduced in [18] to validate the three-compartment tissue model incorporating neurite orientation dispersion, briefly introduced in Section 1.4.1.

The PGSE parameters G , Δ and δ and the multi-shell HARDI parameters M and N are determined through an optimization similar to that used for the ActiveAx scheme [32] with the additional restriction that the total number of acquisition must be limited to 90 so as to maintain an human-bearable acquisition time on their available hardware. The optimization procedure leads to $M = 2$ shells and provides the corresponding gradient strengths G_1 and G_2 , as well as the values for Δ and δ , identical for both shells. They choose to sample the outer shell (that of higher b-value) at twice the angular resolution of the inner shell, i.e. $N_1 = 30$ and $N_2 = 60$, as DW-MRI signals at high b-values are thought to have greater sensitivity to complex microstructure configurations [47].

The scheme is not readily available online so we generated the gradient directions by minimizing the generalized electrostatic potential energy, known as Reisz s-energy, of charged particles on a sphere. We also incorporated two intermediate shells sampled at respectively 30 and 60 angular directions, leading to a total of 180 acquisition sequences. These two extra shells are used in the original NODDI paper to form a richer protocol and provide pseudo ground-truth for model validation.

DSI sampling scheme

A diffusion spectrum imaging, or DSI-like sampling scheme [27] differs from HARDI-type protocols in that it is not based on shells of constant b-values but rather on a lattice sampling of the q-space with a fixed Δ , where the vector \mathbf{q} is defined as

$$\mathbf{q} = \gamma\delta\mathbf{g}, \quad (\text{D.2})$$

with γ the gyromagnetic ratio of protons. More specifically, δ is also fixed and the magnetic gradient \mathbf{g} varies across the points of a cubic lattice contained within a sphere of maximum q-value. Since \mathbf{q} and \mathbf{b} differ only by a constant in this case, the values of \mathbf{g} are also distributed across a cubic lattice with a restriction on the norm G .

The DSI scheme used in this work comes from the 2013 HARDI Reconstruction Challenge training data² and comprises 515 points in the b-space with 411 independent

²available on http://hardi.epfl.ch/static/events/2013_ISBI/testing_data.html#classical-sampling-schemes.

gradient directions (since some of them are colinear with the origin). The b-values and gradient strengths were scaled to match those reported in the original DSI paper [27].

CUSP schemes

In a Cube and Sphere protocol (CUSP), a restriction is imposed on the $\|\cdot\|_\infty$ norm of the gradient vector \mathbf{g} instead of limiting its euclidean norm $\|\mathbf{g}\|_2 = G$. Concretely, we impose [13]

$$|g_x|, |g_y|, |g_z| \leq G_{max} \quad (\text{D.3})$$

and thereby force \mathbf{g} to lie within the cube enclosing the sphere of radius G_{max} . This is based on the fact that magnetic gradients are usually generated by the combined action of three independent coils in MRI-scanners.

Starting from a shell of radius G in the \mathbf{g} -space, gradients of magnitude up to $\sqrt{2}G_{max}$ and $\sqrt{3}G_{max}$ can be obtained in the hexahedral and tetrahedral directions respectively by relaxing the constraint $G \leq G_{max}$ to the above constraint (D.3).

We proceed to the CUSP projection of each HARDI shell contained in the ActiveAx and NODDI schemes and refer to them as CUSPed ActiveAx and CUSPed NODDI, respectively.

Appendix E

Validation of the generated DW-MRI signals

This appendix provides the Figures intended for the validation of the DW-MRI signals generated with the hybrid method (Section 2.4) described in Sections 3.2.1, 3.2.2, 3.2.3 and 3.2.4. In Figures E.1, E.2 and E.3, related to single fascicles of identical axons, as well as in Figures E.7, E.8 and E.9, related to single fascicles with Gamma-distributed axons, each axon has orientation \mathbf{n} and signals are plotted as a function of the dot product $\mathbf{n} \cdot \hat{\mathbf{g}}$ for all 90 magnetic gradient directions $\hat{\mathbf{g}}$, at fixed PGSE parameters G, Δ and δ .

In the 2D-representations of Figures E.4, E.5 and E.6 related to crossing fascicles of identical axons, α is the elevation angle from the fibers' plane and β is the angle from the fascicles' bisector direction \mathbf{b} , taken in the fascicles' plane, as depicted in Figure 3.4 on page 48. The black crosses in the fascicles' plane ($\alpha = 0$) indicate the directions of the two fibers either side of the bisector while the red crosses mark the directions perpendicular to either fascicle.

E.1 Single fascicles of identical axons

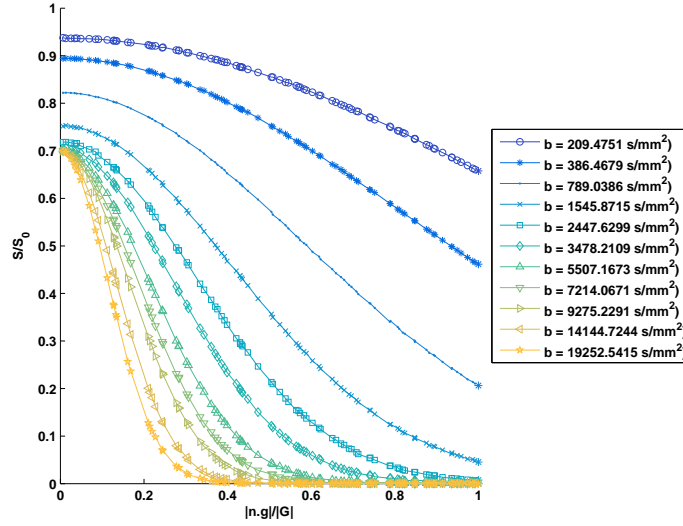


FIGURE E.1: **Smooth hybrid signals for single-fascicle atoms of small axonal radius.** DW-MRI signals generated through the hybrid method corresponding to a single-fascicle atom of identical axons with smallest sampled radius $r = 0.5 \mu\text{m}$ and intra-axonal volume fraction $f_{in} = 0.7$. All signals exhibit satisfactory smoothness.

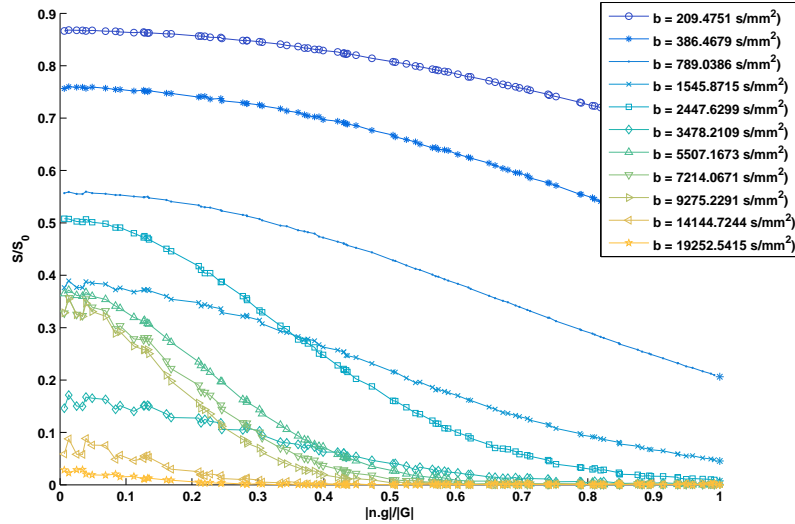


FIGURE E.2: **Smooth hybrid signals for single-fascicle atoms of intermediate axonal radius.** DW-MRI signals generated through the hybrid method corresponding to a single-fascicle atom of identical axons with moderately large radius $r = 7.5 \mu\text{m}$ and intra-axonal volume fraction $f_{in} = 0.6$. Signals at higher b-values show some irregularity, especially for magnetic gradients perpendicular to the axons' axis \mathbf{n} , certainly due to a poor estimation of integral (1.8) through the discretization (2.3) when intense magnetic gradients are applied.

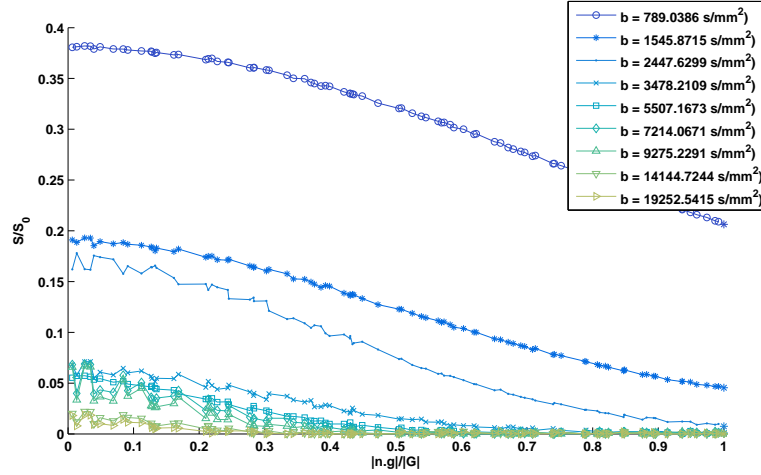


FIGURE E.3: **Smooth hybrid signals for single-fascicle atoms of large axonal radius.** DW-MRI signals generated through the hybrid method corresponding to a single-fascicle atom of identical axons with very large radius $r = 18 \mu\text{m}$ and typical $f_{in} = 0.7$. Signals at higher b-values show some irregularity, especially for magnetic gradients perpendicular to the axons' axis \mathbf{n} , certainly due to a poor estimation of integral (1.8) through the discretization (2.3) when intense magnetic gradients are applied.

E.2 Crossing fascicles of identical axons

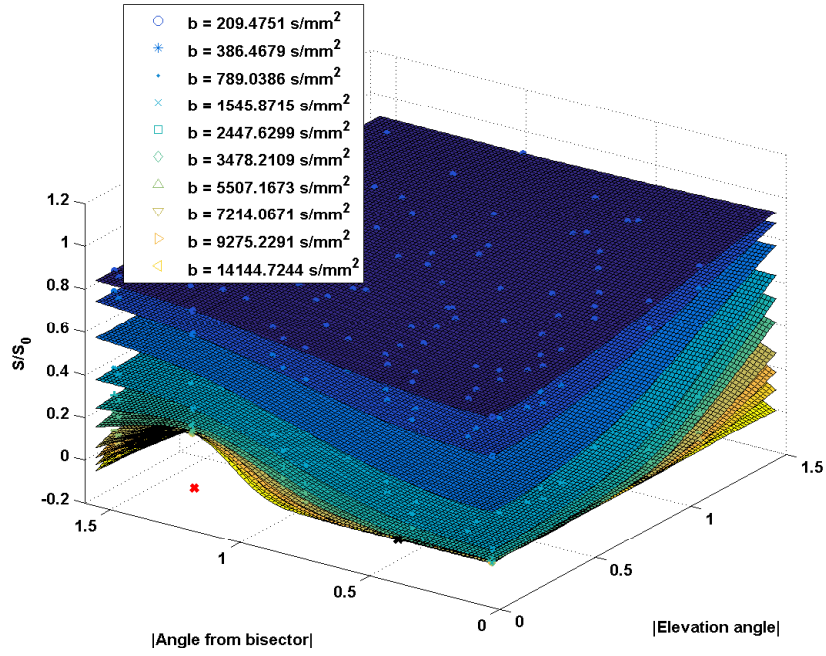


FIGURE E.4: **Smooth hybrid signals for crossing-fascicle atoms of small axonal radius.** DW-MRI signals generated through the hybrid method corresponding to crossing fascicles of identical axons with smallest available radius $r = 0.5 \mu\text{m}$, intra-axonal volume fraction $f_{in} = 0.5$ and crossing angle $\theta = \frac{\pi}{4}$.

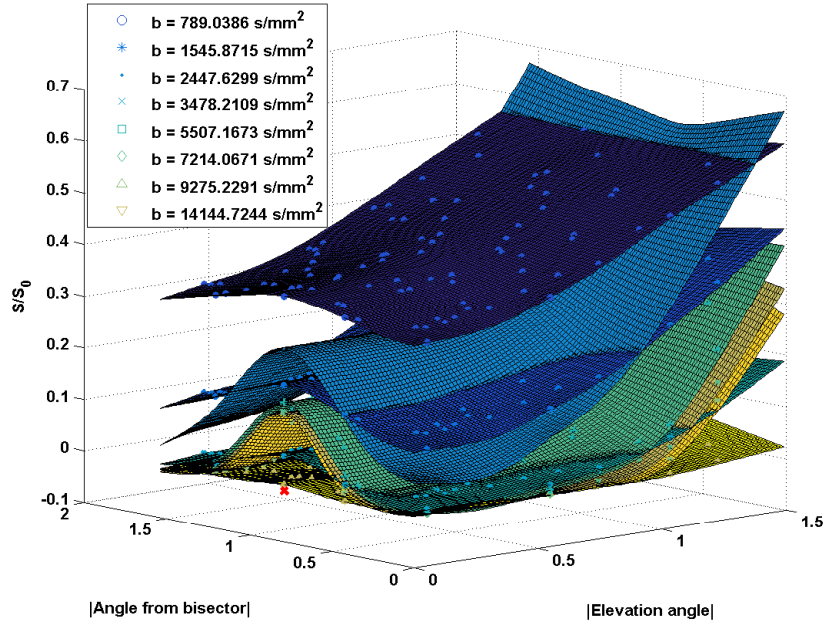


FIGURE E.5: **Smooth hybrid signals for crossing-fascicle atoms of moderately-large axonal radius.** DW-MRI signals generated through the hybrid method corresponding to crossing fascicles of identical axons of relatively large radius $r = 9 \mu\text{m}$, intra-axonal volume fraction $f_{in} = 0.75$ and crossing angle $\theta = \frac{\pi}{2}$. We observe the crossings of curves occurring in the same range of radius values with single-fascicle atoms, as shown in Figure E.2.

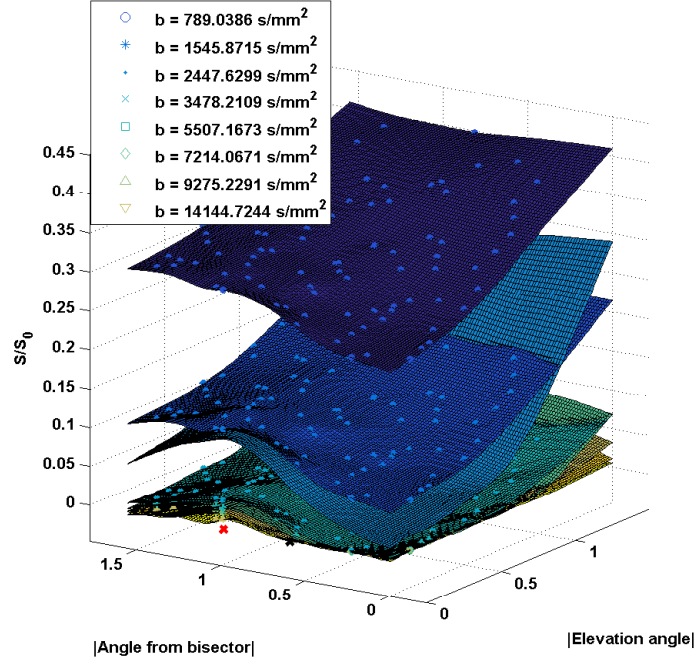


FIGURE E.6: **Smooth hybrid signals for crossing-fascicle atoms of large axonal radius.** DW-MRI signals generated through the hybrid method corresponding to crossing fascicles of identical axons of large radius $r = 16 \mu\text{m}$, intra-axonal volume fraction $f_{in} = 0.65$ and crossing angle $\theta = \frac{3\pi}{8}$. We observe the crossings of curves and orders of magnitude similar to those shown in Figure E.3, related to single-fascicle atoms.

E.3 Single fascicles of Gamma-distributed axons

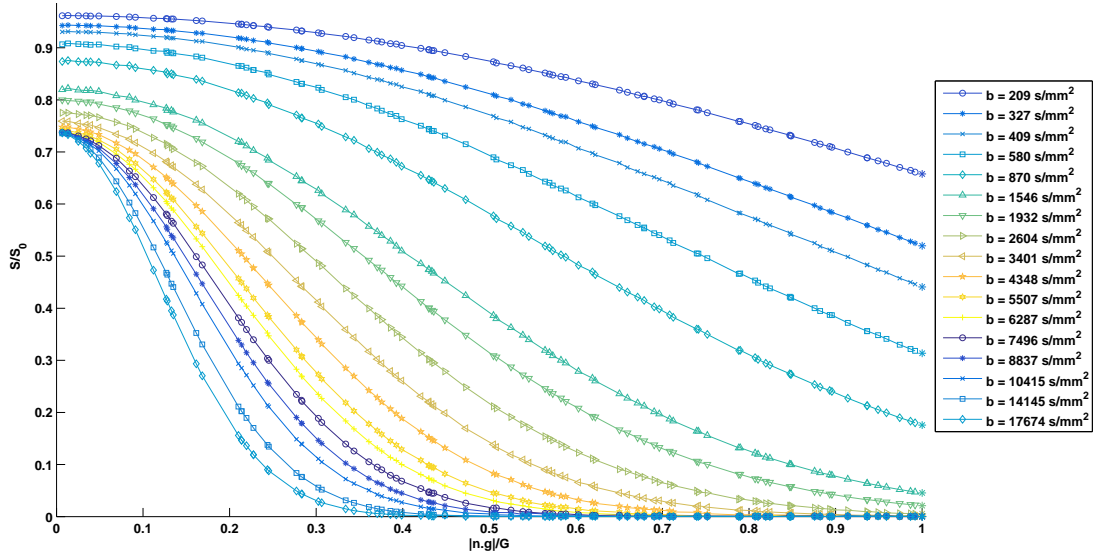


FIGURE E.7: **Smooth hybrid signals for single-fascicle atoms of varying axonal radii.** DW-MRI signals generated through the hybrid method of a so-called Gamma-distributed atom of parameters $\mu_r = 0.532 \mu\text{m}$ and $f_{in} = 0.737$, for 90-direction HARDI shells of b-values ranging from 209 to $17\,674 \text{ s mm}^{-2}$.

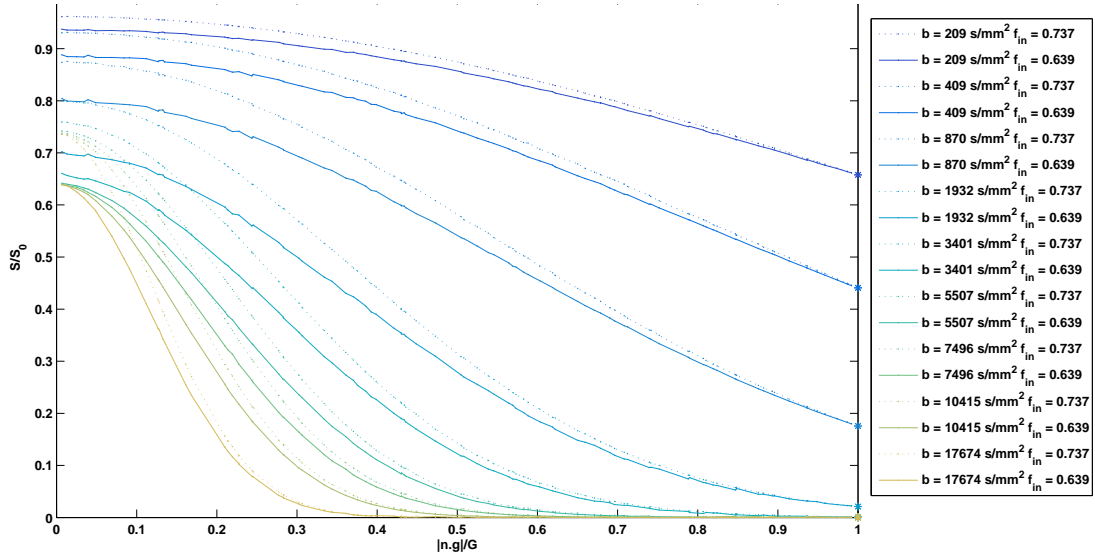


FIGURE E.8: **Verification that hybrid signals show higher intensity at higher axonal density.** DW-MRI signals generated through the hybrid method of two Gamma atoms with radii drawn from the same distribution of mean $\mu_r = 0.535 \mu\text{m}$ and standard deviation $\sigma_r = 0.233 \mu\text{m}$ but with distinct intra-axonal volume fractions. More densely-packed axons oppose more restriction to diffusion and logically present higher signal intensities.

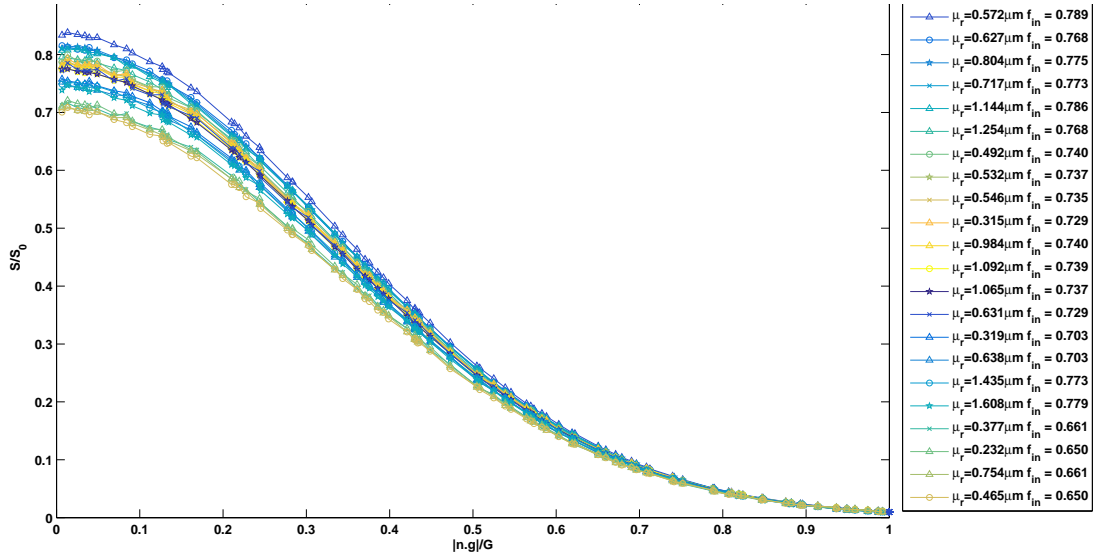


FIGURE E.9: **Verification that hybrid signals seem to present higher intensity in the presence of more diffusion restrictions.** DW-MRI signals generated through the hybrid method for all 44 Gamma-distributed atoms, with acquisition parameters $G = 120 \text{ mT m}^{-1}$, $\Delta = 15 \text{ ms}$ and $\delta = 15 \text{ ms}$, leading to a b-value of $b = 2319 \text{ s mm}^{-2}$. The legend classifies the signals according to their value at $\hat{\mathbf{g}} \cdot \mathbf{n} \approx 0.11$. It seems that higher intra-axonal volume fractions and smaller radius values correspond to more diffusion restriction and higher DW-MRI signals. All results converge to the free-diffusion signal when the applied gradients are parallel to the axons' principal direction.

E.4 Glial cells

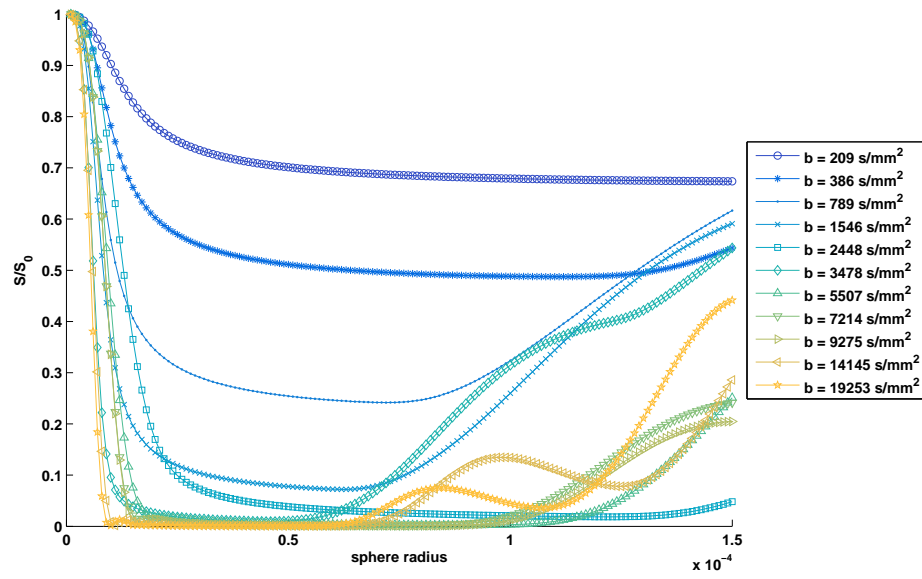


FIGURE E.10: **Smooth hybrid signals for spheres of varying radii.** DW-MRI signals of spherical glial cells presented as a function of the sphere radius for a large range of b -values, with 90 gradient directions per HARDI shell. We globally observe a decrease in signal intensity as the radius first increases, as water molecules are given more freedom to diffuse, followed by a increase for very large radii and diffraction-like patterns.

Appendix F

Dictionary parameters

Table F.1 summarizes and classifies the 6095 PGSE acquisition parameters selected for the generation of our dictionary while Table F.2 presents the selected atom types, their microstructure parameter values as well as the associated simulation times.

Acquisition protocol	\hat{g}	G [mT m ⁻¹]	Δ [ms]	δ [ms]	TE [ms]	b [s mm ⁻²]
ActiveAx	S1 : 90sp	57	87	5	122	496
	S2 : 90sp	60	20	13		682
	S3 : 90sp	46	77	15		2453
	S4 : 90sp	58	80	12		2635
CUSPed ActiveAx	S1 : 90cb	57-98.7	87	5	122	496-1488
	S2 : 90cb	60-103.9	20	13		682-2047
	S3 : 90cb	46-79.7	77	15		2453-7360
	S4 : 90cb	58-100.5	80	12		2635-7905
NODDI	S1 : 30sp	31.9	37.8	17.5	78	711
	S2 : 60sp	63.8				2855
	v-S1 : 30sp	37.8				1000
	v-S2 : 60sp	53.4				2000
CUSPed NODDI	S1: 30cb	31.9-55.3	37.8	17.5	78	711-2133
	S2 : 60cb	63.8-110.5				2855-8565
	v-S1 : 30cb	37.8-65.5				1000-3000
	v-S2 : 60cb	53.4-92.5				2000-6000
DSI	515lt	0-40	66	60	156	680-17000 (23 values)
Extra HARDI	S1-S50 : 90sp	40-140 (6)	15-100 (6)	2-30 (3)	30-130 (13)	209-19253 (50 values)

TABLE F.1: **Acquisition parameters.** Summary of all the selected parameter sets. The \hat{g} column contains the number of gradient directions in each shell (S) or validation-shell (v-S for NODDI) and whether they are distributed over a sphere (sp), a cube (cb) or a lattice (lt).

Atom type	Param.	Param. values	# values	# atoms	MC time	MCF time
Sing. fasc. identical axons	r	$[0.5:0.5:10, 11:1:20] \mu\text{m}$	30	180	3590 hrs (150 days)	225 mins (3 hrs 45 mins)
	f_{in}	$[0.4, 0.5, 0.6, 0.7, 0.8, 0.9]$	6			
Cross. fasc. identical axons	r	$[0.5, 1:1:17] \mu\text{m}$	18	216	5370 hrs (224 days)	540 mins (9 hrs)
	f_{in}	$[0.5, 0.65, 0.747]$	3			
	θ	$[\frac{\pi}{8}, \frac{\pi}{4}, \frac{3\pi}{8}, \frac{\pi}{2}] \text{ rad}$	4			
Sing. fasc. $\Gamma(a, b)$ -distributed axons	$\mu_r = ab$	0.232 to 1.608 μm	22	44	31000 hrs (1292 days)	85 hrs
	$\sigma_r = \sqrt{a} \cdot b$	0.0576 to 0.889 μm	pairs			
	f_{in}	0.564 to 0.789	2 per pair			
Glial cells	r	$[1:1:150] \mu\text{m}$	150	150	\	4 hrs

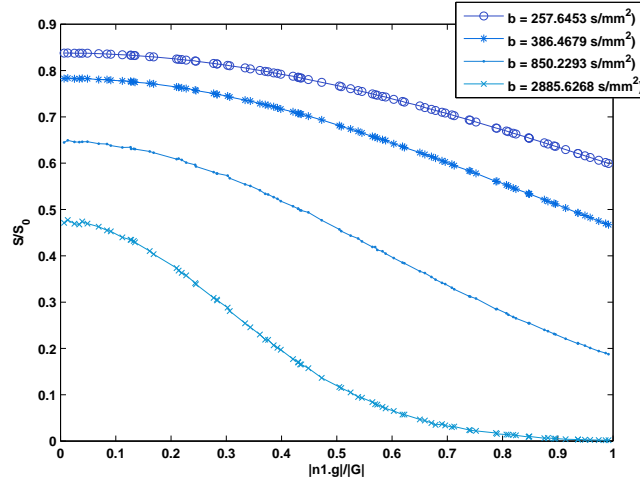
TABLE F.2: **Microstructure parameters.** Microstructure parameters of the 4 elementary atoms of the dictionary : single fascicles and crossing fascicles of identical axons, single fascicles of Gamma-distributed radii and spherical glial cells. Total simulation times for the extra-cellular signal (MC) and intra-cellular signal (MCF) are reported. Enumerations of N parameter values of the type $[v_1 : \Delta v : v_N]$ are to be interpreted in a MATLAB-like fashion.

Appendix G

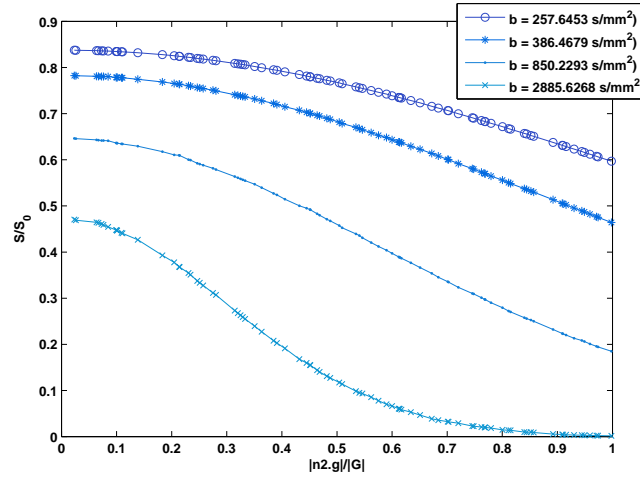
Rotation of single-fascicle atoms

Given a so-called single-fascicle atom $E\left(\{\mathbf{p}_i\}_{1 \leq i \leq P}; \Omega_0\right) \in \mathbb{R}^P$ such as described 3.2.1, where $\mathbf{p}_1, \dots, \mathbf{p}_P$ denote P successive acquisition sequences and $\Omega_0 = (r, f_{in}, \mathbf{n}_0)$ characterizes the single-fascicle substrate through its cylinder radius r , intra-axonal volume fraction f_{in} and orientation \mathbf{n}_0 , the problem is to find the atom of DW-MRI signals associated to the *same* acquisition sequences but to the "rotated" diffusion environment $\Omega_\theta = (r, f_{in}, \mathbf{n}_\theta)$ of identical r and f_{in} but new fascicle orientation \mathbf{n}_θ .

We assume that all acquisitions $\mathbf{p}_1, \dots, \mathbf{p}_P$ correspond to a HARDI shell, i.e. they have identical parameters G_i, Δ_i, δ_i , for $i = 1, \dots, P$ but gradient orientations $\hat{\mathbf{g}}_i$ uniformly distributed over a sphere. Exploiting the symmetry of the protocol, the signal values can be conveniently represented as a 1D-function of the variable $|\hat{\mathbf{g}}^T \mathbf{n}|$. This is illustrated in Figure G.1a and has been used repeatedly in Chapters 2 and 3. The problem is thus to estimate the values of $E(\mathbf{p}_j; \Omega_\theta)$ at the new "query" points $|\hat{\mathbf{g}}_j^T \mathbf{n}_\theta|$, with $j = 1, \dots, P$, from the known "data" points $(|\hat{\mathbf{g}}_i^T \mathbf{n}_0|, E(\mathbf{p}_i; \Omega_0))$, for $i = 1, \dots, P$. This amounts to simple 1-dimensional interpolation/extrapolation. We observed heuristically that linear-spline interpolation produced smooth and stable results (see Figure G.1), more stable for instance than cubic-spline fitting, in particular when extrapolating for query points $\hat{\mathbf{g}}_j^T \mathbf{n}_\theta$ outside the range of the data points $|\hat{\mathbf{g}}_i^T \mathbf{n}_0|$.



(A) DW-MRI signals $E\left(\{\mathbf{p}_i\}_{1 \leq i \leq P}; \Omega_0\right)$ of a single-fascicle atom of orientation \mathbf{n}_0 , as a function of $|\hat{\mathbf{g}}^T \mathbf{n}_0|$.



(B) DW-MRI signals $E\left(\{\mathbf{p}_i\}_{1 \leq i \leq P}; \Omega_\theta\right)$ of a single-fascicle atom of orientation \mathbf{n}_θ , as a function of $|\hat{\mathbf{g}}^T \mathbf{n}_\theta|$.

FIGURE G.1: Rotationally-invariant acquisitions of single-fascicle atoms can be accurately rotated through simple 1D interpolation. DW-MRI signals of a single-fascicle atom plotted as a function of the projection of each gradient orientation $\hat{\mathbf{g}}_i$ onto the fascicle orientation \mathbf{n}_0 in Figure G.1a and the signal corresponding to its rotated version in Figure G.1b, plotted against the new orientation \mathbf{n}_θ . The signals are almost identical, as expected from the rotational symmetry of a HARDI protocol.

Appendix H

Exploratory analysis of the dictionary

Superposition principle for crossing fascicles

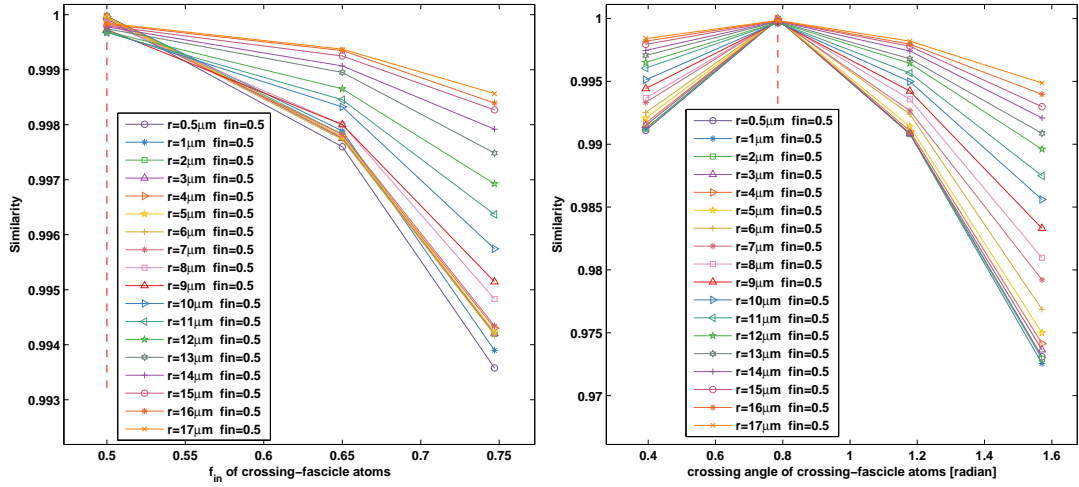
This appendix contains the results associated with the "easy" (Figure H.1) and "difficult" (Figure H.2) set-ups explored in Section 4.1.3 in order to investigate the validity of the superposition principle for crossing fascicles of axons.

The first experiment seems to uphold the superposition principle while the latter presents mixed results, supportive of the superposition principle for the recovery of the crossing angle but sometimes performing unexpectedly for the recovery of the intra-axonal volume fraction f_{in} and cylinder radius r .

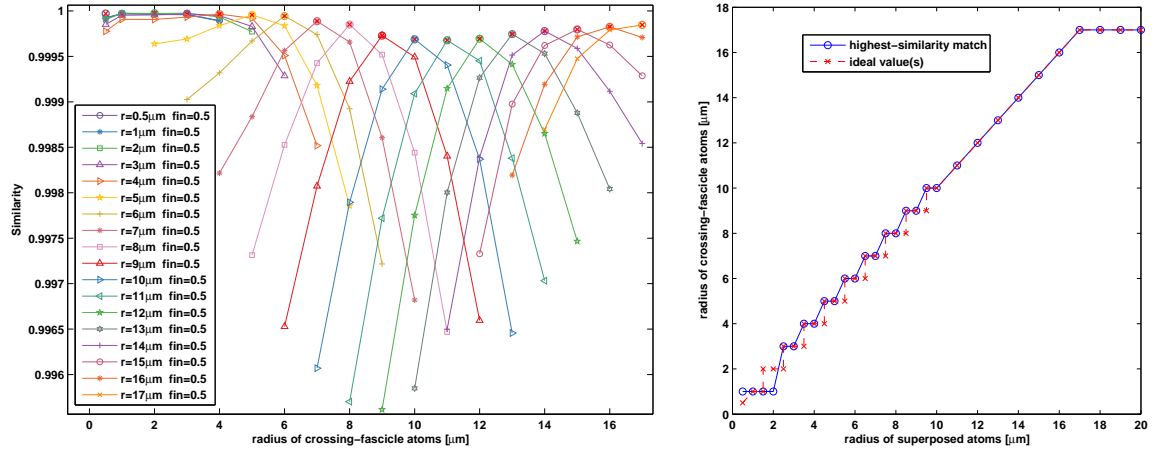
Red vertical dashed lines indicate the true underlying values of the microstructural parameters f_{in}, α, r . When comparing r_{ref} with the radius of the atom from \mathcal{D}_{cros} with highest mathematical similarity, radius values not present in \mathcal{D}_{cros} are allowed to match the two closest available values in \mathcal{D}_{cros} , hence the stair-like red curves on Figures H.1d and H.2d.

Resistance to noise

Figures H.3 and H.4 present the results associated to the experiments carried out in Section 4.2. It appears that all 5 schemes consistently find the true underlying atom within the first 3 matches (see Figure H.3) and it is worth noting that further inspection of the results reveal that the other top matches are usually "resembling" atoms in terms

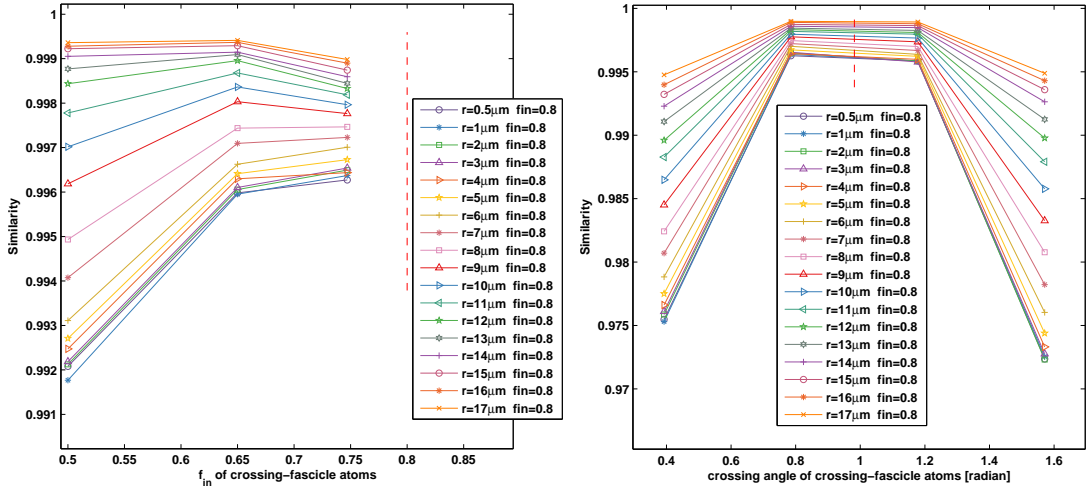


(A) Similarity vs intra-axonal volume fraction of actual crossing fascicles at matching cylinder radius and crossing angle. (B) Similarity vs crossing angle of actual crossing fascicles at matching cylinder radius and intra-axonal volume fraction.

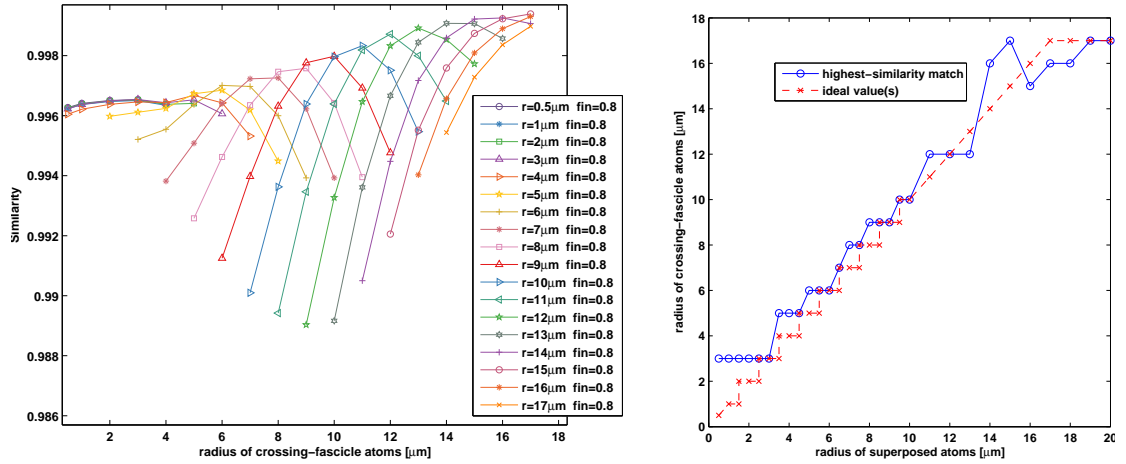


(C) Similarity vs cylinder radius of actual crossing fascicles, (D) Cylinder radius of matched crossing-fascicle atom in \mathcal{D}_{cross} vs true radius of artificial atom. Curves associated to artificially-created atoms with radius that did not have a perfect match among \mathcal{D}_{cross} are not represented.

FIGURE H.1: **Superposition principle backed by "easy" set-up.** When both $f_{ref} = 0.5$ and $\alpha_{ref} = \frac{\pi}{4} \approx 0.785$ belong to the sub-dictionary \mathcal{D}_{cross} of true crossing-fascicle atoms, the superposition principle seems to hold reasonably well, as the matching microstructural properties f_{in} , α and r correlate with higher mathematical similarity in all cases except for 2 small radius values in (D).

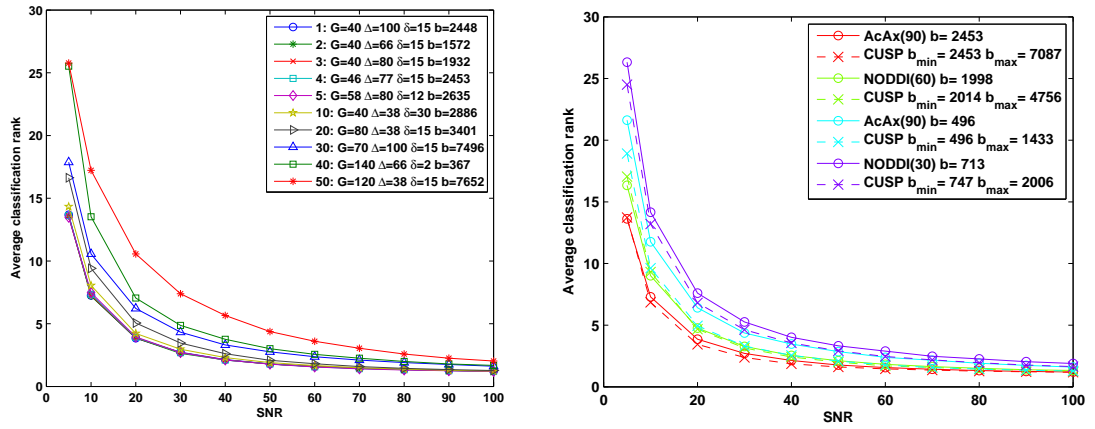


(A) Similarity vs intra-axonal volume fraction of actual crossing fascicles at matching cylinder radius and crossing angle. (B) Similarity vs crossing angle of actual crossing fascicles at matching cylinder radius and intra-axonal volume fraction.



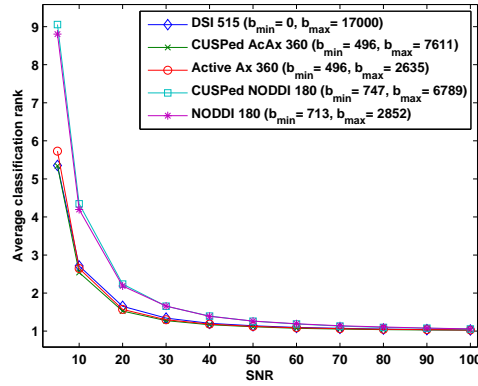
(C) Similarity vs cylinder radius of actual crossing fascicles, at matching crossing angle and intra-axonal volume fraction. Curves associated to artificially-created atoms with radius that did not have a perfect match among \mathcal{D}_{cros} are not represented. (D) Cylinder radius of matched crossing-fascicle atom in \mathcal{D}_{cros} vs true radius of artificial atom.

FIGURE H.2: Validity of superposition principle challenged in "difficult" set-up. When neither $f_{ref} = 0.8$ nor $\alpha_{ref} = \frac{5\pi}{16} \approx 0.982$ belongs to the sub-dictionary \mathcal{D}_{cros} of true crossing-fascicle atoms, extrapolation of f_{in} at radius values of 9 μm and higher and recovery of r are not completely supporting the superposition principle hypothesis. The appropriate crossing angle still appears to be recovered however.



(A) 10 out of the 54 available 90-direction HARDI shells ($N_{rep} = 50$).

(B) HARDI vs CUSP shells ($N_{rep} = 75$).



(c) Complete traditional acquisition protocols ($N_{rep} = 75$).

FIGURE H.3: More acquisitions and more gradient intensities lead to better matching. Average classification rank for (A) single HARDI shells, (B) HARDI shells and their CUSP projections, (C) five traditional acquisition protocols (the number in the legend indicates the number of acquisitions). The order of appearance in the legend is based on an SNR level of 20. Units of G are in mTm^{-1} , Δ and δ in ms and b in mm^{-2} .

of cylinder radius and intra-axonal volume fraction. Multi-CUSP-like schemes still seem to have a slight edge over their multi-HARDI equivalents.

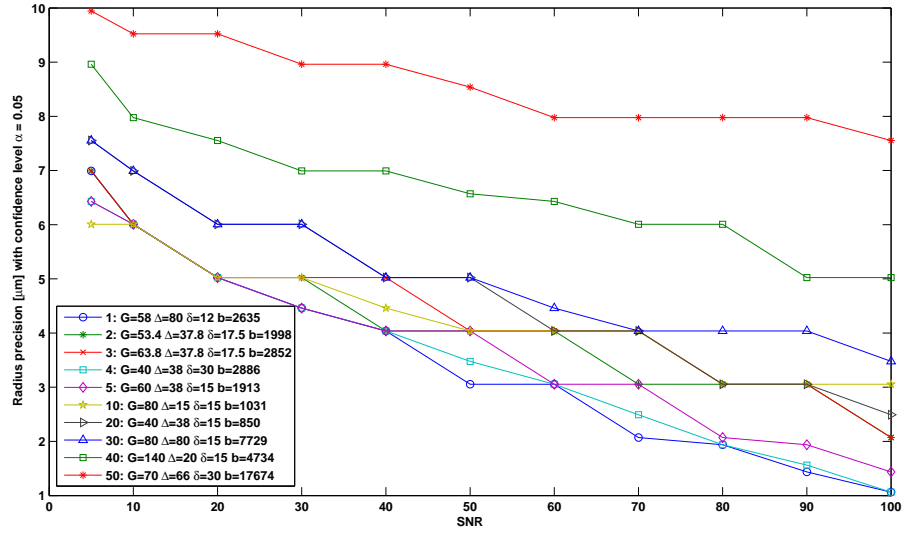
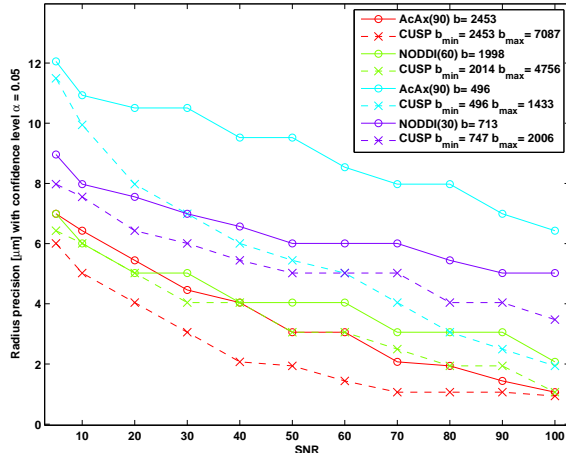
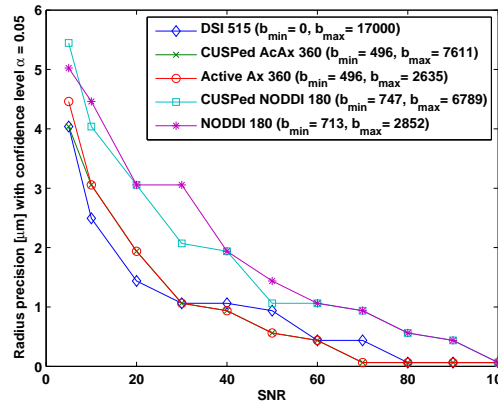
(A) 10 out of the 54 available 90-direction HARDI shells ($N_{rep} = 50$).(B) HARDI vs CUSP shells ($N_{rep} = 75$).(C) Complete traditional acquisition protocols ($N_{rep} = 75$).

FIGURE H.4: **More acquisitions and more gradient intensities lead to better matching.** Radius precision with confidence level $\alpha = 0.05$ for (A) single HARDI shells, (B) HARDI shells and their CUSP projections, (C) five traditional acquisition protocols (the number in the legend indicates the number of acquisitions). The order of appearance in the legend is based on an SNR level of 20. Units of G are in mTm^{-1} , Δ and δ in ms and b in mm^{-2} . The apparent discontinuities in the graphs are due to the discrete sampling of radius values within the dictionary and the way probabilities are computed, based on an experimental set of $N_{rep} \times 180$ samples.

Bibliography

- [1] Maria Eugenia Caligiuri, Stefania Barone, Andrea Cherubini, Antonio Augimeri, Carmelina Chiriaco, Maria Trotta, Alfredo Granata, Enrica Filippelli, Paolo Perrotta, Paola Valentino, et al. The relationship between regional microstructural abnormalities of the corpus callosum and physical and cognitive disability in relapsing–remitting multiple sclerosis. *NeuroImage: Clinical*, 7:28–33, 2015.
- [2] Benoît Macq (supply teacher : John Lee). Course notes GBIO2050 - Medical Imaging. Technical report, Université catholique de Louvain, 2015.
- [3] William S Price. *NMR studies of translational motion: principles and applications*. Cambridge University Press, 2009.
- [4] Santiago Aja-Fernández and Antonio Tristán-Vega. Influence of noise correlation in multiple-coil statistical models with sum of squares reconstruction. *Magnetic Resonance in Medicine*, 67(2):580–585, 2012.
- [5] Cheng Guan Koay, Evren Özarslan, and Peter J Basser. A signal transformational framework for breaking the noise floor and its applications in MRI. *Journal of Magnetic Resonance*, 197(2):108–119, 2009.
- [6] Erik G Larsson, Deniz Erdogmus, Rui Yan, Jose C Principe, and Jeffrey R Fitzsimmons. SNR-optimality of sum-of-squares reconstruction for phased-array magnetic resonance imaging. *Journal of Magnetic Resonance*, 163(1):121–123, 2003.
- [7] Denis S Grebenkov. Laplacian eigenfunctions in NMR. i. a numerical tool. *Concepts in Magnetic Resonance Part A*, 32(4):277–301, 2008.
- [8] Lawrence Evans. *Partial differential equations*. American Mathematical Society, 1998.
- [9] Maxime Taquet. *Multi-Fascicle Models of the Brain Microstructure for Population Studies: Acquisition, Estimation, Registration and Statistical Analysis*. PhD thesis, UCL, Louvain-la-Neuve, Belgium, 2013.

- [10] Peter J Basser, James Mattiello, and Denis LeBihan. MR diffusion tensor spectroscopy and imaging. *Biophysical journal*, 66(1):259, 1994.
- [11] Ben Jeurissen, Alexander Leemans, Jacques-Donald Tournier, Derek K Jones, and Jan Sijbers. Investigating the prevalence of complex fiber configurations in white matter tissue with diffusion magnetic resonance imaging. *Human brain mapping*, 34(11):2747–2766, 2013.
- [12] David S Tuch, Timothy G Reese, Mette R Wiegell, Nikos Makris, John W Belliveau, and Van J Wedeen. High angular resolution diffusion imaging reveals intravoxel white matter fiber heterogeneity. *Magnetic Resonance in Medicine*, 48(4):577–582, 2002.
- [13] Benoit Scherrer and Simon K Warfield. Parametric representation of multiple white matter fascicles from cube and sphere diffusion MRI. *PLoS one*, 7(11):e48232, 2012.
- [14] Benoit Scherrer, Armin Schwartzman, Maxime Taquet, Sanjay P Prabhu, Mustafa Sahin, Alireza Akhondi-Asl, and Simon K Warfield. Characterizing the distribution of anisotropic micro-structural environments with diffusion-weighted imaging (DIAMOND). In *Medical Image Computing and Computer-Assisted Intervention–MICCAI 2013*, pages 518–526. Springer, 2013.
- [15] A-S Lamantia and P Rakic. Cytological and quantitative characteristics of four cerebral commissures in the rhesus monkey. *Journal of Comparative Neurology*, 291(4):520–537, 1990.
- [16] Francisco Aboitiz, Arnold B Scheibel, and Eran Zaidel. Morphometry of the sylvian fissure and the corpus callosum, with emphasis on sex differences. *Brain*, 115(5):1521–1541, 1992.
- [17] Daniel C Alexander, Penny L Hubbard, Matt G Hall, Elizabeth A Moore, Maurice Ptito, Geoff JM Parker, and Tim B Dyrby. Orientationally invariant indices of axon diameter and density from diffusion MRI. *Neuroimage*, 52(4):1374–1389, 2010.
- [18] Hui Zhang, Torben Schneider, Claudia A Wheeler-Kingshott, and Daniel C Alexander. NODDI: practical in vivo neurite orientation dispersion and density imaging of the human brain. *Neuroimage*, 61(4):1000–1016, 2012.
- [19] Ofer Pasternak, Martha E Shenton, and Carl-Fredrik Westin. Estimation of extracellular volume from regularized multi-shell diffusion mri. In *Medical Image Computing and Computer-Assisted Intervention–MICCAI 2012*, pages 305–312. Springer, 2012.

- [20] R Mark Henkelman. Measurement of signal intensities in the presence of noise in MR images. *Medical physics*, 12(2):232–233, 1985.
- [21] Juwhan Liu and Jack L Koenig. An automatic phase correction method in nuclear magnetic resonance imaging. *Journal of Magnetic Resonance (1969)*, 86(3):593–604, 1990.
- [22] Denis S Grebenkov. NMR survey of reflected brownian motion. *Reviews of Modern Physics*, 79(3):1077, 2007.
- [23] Michal Aharon, Michael Elad, and Alfred Bruckstein. K-SVD: An algorithm for designing overcomplete dictionaries for sparse representation. *Signal Processing, IEEE Transactions on*, 54(11):4311–4322, 2006.
- [24] PA Cook, Y Bai, SKKS Nedjati-Gilani, KK Seunarine, MG Hall, GJ Parker, and DC Alexander. Camino: open-source diffusion-MRI reconstruction and processing. In *14th scientific meeting of the international society for magnetic resonance in medicine*, volume 2759, 2006.
- [25] Matt G Hall and Daniel C Alexander. Convergence and parameter choice for Monte-Carlo simulations of diffusion MRI. *Medical Imaging, IEEE Transactions on*, 28(9):1354–1364, 2009.
- [26] Eleftheria Panagiotaki, Torben Schneider, Bernard Siow, Matt G Hall, Mark F Lythgoe, and Daniel C Alexander. Compartment models of the diffusion mr signal in brain white matter: a taxonomy and comparison. *Neuroimage*, 59(3):2241–2254, 2012.
- [27] Van J Wedeen, Patric Hagmann, Wen-Yih Isaac Tseng, Timothy G Reese, and Robert M Weisskoff. Mapping complex tissue architecture with diffusion spectrum magnetic resonance imaging. *Magnetic Resonance in Medicine*, 54(6):1377–1386, 2005.
- [28] Els Fieremans, Dmitry S Novikov, Jens H Jensen, and Joseph A Helpert. Monte carlo study of a two-compartment exchange model of diffusion. *NMR in Biomedicine*, 23(7):711–724, 2010.
- [29] Denis S Grebenkov. A fast random walk algorithm for computing the pulsed-gradient spin-echo signal in multiscale porous media. *Journal of Magnetic Resonance*, 208(2):243–255, 2011.
- [30] Eleftheria Panagiotaki, Matt G Hall, Hui Zhang, Bernard Siow, Mark F Lythgoe, and Daniel C Alexander. High-fidelity meshes from tissue samples for diffusion mri

- simulations. In *Medical Image Computing and Computer-Assisted Intervention—MICCAI 2010*, pages 404–411. Springer, 2010.
- [31] Nadya Pyatigorskaya, Denis Bihan, Olivier Reynaud, and Luisa Ciobanu. Relationship between the diffusion time and the diffusion MRI signal observed at 17.2 tesla in the healthy rat brain cortex. *Magnetic Resonance in Medicine*, 72(2):492–500, 2014.
- [32] Daniel C Alexander. A general framework for experiment design in diffusion MRI and its application in measuring direct tissue-microstructure features. *Magnetic Resonance in Medicine*, 60(2):439–448, 2008.
- [33] Y Assaf, RZ Freidlin, and PJ Basser. The measurement of the axon diameter distribution in white matter using diffusion mr methods. In *Proc. ISMRM*, page 842, 2005.
- [34] C Meca, S Chabert, and D Le Bihan. Diffusion MRI at large b values: what’s the limit. In *Proceedings of the 12th Annual Meeting of ISMRM, Kyoto, Japan*, page 1196, 2004.
- [35] Alessandro Daducci, Erick J Canales-Rodríguez, Hui Zhang, Tim B Dyrby, Daniel C Alexander, and Jean-Philippe Thiran. Accelerated microstructure imaging via convex optimization (AMICO) from diffusion mri data. *NeuroImage*, 105:32–44, 2015.
- [36] Yaniv Assaf, Tamar Blumenfeld-Katzir, Yossi Yovel, and Peter J Basser. Axciliber: a method for measuring axon diameter distribution from diffusion MRI. *Magnetic Resonance in Medicine*, 59(6):1347–1354, 2008.
- [37] Yaniv Assaf, Raisa Z Freidlin, Gustavo K Rohde, and Peter J Basser. New modeling and experimental framework to characterize hindered and restricted water diffusion in brain white matter. *Magnetic Resonance in Medicine*, 52(5):965–978, 2004.
- [38] WA Edelstein, Paul A Bottomley, and Leah M Pfeifer. A signal-to-noise calibration procedure for NMR imaging systems. *Medical Physics*, 11(2):180–185, 1984.
- [39] Lin-Ching Chang, Gustavo K Rohde, and Carlo Pierpaoli. An automatic method for estimating noise-induced signal variance in magnitude-reconstructed magnetic resonance images. In *Medical Imaging*, pages 1136–1142. International Society for Optics and Photonics, 2005.
- [40] Jan Sijbers, Dirk Poot, Arnold J den Dekker, and Wouter Pintjens. Automatic estimation of the noise variance from the histogram of a magnetic resonance image. *Physics in medicine and biology*, 52(5):1335, 2007.

- [41] Cheng Guan Koay, Evren Özarslan, and Carlo Pierpaoli. Probabilistic identification and estimation of noise (PIESNO): a self-consistent approach and its applications in MRI. *Journal of Magnetic Resonance*, 199(1):94–103, 2009.
- [42] Jürgen Jost. *Partial Differential Equations*, volume 214 of *Graduate Texts in Mathematics*. Springer-Verlag, 2002.
- [43] Paul T Callaghan. *Principles of nuclear magnetic resonance microscopy*, volume 3. Clarendon Press Oxford, 1991.
- [44] Yu-Chien Wu, Aaron S Field, and Andrew L Alexander. Computation of diffusion function measures in-space using magnetic resonance hybrid diffusion imaging. *Medical Imaging, IEEE Transactions on*, 27(6):858–865, 2008.
- [45] MD Hurlimann, KG Helmer, TM Deswiet, and PN Sen. Spin echoes in a constant gradient and in the presence of simple restriction. *Journal of Magnetic Resonance, Series A*, 113(2):260–264, 1995.
- [46] Haim Brezis. *Functional analysis, Sobolev spaces and partial differential equations*. Springer Science & Business Media, 2010.
- [47] Chris A Clark and Denis Le Bihan. Water diffusion compartmentation and anisotropy at high b values in the human brain. *Magnetic Resonance in Medicine*, 44(6):852–859, 2000.